
# Semiconducting Nanocrystals: Synthesis, Colloidal Stability, and Charge Carrier Dynamics

**Dissertation**

Zur Erlangung des Grades

“Doktor der Naturwissenschaften” (Dr. rer. nat.)

im Promotionsfach Chemie

am Fachbereich Chemie, Pharmazie und Geowissenschaften

der Johannes Gutenberg Universität in Mainz

**Shuai Chen**

Geboren in Henan province, China

Mainz, 2023

Dekan: Prof. Dr.

1. Berichterstatter: Prof. Dr. Mischa Bonn

2. Berichterstatter: Prof. Dr. Carsten Sönnichsen

Tag der mündlichen Prüfung: 06/2023

Die vorliegende Arbeit wurde in der Zeit von 01/2019 bis 06/2023 im Max-Planck-Institut für Polymerforschung in Mainz unter der Betreuung von Dr. Hai Wang, Dr. Andreas Riedinger und Prof. Dr. Mischa Bonn durchgeführt.

## Declaration

I hereby declare that I wrote the dissertation submitted without any unauthorized external assistance and used only sources acknowledged in the work. All textual passages which are appropriated verbatim or paraphrased from published and unpublished texts as well as all information obtained from oral sources are duly indicated and listed in accordance with bibliographical rules. In carrying out this research, I complied with the rules of standard scientific practice as formulated in the statutes of Johannes Gutenberg-University Mainz to insure standard scientific practice.

Shuai Chen

# Table of Contents

## Abstract

Colloidal nanocrystals (NCs) with controllable morphologies and sizes are at the core of nanomaterials research. Among different NCs (zero-dimensional quantum dots, one-dimensional nanorods, etc.), two-dimensional cadmium selenide (CdSe) nanoplatelets (NPLs) with lateral extension of over 100 $nm^2$ and atomically precise thickness are one of the most promising semiconductors for optoelectronic applications. However, several issues remain for implementing CdSe NPLs for applications, including: (1) containing toxic and heavy elements, and (2) lacking a fundamental understanding of the colloidal stability and the process of charge carrier generation in solids. This thesis aims to synthesize environmentally friendly alternatives, such as indium phosphide (InP) NCs with varied shapes, and shed light on colloidal stability and charge carrier generation and dynamics using conventional CdSe NPLs as the model system.

The introductory **Chapter 1** briefly presents an overview of nanomaterials and nanotechnology, including quantum confinement in NCs, quantum dots, InP NCs, the synthesis status of CdSe NPLs, colloidal NCs stabilization in dispersion, photophysics of CdSe NPLs, ligand exchange method, and the thermal annealing method. In **Chapter 2**, we introduce terahertz (THz) spectroscopy basics, including the generation and detection mechanism, experimental setups, and the conductivity models for data analysis to infer charge transport properties in materials of interest. **Chapters 3-5** present the key results of this thesis. In **Chapter 3**, we synthesize InP NCs with different shapes and sizes by utilizing triphenyl phosphite as the phosphorus source. We show that InP NCs can be synthesized and formed from $In_2O_3$ NCs. Our findings open new synthetic possibilities by utilizing a cost-effective, non-pyrophoric, and non-toxic phosphorus precursor. In **Chapter 4**, we combine THz photoconductivity measurements with simulations to study the colloidal stability and aggregation process in CdSe NPL dispersion. We demonstrate that increasing the facet area of NPLs and the solvent length can reduce the critical concentration at which NPLs start aggregating. Our simulation attributes the effect to the solvation force-dominated colloidal stability for the NPL system; the solvation force is enhanced by increasing the NPL lateral area and the length of solvent molecules. In **Chapter 5**, we report that thermal annealing constitutes an effective strategy to control the optical absorption and electrical properties of CdSe NPLs by tuning the inter-NPL distance. We observe a direct correlation between the temperature-dependent ligand decomposition and the NPL-NPL distance shortening (by TEM). This leads to a strong red-shift in the absorption band edge (by UV-vis studies) and enhanced electrical transport

in NPL films. Our results illustrate a straightforward manner to control the interfacial electronic coupling strength for developing functional optoelectronics through thermal treatments.

## Zusammenfassung

Kolloidale Nanokristalle (NCs) mit kontrollierbarer Morphologie und Größe stehen im Mittelpunkt der Nanomaterialforschung. Unter den verschiedenen NCs (nulldimensionale Quantenpunkte, eindimensionale Nanostäbe usw.) gehören zweidimensionale Cadmiumselenid (CdSe)-Nanoplättchen (NPLs) mit einer lateralen Ausdehnung von über 100 $nm^2$ und einer atomar präzisen Dicke zu den vielversprechendsten Halbleitern für optoelektronische Anwendungen. Es bleiben jedoch noch einige Probleme bei der Implementierung von CdSe-NPLs für Anwendungen bestehen, darunter: (1) der Gehalt an toxischen und schweren Elementen,(2) das Fehlen eines grundlegenden Verständnisses der kolloidalen Stabilität und (3) des Prozesses der Ladungsträgererzeugung in Feststoffen. Ziel dieser Arbeit ist es, umweltfreundliche Alternativen wie Indiumphosphid (InP)-NCs mit unterschiedlichen Formen zu synthetisieren und Licht auf die kolloidale Stabilität und die Ladungsträgererzeugungsdynamik zu werfen, wobei herkömmliche CdSe-NPLs als Modellsystem dienen.

Das einleitende **Kapitel 1** bietet einen Überblick über verschiedene Nanomaterialien und Aspekte der Nanotechnologie, einschließlich des Effekts des Quanteneinschlusses (engl. quantum confinement) in NCs, der Betrachtung von Quantenpunkten, von InP-NCs, vom Synthesestatus von CdSe-NPLs, der kolloidale NC-Stabilisierung in Dispersionen, der Photophysik von CdSe-NPLs, von Methoden zum Austausch von Liganden und der thermischen Glühmethode. In **Kapitel 2** stellen wir die Grundlagen der THz-Spektroskopie vor, einschließlich des Erzeugungs- und Detektionsmechanismus, der Versuchsaufbauten und der Leitfähigkeitsmodelle für die Datenanalyse, um Ladungstransporteffekte in interessierenden Materialien abzuleiten. In den **Kapiteln 3-5** werden die wichtigsten Ergebnisse dieser Arbeit vorgestellt. In **Kapitel 3** synthetisieren wir InP-NCs mit unterschiedlichen Formen und Größen unter Verwendung von Triphenylphosphit als Phosphorquelle. Wir zeigen, dass InP-NCs aus $In_2O_3$-NCs synthetisiert und gebildet werden können. Unsere Erkenntnisse eröffnen neue Synthesemöglichkeiten durch die Verwendung eines kostengünstigen, nicht pyrophoren und ungiftigen Phosphorvorläufers. In **Kapitel 4** kombinieren wir THz-Photoleitfähigkeitsmessungen und Simulationen, um die kolloidale Stabilität und den Aggregationsprozess in CdSe-NPL-Dispersionen zu untersuchen. Wir zeigen, dass sowohl eine Vergrößerung der Facettenfläche von NPLs, als auch längere Lösungsmittelalkane die kritische Konzentration verringert, bei der NPLs zu aggregieren beginnen. Unsere Simulationen führen den Effekt auf die durch im Lösungsmittel auftretenden Kräfte (engl.

solvation forces) dominierte kolloidale Stabilität für das NPL-System zurück; Die im Lösungsmittel auftretenden Kräfte verstärken sich bei einer Vergrößerung der interagierenden NPL-Facetenflächen, sowie bei einer Verlängerung der Lösungsmittelmoleküle. In **Kapitel 5** berichten wir, dass thermisches Tempern eine wirksame Strategie zur Steuerung der optischen Absorption und der elektrischen Eigenschaften von CdSe-NPLs durch Abstimmung des Abstands zwischen den NPLs darstellt. Wir beobachten eine direkte Korrelation zwischen der temperaturabhängigen Ligandenzersetzung und der NPL-NPL-Abstandsverkürzung (durch TEM). Dies führt zu einer starken Rotverschiebung der Absorptionsbandkante (durch UV-Vis-Studien) und einem verstärkten elektrischen Transport in NPL-Filmen. Unsere Ergebnisse veranschaulichen eine einfache Möglichkeit, die Stärke der elektronischen Grenzflächenkopplung für die Entwicklung funktioneller Optoelektronik durch thermische Behandlungen zu steuern.

# Chapter 1: Introduction

## 1.1 A brief overview of nanomaterials and nanotechnology

Nanomaterials generally refer to materials with sizes ranging from 1 to 100 nm in at least one of the size dimensions. Metal nanoparticles (NPs) are arguably the earliest studied classes of nanomaterial systems. In 1850, Faraday observed that nanogold sol presents distinct optical phenomena in which the color of the gel changes with the gold size, which transmuted the "Alchemy of gold" into fascinating scientific research.[1] One hundred years later, Feynman proposed the concept of nanotechnology in his famous lecture "There's Plenty of Room at the Bottom: An Invitation to Enter a New Field of Physics" at the annual American Physical Society meeting in 1959. From then on, controlling matter at the nanoscale is the comprehensive dream of the nanotechnology field.

Nanomaterials may exhibit novel physical, chemical, mechanical, and optical properties,[2] which are fundamentally important for both scientific research and applications. For instance, along with the size reduction, the much enhanced surface-area-to-volume ratio (in comparison to their bulk counterparts) substantially increases the chemical reactivity of the materials, relevant for many chemical and electrochemical processes (e.g., catalysis). Furthermore, quantum confinement is expected to substantially modulate the electronic and optical properties of nanomaterials when their size is below the so-called Bohr radius (see more detailed discussions in **1.2.1**). Due to quantum confinement, nanomaterials have molecule-like discrete electronic states that exhibit size-dependent optical and electronic properties. In addition to the quantum confinement, the accompanied "dielectric confinement" can essentially reduce the charge screening between photogenerated electrons and holes, resulting in the formation of bounded electron-hole pairs (or so-called excitons).[3] The strong exciton effect of nanomaterials may dominate the electronic and optical properties, even at room temperature.

Quantum dots are nanomaterials with diameters in the range of 2-10 nm. It's one of the central topics in nanochemistry and nanomaterial science. In the 1980s, Ekimov, Efros[4], and Brus[5] put forward the concept of quantum confinement, which presented the start of the semiconductor QDs field. Peng et al. made a significant step forward by achieving the shape control synthesis of semiconductor CdSe QDs in 2000.[6] Since then, QDs have started to rapidly develop for biomedical

imaging, lasing, lighting displays, photonic quantum technology, and solar cell.[7,8,9] However, many QDs contain toxic elements (cadmium or lead). Thus, the development of nontoxic QDs composed of inexpensive and earth-abundant elements would greatly facilitate the development and commercialization of QD applications. In addition, the dimension and shape of nanomaterials directly impact their physical properties. Two-dimensional semiconductor nanoplatelets (NPLs), e.g., CdSe NPLs[10] are one of the most fascinating newly-developed colloidal nanomaterials, which has attracted much research attention. The fascinating optical gain effect for laser applications has been reported to originate from the biexciton states in NPLs.[11] Understanding the charge carrier dynamics (e.g. generation of free carriers and exciton complex in the ultrafast, picosecond (ps) time scale) is therefore important.

After several decades of meticulous research and intensive development, nanomaterials have emerged as highly practical and technologically significant foundational components for a wide range of applications. The community is developing rigorous methodologies to control the size, shape, and surface structure of a large number of functional materials. These synthetic developments are aimed at a deep understanding of fundamental electronic, magnetic, and other processes in nanomaterials.

This thesis dealt with two subjects: (1) developing indium phosphide (InP) NPs as one of the promising nontoxic nanomaterials for optoelectronics, and (2) understanding the physiochemical (e.g., colloidal stability) and photophysical (e.g., free carrier generation) of two-dimensional CdSe NPLs. Prior to presenting the scientific findings, Chapter 1 provides a thorough review of pertinent literature, encompassing topics such as synthesis methodologies and colloidal stability of NCs. Furthermore, Chapter 2 offers an overview of the experimental instruments employed throughout the thesis.

## 1.2 Semiconductor nanocrystals

### 1.2.1 Quantum confinement in nanocrystals

When the dimension of semiconductor materials shrink down to a sufficiently small size, confinement of the electronic wave function can result in new physical properties that drastically differ from the bulk. In bulk semiconductors, electrons are filled up to the top of the valence band with no occupation for the bottom of the conduction band. The energy difference between the

conduction band minimum and the valence band maximum defines a bandgap energy $E_g$ for a semiconductor. Photoexcitation of semiconductors promotes electrons across the bandgap from the valence to the conduction band and leaves one "hole" in the valence band. Photogenerated electrons and holes are subjected to Coulomb interactions. When the electron-hole interaction energy, e.g. the energy for ionizing electrons far away from the hole (so that they do not interact anymore) is much larger than thermal excitation ($k_BT$), electrons and holes are bound to form "excitons". When excitons are formed (e.g. at cryogenic temperatures), the electron can be seen orbiting around the hole charge. The physical separation between the electron and the hole defines the so-called Bohr radius (e.g. CdSe ~ 4 nm, InAs ~ 29 nm).[12] With decreasing the material size, the energy levels of the conduction band and valence band change from continuous distribution to discrete distribution (Figure 1-1). As the size reaches the nanoscale, where the nanocrystal is made up of only a smaller number of atoms or molecules, the number of overlapping orbitals or energy levels decreases. This will increase the energy gap between the conduction band and the valence band. This explains the higher energy gap in NP than that in the corresponding bulk material.

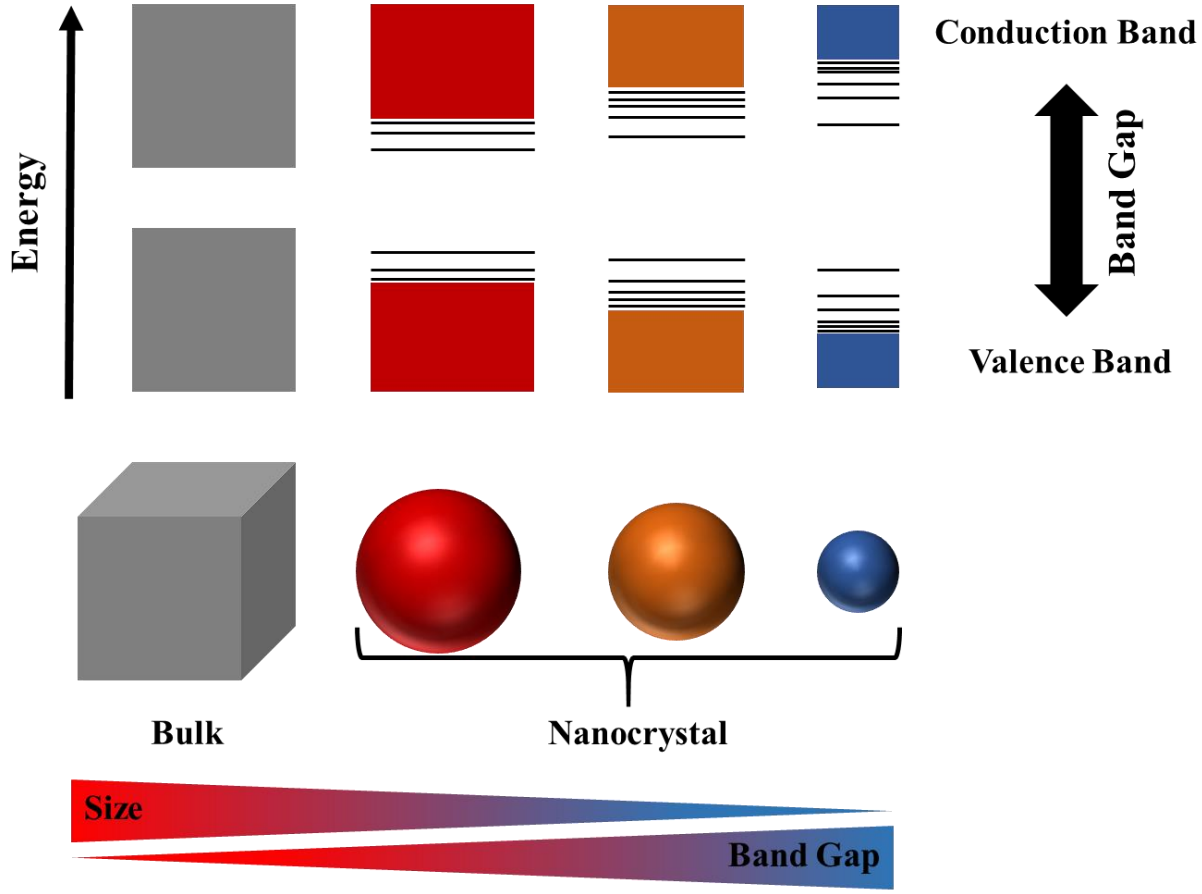

**Figure 1-1**. Electronic states of bulk and quantum materials.

### 1.2.2 Quantum dots

QDs are important low-dimensional semiconductor materials that experience strong spatial quantum confinement due to their small size, which is no larger than twice the Bohr radius. This quantum confinement makes QDs uniquely capable of potentially color-pure fluorescence (if no defects) that can be precisely controlled by the size and crystalline structures. QDs are sometimes called "artificial atoms" because of the discrete electronic energy levels, which are analogous to isolated atoms in a manner. This confinement effect can be readily understood by the famous "particle in a box" model.[12]

QDs are typically spherical or quasi-spherical, with sizes ranging from 2 to 20 nm. The most common QDs are composed of IV, II-VI, IV-VI, and III-V elements. Specific examples include silicon (Si) QDs,[13] germanium (Ge) QDs,[14] cadmium sulfide (CdS) QDs,[15] cadmium selenide (CdSe) QDs,[16] cadmium telluride (CdTe) QDs,[17] zinc selenide (ZnSe) QDs,[18] lead sulfide (PbS) QDs,[19] lead selenide (PbSe) QDs,[20] indium phosphide (InP) QDs,[21] and indium arsenide (InAs) QDs.[22] Importantly, a wide array of research areas including biomedical imaging, lasing, lighting displays, and photonic quantum technology rely on the optimized fluorescent QDs. Figure 1-2 depicts the reported emission ranges for several kinds of QDs.

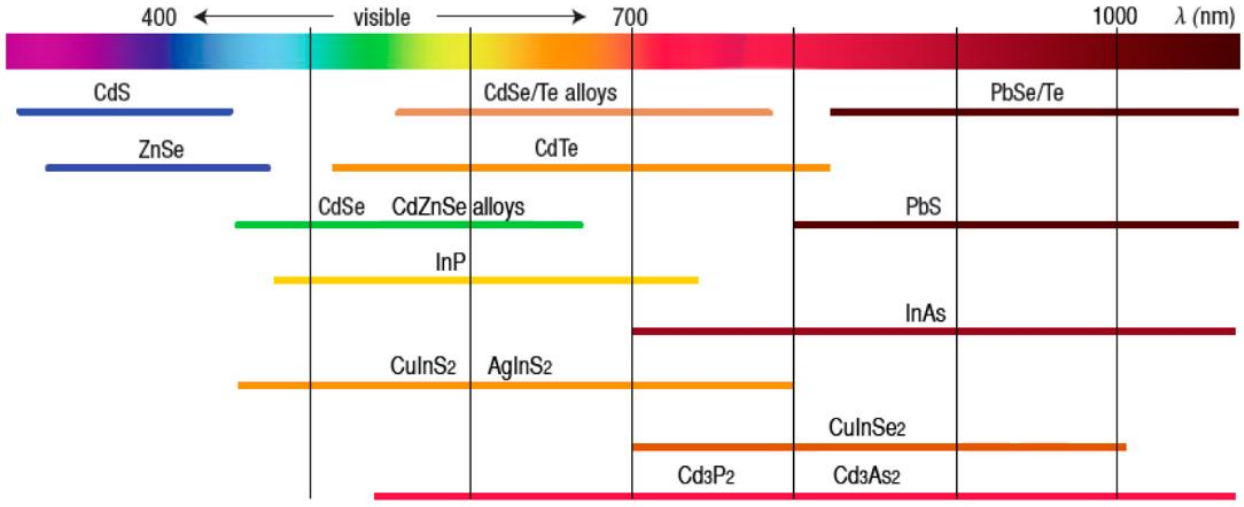


**Figure 1-2.** The spectral range of emission for the most widely studied semiconductor NCs.[23] (Reprinted with permission from ref. 23, Copyright 2016, American Chemical Society.)

### 1.2.3 InP nanocrystals

Since their discovery 40 years ago, QDs have been used in both fundamental research and application development.[2] As depicted in Figure 1-3, QD applications are mostly based on exquisite optical properties including light-emitting diodes (LEDs), photovoltaics, photoconductors and photodetectors, biomedical and environmental applications, catalysis, and other applications.[24] However, a particular concern is that the best-performed NC system is CdSe-based. Inherent cadmium toxicity limits its implementation in biological and industrial applications.

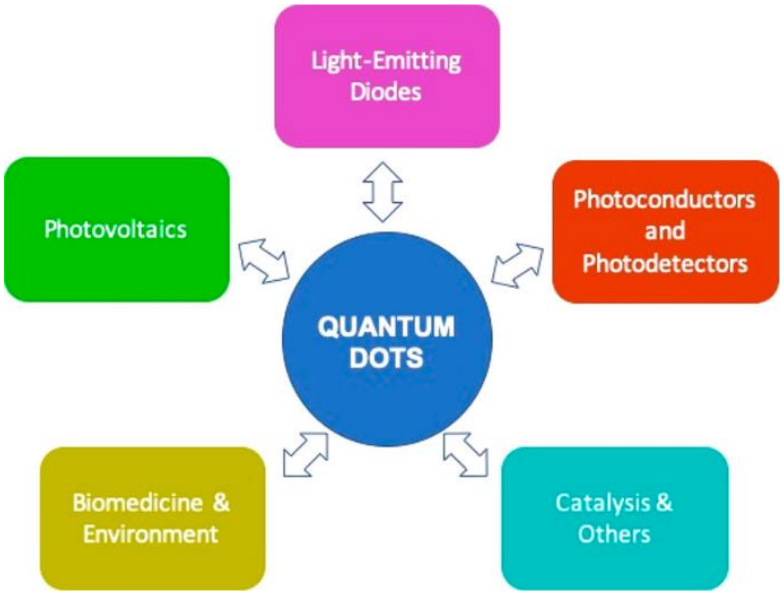


**Figure 1-3.** QD-based applications.[24] (Reprinted with permission from ref. 24, Copyright 2020, American Chemical Society.)

As a result, toxic-free and environmentally friendly alternative materials, including III-V QDs such as InP, have been developed and explored for optical and optoelectronic applications in recent years.[25,26,27] Besides being nontoxic, compared with the CdSe, the smaller bandgap (1.27 vs 1.74 eV for the bulk) allows the InP QDs emission to be tuned from the visible to the near-infrared (IR) region. Additionally, the bulk InP has higher carrier mobility (up to 4600 $cm^2$ $V^{-1}$ $s^{-1}$). Another significant feature is its larger Bohr exciton diameter bigger than CdSe (21.61 vs 6.04 nm), thus offering greater optical tunability than CdSe.[28]

So far, the primary research effort on InP nanocrystal materials has been devoted to synthesis (chemicals, synthetic techniques, and shape control), growth mechanisms (classical nucleation and

growth mechanisms, cluster formation, size-dependent growth rate), and surface chemistry (ligand, ligand exchange, surface oxidation).

**Synthesis.** In most synthetic routes, the solution-based InP nanocrystal synthesis involves the reaction of indium (long alkyl-chain carboxylates or halide) and phosphorus sources at high temperatures (>180 °C) in high-boiling point solvents (e.g., ODE). Normally, researchers have shown that indium carboxylate plays a critical role in tuning NCs size distribution and serves as a stabilizing ligand. Because of its strong reactivity, tris(trimethylsilyl)phosphine (TMSiP) is the most common phosphorus source.[28] Heat-up, microwave, and hot-injection methods were used to grow InP NCs with smaller diameters (< 3.5 nm). When aiming at synthesizing large crystals, only the continuous hot-injection method has been reported to produce large InP NCs up to 27 nm.[29] In 2016, Kim et al. produced tetrahedral and triangular prism InP QDs with 5-10 nm through the synergistic passivation of halide-amine in indium-rich (111) facets (Figure 1-4a).[30] In 2021, Jeong et al. isolated the metastable intermediates (tetrapod InP QDs) from the formation of tetrahedral InP QDs (Figure 1-4b).[31]

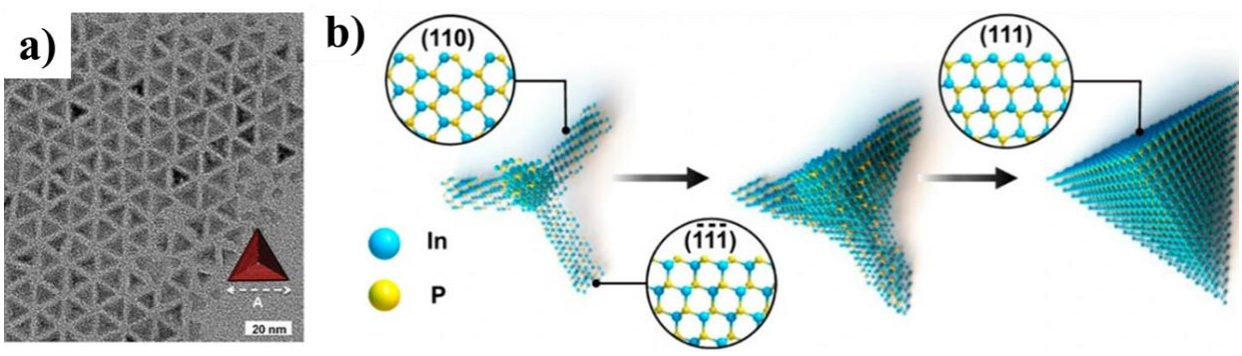


**Figure 1-4**. (a) TEM image of InP tetrahedral NCs.[30] (Reprinted with permission from ref. 30, Copyright 2016, John Wiley and Sons.) (b) Schematic illustrations of the crystalline structures from tetrapod to tetrahedron.[31] (Reprinted with permission from ref. 31, Copyright 2021, Springer Nature.)

**Growth mechanisms**. Understanding the growth mechanisms allows for optimizing the quality of InP QDs. For the classical nucleation theory (CNT), the seed crystals form monomeric precursors and further grow to QDs. Based on CNT, there exists a critical radius, above which the QD growth is thermodynamically favorable. On the contrary, the nucleus redissolves back into monomer species (Figure 1-5a). In 1950, the LaMer model was proposed to describe nanocrystal nucleation and growth. The LaMer model assumes that the rapidly increasing concentration of

monomers will induce a "burst" of nucleation (Figure 1-5b). However, the growth of InP QDs shows a significant deviation from classical nucleation theory. In 2009, Xie et al. studied InP cluster formation through the appearance of an absorbance feature at 386 nm. This nanoscale cluster, also termed as "magic-sized cluster" (MSC)[32], possesses a precise number of atoms and is reported to be thermodynamically stable. In 2016, matrix-assisted laser desorption ionization-time of flight mass spectrometry was used to analyze the MSC information. High-temperature ab initio molecular dynamics was used to discover the early-stage intermediate $In_4P$ MSC (Figure 1-5c). Furthermore, single-crystal X-ray diffraction (XRD) revealed that the InP MSC structure is $In_{37}P_{20}(O_2CR)_{51}$ with a pseudo tetrahedral arrangement at a 0.83 Å resolution. Hence, the formation of MSCs is an important intermediate process for the growth of InP QDs. Later, in the seedless continuous injection method, Achorn et al. found that new QDs continuously nucleated while the existing larger QDs' growth slowed significantly (Figure 1-5d).[29]

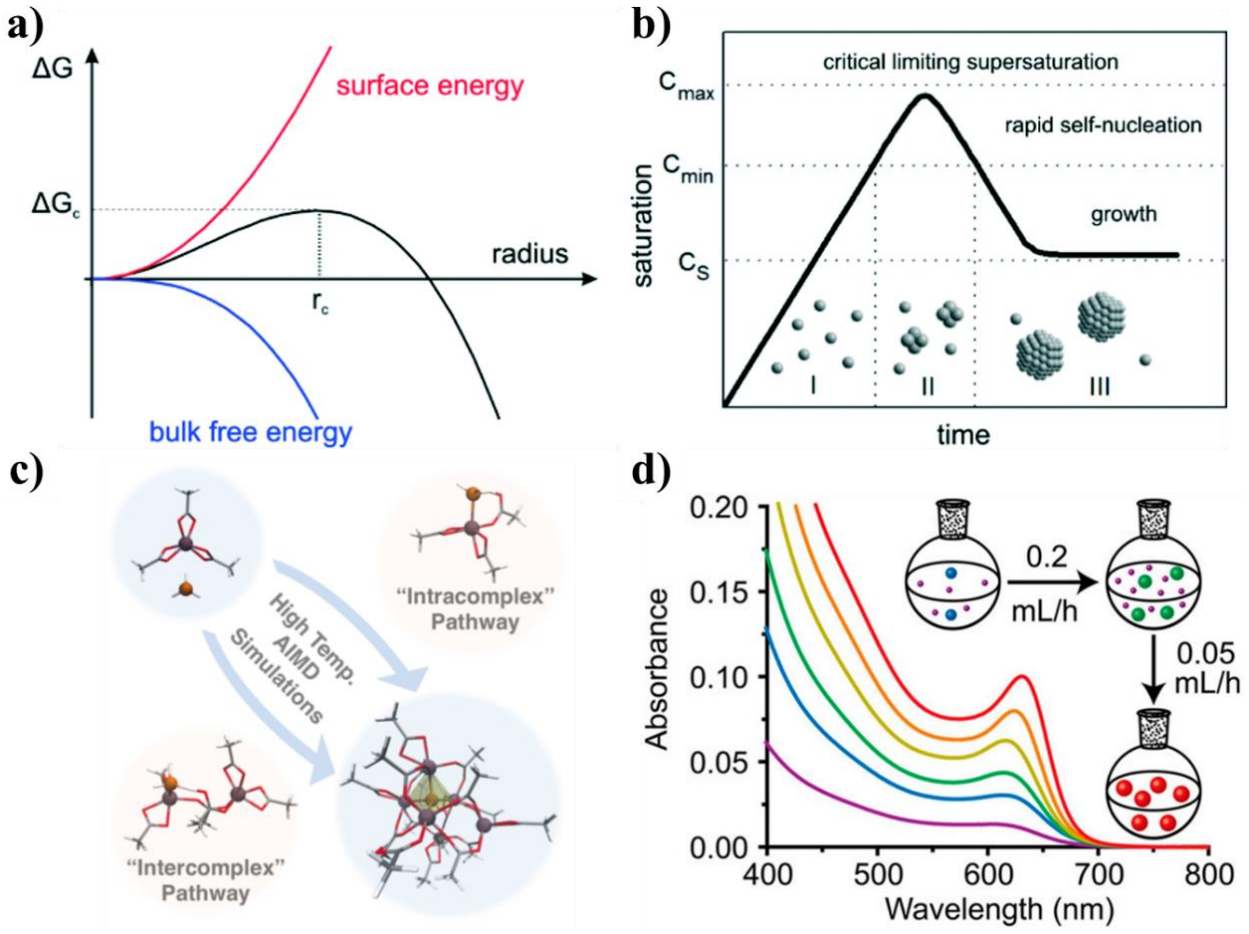


**Figure 1-5.** (a) Classical nucleation theory model. (b) LaMer model for nucleation vs growth of nanoparticles.[28] (Reprinted with permission from ref. 28, Copyright 2023, American Chemical

Society.) (c) The cluster formation in the early-stage InP QDs growth process.[34] (Reprinted with permission from ref. 34, Copyright 2016, American Chemical Society.) (d) Size-dependent growth detected by absorption spectra.[29] (Reprinted with permission from ref. 29, Copyright 2020, American Chemical Society.)

**Surface chemistry**. The ligands and bonding environment at the surface dominate the surface chemistry of InP QDs. For a variety of applications, we need to understand and control the ligand exchange dynamics, surface fluorination, and controllable interface shell (Figure 1-6).[35] In the ligand exchange process, carboxylate-capped InP QDs can be treated with other ligands (amines, palmitate, or inorganic ligand) to modify surface reactivity and quantum yield.[36,37,38] For surface fluorination, HF etching is a well-known tactic for increasing InP QD quantum yields.[39,40] To enhance the photoluminescence and chemical stability, the growth of interface shell around QDs to form so-called core-shell structures has been developed. For InP QDs, Zn- based shell growth (i.e., ZnSe and/or ZnS) has been developed as the predominant method.[41,42]

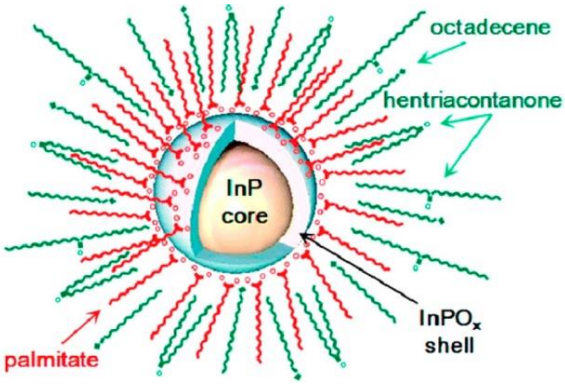


**Figure 1-6.** Schematic view of InP NCs surface.[35] (Reprinted with permission from ref. 35, Copyright 2016, American Chemical Society.)

## 1.3 CdSe nanoplatelets

### 1.3.1 Introduction of nanoplatelets

Quasi-two-dimensional (2D) semiconductor NPLs are atomically flat sheets whose thickness is much smaller than the Bohr radius. The 2D NPLs family includes cadmium chalcogenides, lead chalcogenides, indium selenide, and $CsPbX_3$ perovskites (Figure 1-7), etc.[43]

As an emerging class of photoactive materials, 2D semiconducting NPLs can be used in optoelectronic devices thanks to their large absorption coefficient, high carrier mobility, and

unique thickness-dependent optical transitions.[44] Due to their 2D nature, the charge carriers are strongly confined in the thickness and may be also weakly confined in the lateral dimensions (depending on the lateral sizes). Thus, the extension of lateral sizes has minor effects on the electronic structures in NPLs: i.e. their energy levels are independent of the lateral size. Charge carriers in 2D NPLs can move freely in the plane, which may lead to superior charge transport compared to QDs. Furthermore, because of the strong quantum confinement in 2D NPLs, the narrow photoluminescence (PL) emission can be tuned by precisely controlling their thickness at the nanoscale.

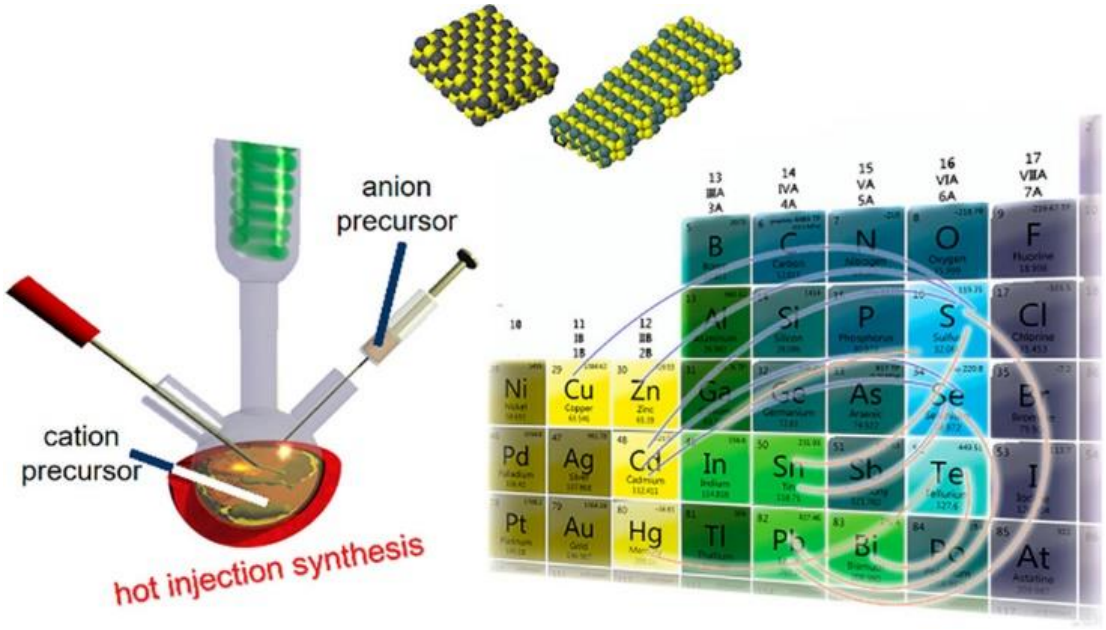


**Figure 1-7.** Two-dimensional colloidal semiconductor nanoplatelets: synthesis method and possible compositions.[45] (Reprinted with permission from ref. 45, Copyright 2021, American Chemical Society.)

### 1.3.2 Synthesis status of CdSe nanoplatelets

**Wurtzite CdSe nanoplatelets**. In 2006, the first colloidal CdSe NPLs (which by then were termed as "nanoribbons") were synthesized in the solvent phase by Hyeon et al.[46] This is also the first report on semiconductor CdSe NCs with one-dimensional confinement. These NPLs with wurtzite structures are synthesized at a low temperature (120 ℃), compared to molecular beam epitaxy or chemical vapor deposition at high temperature (500-700 ℃). From the TEM image, the width (10-20 nm) is beyond the quantum confinement. The uniform 1.4 nm thickness confirms its

2D characteristic. In 2009, Hyeon et al. used selenium and octanamine to obtain large-scale CdSe NPLs with 1.4 nm thickness (Figure 1-8a).[47] The long-chain amine not only reduces the effective contact between organic layers but also increases the steric hindrance, which weakens the interaction between nanosheets and makes it possible to monodispersed by simple ultrasonication (Figure 1-8b).

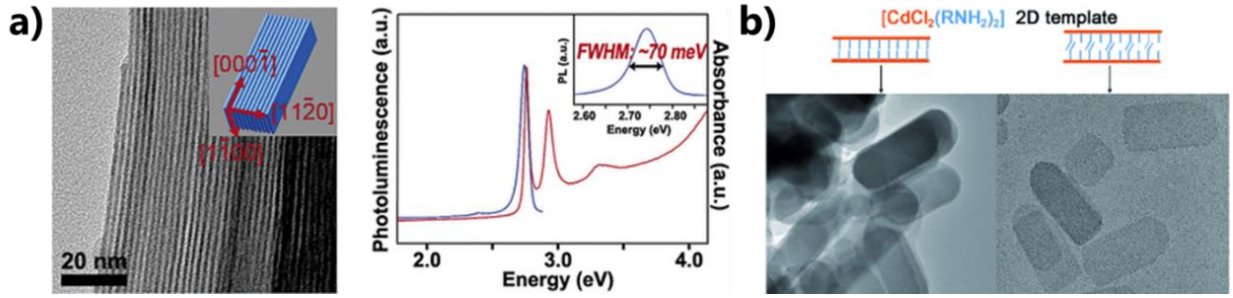


**Figure 1-8**. (a) TEM images and UV−vis absorption of wurtzite CdSe "nanoribbons".[46] (Reprinted with permission from ref. 46, Copyright 2006, American Chemical Society.) (b) Lamellar-structured CdSe NPLs.[47] (Reprinted with permission from ref. 47, Copyright 2009, John Wiley and Sons.)

**Zinc-blende CdSe nanoplatelets.** Compared with the hexagonal wurtzite structure, the zinc-blende structure has a more uniform distribution of size, shape, and more controllable thickness with better dispersion properties in solution.[48] The first synthesis of zinc-blende CdSe NPLs occurred in 2008 by Dubertret et al. (Figure 1-9).[48] The temperature was reported as the key to precisely controlling the thickness of the NPLs from 3 to 5 monolayers (ML). Moreover, the peak positions of the PL spectrum are located at 462 ± 2 nm, 512 ± 2nm, and 550 ± 2 nm. The FWHM is extremely narrow (~10 nm). The narrow peak indicates the uniform thickness of NPLs. Compared with the absorption spectrum, the stokes shift is extremely small (nearly zero).

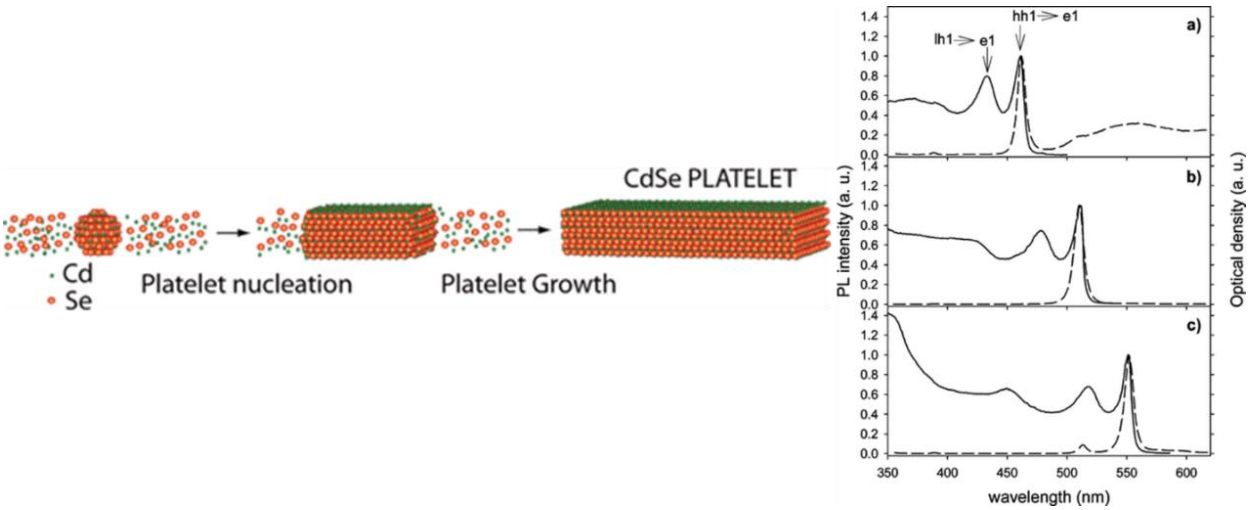


**Figure 1-9.** Room temperature UV-Vis (dash line) and PL (dash solid line) spectra of 3 ML, 4 ML, and 5 ML CdSe NPLs.[48] (Reprinted with permission from ref. 48, Copyright 2008, American Chemical Society.)

The NPL optical properties, such as the Auger recombination rate[49] and optical gain threshold[50] are strongly correlated to the CdSe NPLs thickness. The synthesis of thicker NPLs is difficult because the larger seeds easily create spherical QDs rather than 2D growth. Recently, thicker NPLs have been synthesized with different improved methods. Iwan et al. achieved a transversal growth of CdSe NPLs from 4 ML up to 8 ML (625 nm emission) by adding $CdCl_2$ in a two-step reaction at high temperature (Figure 1-10a);[51] Dmitri et al. introduced the chloride to change the nucleation barrier for island formation to grow 6 ML CdSe NPLs (Figure 1-10b);[52] Emmanuel et al. used the colloidal atomic layer deposition (c-ALD) method to obtain 11 ML CdSe NPLs (Figure 1-10c).[53]

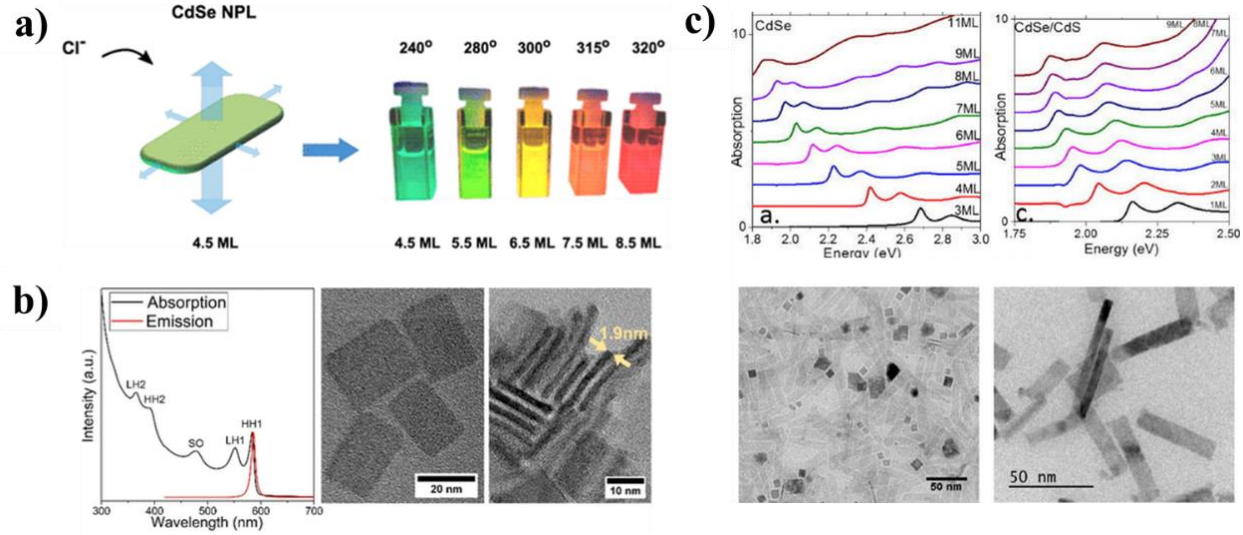

**Figure 1-10.** (a) Chloride-induced thickness control in CdSe NPLs.[51] (Reprinted with permission from ref. 51, Copyright 2018, American Chemical Society.) (b) Direct synthesis of 6 ML (1.9 nm) thick zinc-blende CdSe NPLs emitting at 585 nm.[52] (Reprinted with permission from ref. 52, Copyright 2018, American Chemical Society.) (c) Thickness-controlled CdSe and CdSe/CdS NPLs.[53] (Reprinted with permission from ref. 53, Copyright 2018, AIP Publishing.)

### 1.3.3 Colloidal nanoparticle stabilization in dispersion

Colloidal stability is one of the major aspects in dispersion chemistry, which is relevant for not only the processability of NCs for devices but also NCs' functionality in dispersion. Colloidal stability depends on the different forces that NPs experience, which include van der Waals (vdW) attractions, electrostatic interactions (in polar solvent), and solvation forces. Those interaction forces need to be balanced to get a stable dispersion. When aggregation appears, the surface of the whole system is reduced, which is unfavorable for applications including catalysis, which requires a large surface area for operation.

In the following, we review theories and relevant critical forces that have been identified for describing and governing colloidal stability (in particular for NPLS).

#### 1.3.3.1 DLVO theory

In 1941, Derjaguin and Landau introduced a theory to account for the stability of colloidal dispersions. In this theory, the vdW attractions are countered by the stabilizing influence of electrostatic repulsions.[95] Seven years later, Verwey and Overbeek reported the same result independently.[132] The part of interaction forces for stabilized NPs could be described by DLVO theory (named after Boris Derjaguin, Lev Landau, Evert Verwey, and Theodoor Overbeek), which combines vdW forces and electrostatic interaction to estimate the actual interaction between NPs.

**Van der Waals interaction**

In molecular physics, vdW is a distance-dependent interaction between atoms or molecules which is calculated by the contribution of all interacting atom pairs in NPs. By using the Derjaguin approximation,[139] the interaction energy $G_{vdW}$ between two NPs (spheres or plates) is as follows:

The interaction energy between two spheres:

$$G_{vdW} = -\frac{A}{6D}\frac{R_1 R_2}{R_1 + R_2} \quad (Equation\ 1.1)$$

The interaction energy between two plates:

$$G_{vdW} = -\frac{A}{12\pi D^2} \ (Equation\ 1.2)$$

Where D is the distance between NPs, R is the radius of NPs, and A is the Hamaker constant.

**Electrostatic interaction (Electrostatic double-layer forces)**

For electrostatic interaction, the double-layer forces are considered here. In NPs, the charged molecules form the first layer, and the equilibrium of charged counterions around the first layer forms the second layer. The electrostatic interaction (EI) between two NPs (spheres or plates) is as follows:

The interaction energy between two spheres:

$$G_{EI} = \frac{64k_BTR\rho_\infty\gamma^2}{\kappa^2}e^{-\kappa D}(Equation\ 1.3)$$

The interaction energy between two plates:

$$G_{EI} = \frac{64k_BT\rho_\infty\gamma^2}{\kappa}e^{-\kappa D}(Equation\ 1.4)$$

Where $k_B$ is the Boltzmann constant, $\rho_\infty$ is the number density of ions in bulk solution, and $\gamma$ is the reduced surface potential.

**Total interaction energy based on DLVO**

The DLVO force is the addition of the vdW force and electrostatic interaction, which is the total interaction energy between two NPs. Additionally, Born repulsion is the sum of Coulombic attraction potential and short-range repulsive potential. When the two NPs are closer enough (smaller than the radio of NPs), the Born repulsion needs to be included. The total energy is given by:[154]

The interaction energy between two spheres:

$$G_{total} = G_{vdW} + G_{EI} + G_{Born} = -\frac{A}{6D}\frac{R_1R_2}{R_1+R_2} + \frac{64k_BTR\rho_\infty\gamma^2}{\kappa^2}e^{-\kappa D} + \frac{1}{d^{12}} \ (Equation\ 1.5)$$

The interaction energy between two plates:

$$G_{total} = G_{vdW} + G_{EI} + G_{Born} = -\frac{A}{12\pi D^2} + \frac{64k_BT\rho_\infty\gamma^2}{\kappa}e^{-\kappa D} + \frac{1}{d^{12}} \ (Equation\ 1.6)$$

The interactions are summarized in the plot Figure 1-11.

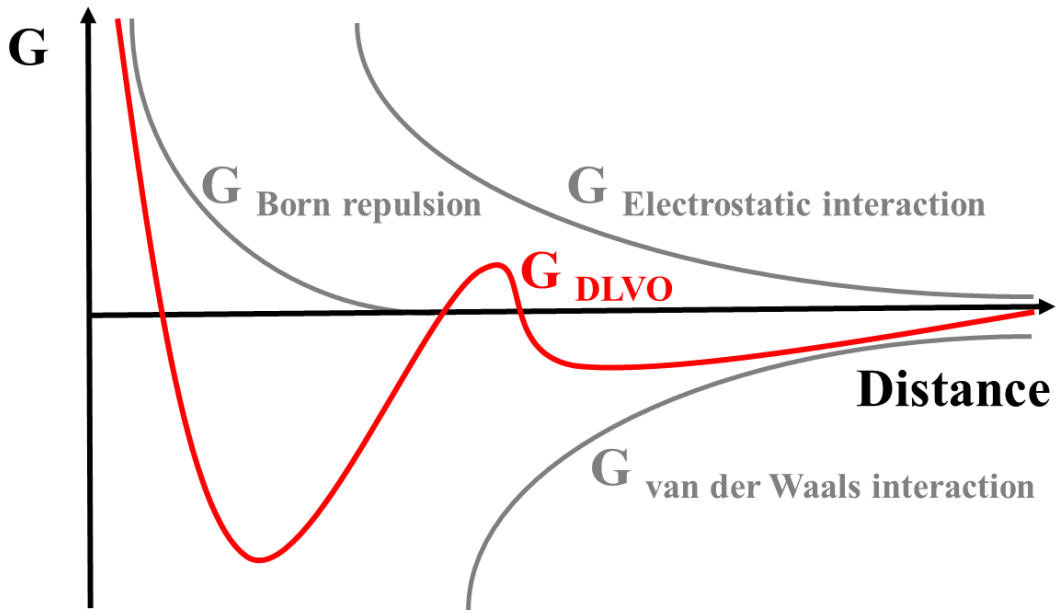


**Figure 1-11.** Total interaction of DLVO theory with distance (red curve).

### 1.3.3.2 Solvation forces

When the vdW interactions are weak between NPs, the simplified DLVO theory breaks down. The ligand and solvent molecules need to be considered. The as-prepared NPs are coated with ligands and dispersed in organic solvents. The organic solvent can cause fluids around ligand-capped NCs. When two NPs approach each other, the organic solvent forms layers. Due to the layering and changed entropy of the solvent, the solvation forces can emerge and can't be ignored. More importantly, the solvation forces are critically dependent on the ligand length, ligand grafting density, and facet area (Figure 1-12).[54] We will investigate the criticality of solvent force in dictating the NPL dispersion stability in chapter 4.

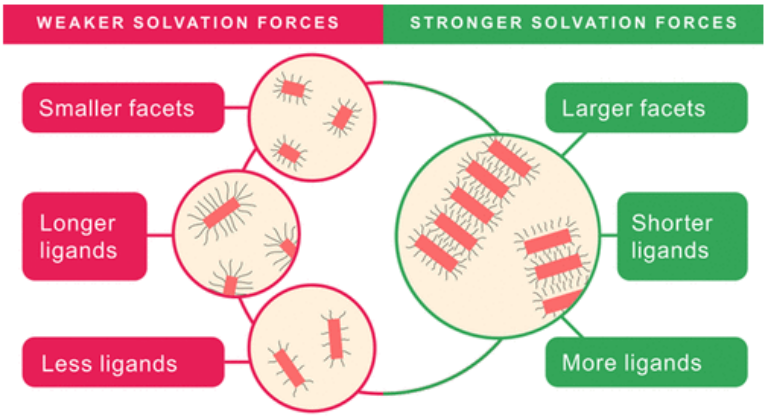

**Figure 1-12.** The crucial role of solvation forces in the steric stabilization of NPLs.[54] (Reprinted with permission from ref. 54, Copyright 2022, American Chemical Society.)

### 1.3.4 Photophysical of CdSe nanoplatelets

For many potential applications in the fabrication of optoelectronic and electronic devices, deposition of NC thin films from the dispersion is mandatory. Understanding how the charge carrier dynamics evolve from the solution phase to solid-state assembly is necessary to improve the device's performance.

The CdSe NPLs are two-dimensional NPs whose thickness is controlled at the atomic level. The ordered assembly of NPLs into superlattices will lead to new features such as the polarization of light, the appearance of phonon lines at low temperatures, or efficient energy transfer.[55,56,57,58] Furthermore, when the NPLs are assembled to stack, the exciton transfer between NPLs happens through resonant non-radiative energy transfer processes which are called homo-Förster resonance energy transfer (FRET).[59] Moreover, Nadja et al. manufactured the polymer-encapsulated NPLs stacks and reduced the inter-NPL distance, as predicted, enhancing the photocurrent in devices.[60] Recently, by enhancing the coupling strength between the NPLs, our group employing THz spectroscopy, observed a transition from the excitonic response in dispersed NPLs to quasi-free carriers in the edge-up assembly NPLs.[58] However, the as-synthesized NPLs are capped with long carbonic ligands, which leads to long NPL distances and prohibits efficient charge transport between NPLs. Therefore, surface ligand modification is an effective way to decrease NPL distance and improve charge transport efficiency.

There are two main ways to modify surface ligands: ligand exchange and thermal annealing.

#### 1.3.4.1 Ligand exchange method

The exposed Cd-terminated surfaces of zinc-blende CdSe NPLs are stabilized by various types of ligands. Ligands are an essential part of the NPL-ligand complex, which can play an important role in tuning the optical features, inter-NPs distance, as well as charge transport properties of NPLs.

**Tuning the optical features.** Normally, the NPLs are stabilized in organic solvents (e.g., hexane) through long steric ligands (e.g., myristic acid or oleic acid). For optical spectral tunability, redshifts with varied magnitudes are usually observed after the exchange with various longer

functionalized molecules (the length is similar to myristic acid), including hexadecyl-phosphonates (HDPA) (Figure 1-13a, b)[61,62] and Br/oleylamine (Figure 1-13c).[63] The excitonic transition energies redshift up to 240 meV. These substantial bathochromic shifts or reductions of bandgap energy were originally from strain-induced lattice distortion.[62] The lattice distortions may be attributed to multiple factors such as strain induced by the van der Waals attraction, surface reconstruction caused by ligand head groups, or different ligand packing densities.[62] Briefly speaking, the ligand exchange could reduce the confinement effects by extension in the vertical dimension. Apart from optical spectral tunability, other new features will appear. For example, HDPA could control the NPLs stack length by varying its concentration and reaction time.[61] Hydrogen bonding between halides and amines provides highly stable colloidal in nonpolar solvents, passivates the traps, and increases the fluorescence QY (up to 70 %).[63]

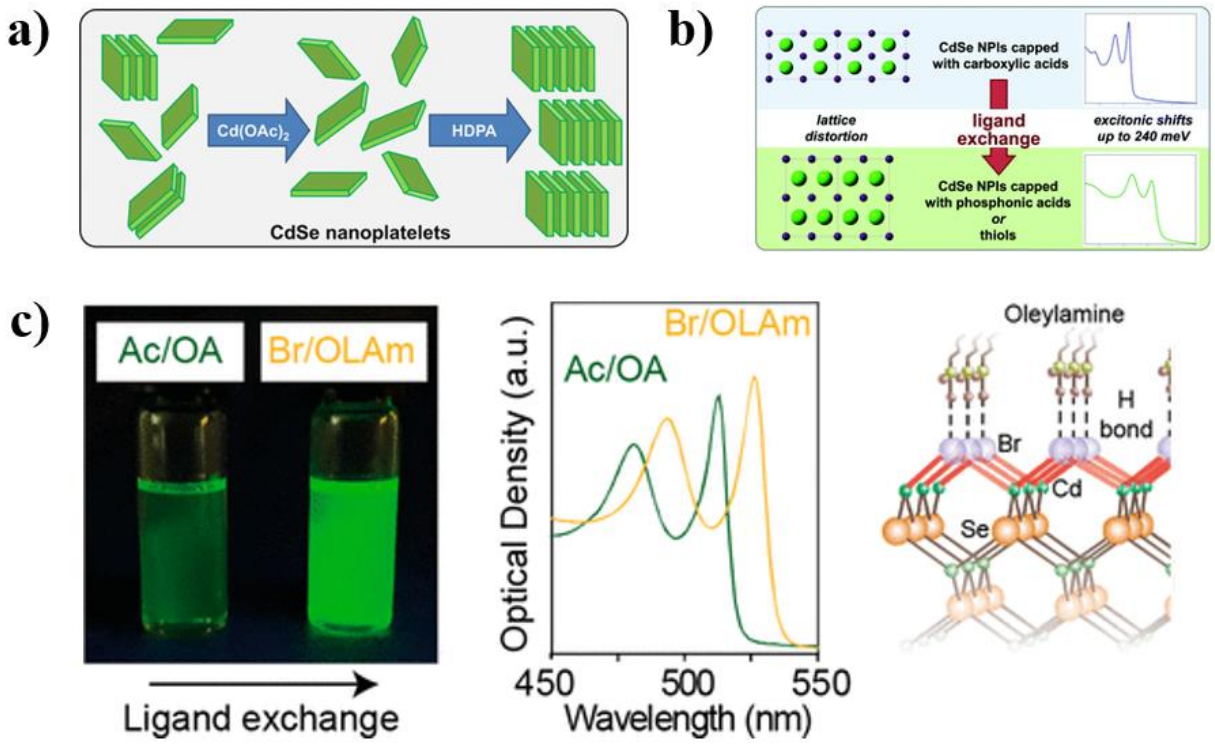


**Figure 1-13.** (a) Self-assembly of CdSe NPLs into stacks of controlled size induced by ligand exchange.[61] (Reprinted with permission from ref. 61, Copyright 2016, American Chemical Society.) (b) The impact of organic ligand shell on the exciton transition energy shift in CdSe NPLs.[62] (Reprinted with permission from ref. 62, Copyright 2017, Royal Society of Chemistry.) (c) Halide ligands to release strain in CdSe NPLs and achieve high brightness.[63] (Reprinted with permission from ref. 63, Copyright 2019, American Chemical Society.)

**Tuning inter-NPLs coupling for charge transport.** To modify the inter-NPL distances, one of the most straightforward methods lies in ligand exchange. The native long-chain carboxylic acid could be replaced by halide and short amine/phosphonate/thiolate (Figure 1-14).[64,65,66,67] Treatment of CdSe NPLs with inorganic halide ions resulted in large bathochromic shifts of excitonic absorption and a short distance between NPLs. (Figure 1-14a). The halide-capped NPLs can decrease the inter-NPLs distance by using two-phase ligand exchange and exhibit a reversible process (Figure 1-14b). The ligand exchange in zinc-blende CdSe NPLs can achieve – ethylenediamine-terminated to decrease the inter-NPLs distance. (Figure 1-14c).

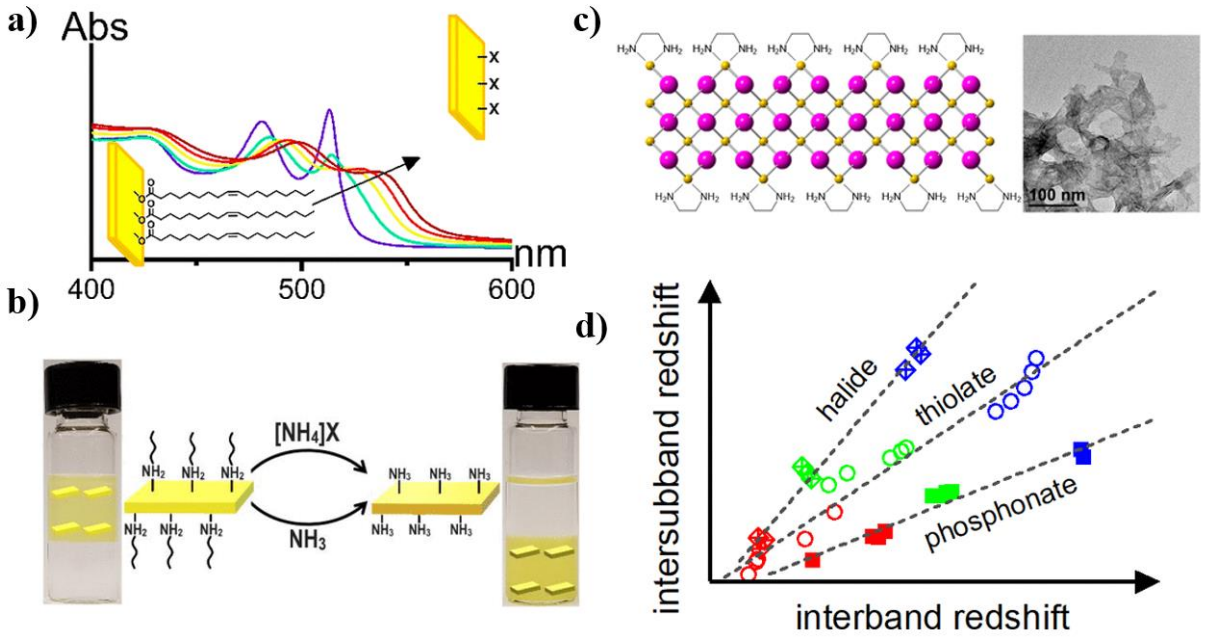


**Figure 1-14**. (a) Shape-selective optical transformations of CdSe NPLs driven by halide ion ligand exchange.[64] (Reprinted with permission from ref. 64, Copyright 2019, American Chemical Society.) (b) Two-phase ligand exchanges on CdSe NPLs with a reversible process.[65] (Reprinted with permission from ref. 65, Copyright 2020, American Chemical Society.) (c) The ethylenediamine-terminated NPLs.[66] (Reprinted with permission from ref. 66, Copyright 2020, American Chemical Society.) (d) Ligand-dependent tuning of inter-band and inter-subband transitions of CdSe NPLs.[67] (Reprinted with permission from ref. 67, Copyright 2020, American Chemical Society.)

The as-prepared NPLs could be encapsulated into a polymer shell to form larger units (Figure 1-15a). The NPL larger unit stacks show applications like photo-electrochemical sensing, such as exciton transport in the stack direction.[68] However, the longer NPL-NPL distance within the stacks

influences the photo-electrochemical properties. Considering that smaller distances should greatly enhance charge carrier transport due to larger electronic wave function overlap of neighboring NPLs, a decrease of the NPL-NPL distance might pave the way toward future applications of NPL assemblies such as (photo)transistors, photoconductors, sensors for photodetection in solar cells, or as light-emitting diodes. The exchange is assisted by the addition of different amounts of $CdBr_2$. Afterward, the ligand-exchanged NPLs are employed in the assembly of NPL stacks with ultra-small NPL–NPL distances.

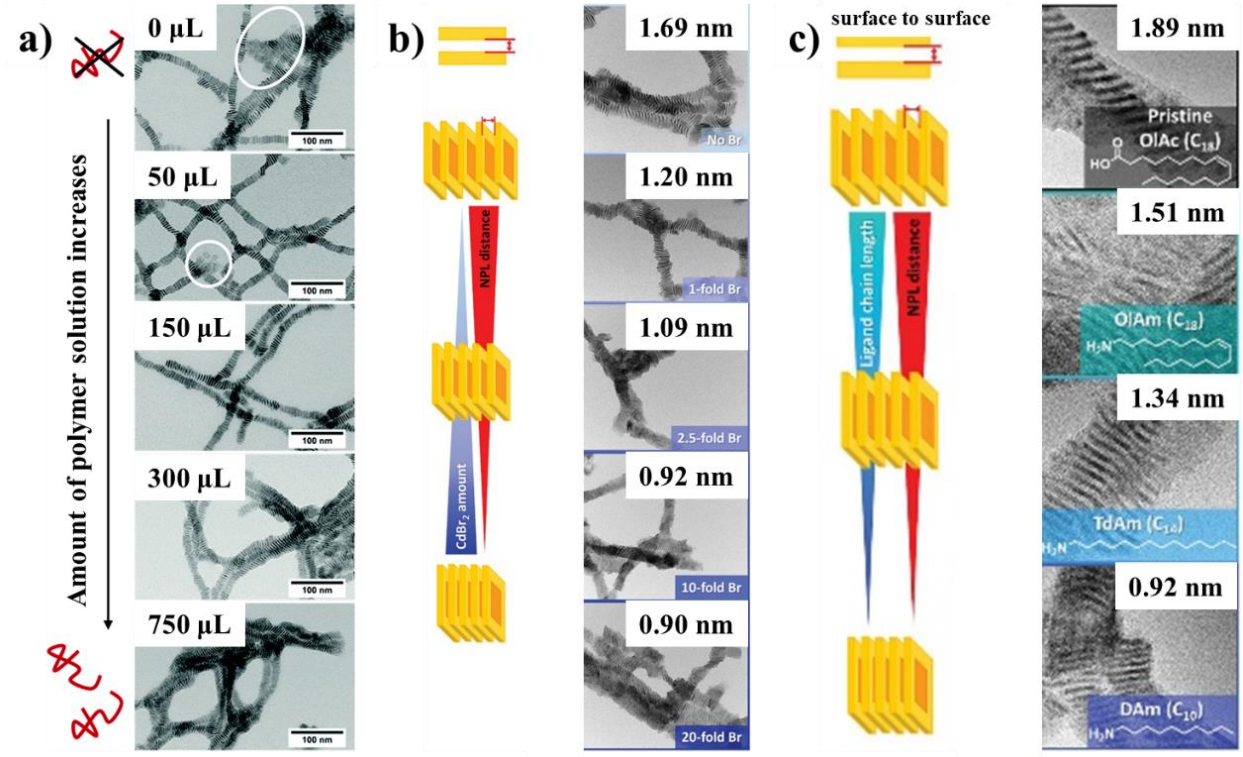


**Figure 1-15.** (a) TEM micrographs of polymer-encapsulated NPLs stacks without (a) and with ligand exchange of different amounts of $CdBr_2$ (b) and different lengths of amine (c).[69] (Reprinted with permission from ref. 69, Copyright 2022, John Wiley and Sons.)

### 1.3.4.2 Thermal annealing method

Thermal annealing is an intuitive but nontrivial method to tune the physical (ductility and hardness) or chemical properties (stability) of the material, by e.g., removing surface ligands. The annealing process normally includes three stages: heating to the desired temperature, holding or "soaking" at this temperature, and cooling down to room temperature. Annealing temperature and time are important parameters in annealing procedures. The treatment can be a double-edged

sword: PL may be quenched due to the formation of trap states, surface ligands will be removed, and the size of NCs may be increased. On the other hand, a significantly stronger photocurrent appears after thermal annealing due to enhanced inter-NC coupling for free carrier generation and transport (Figure 1-16).

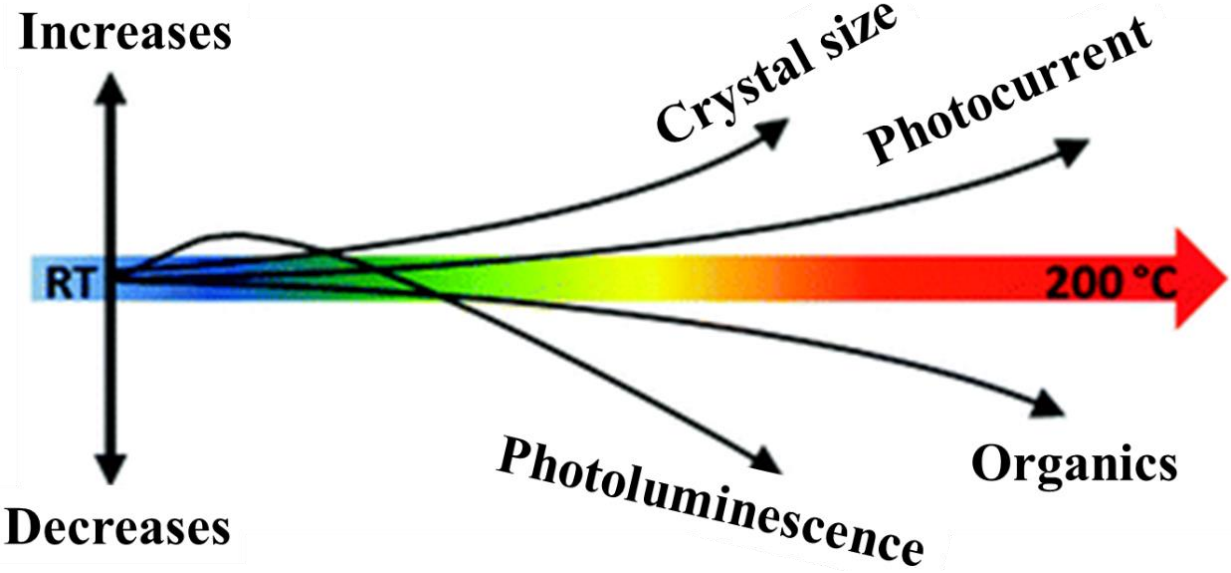


**Figure 1-16.** The temperature-dependent photoluminescence, photocurrent, organics, and crystal sizes.[70] (Reprinted with permission from ref. 70, Copyright 2016, Royal Society of Chemistry.)

Furthermore, organic ligands are quickly removed from the supported nanocrystals by a fast thermal treatment in the air.[71] During the treatment, the heating and cooling ramps are in the order of tens of degrees per second, similar to rapid annealing procedures used in the semiconductor industry. With this fast treatment, kinetic transformations are favored over thermodynamics, preventing the system from relaxing to sintering. This fast thermal treatment method is also widely applicable to NCs with different compositions, sizes, and shapes. Yet, thermal annealing sometimes performs coking from incomplete ligand pyrolysis, and high temperatures (~400 °C) are easy to induce the loss of quantum confinement and conductivity. Hence, Brutchey et al. combined thermal annealing and ligand exchange methods to get improved interparticle coupling, better colloidal stability, lower organic content, and increased photocurrent response (Figure 1-17a).[72] Jang et al. used ligand washing/exchange methods for the preliminary ligand removal and annealing process as the second step to remove most of the remaining ligands (Figure 1-17b).[73]

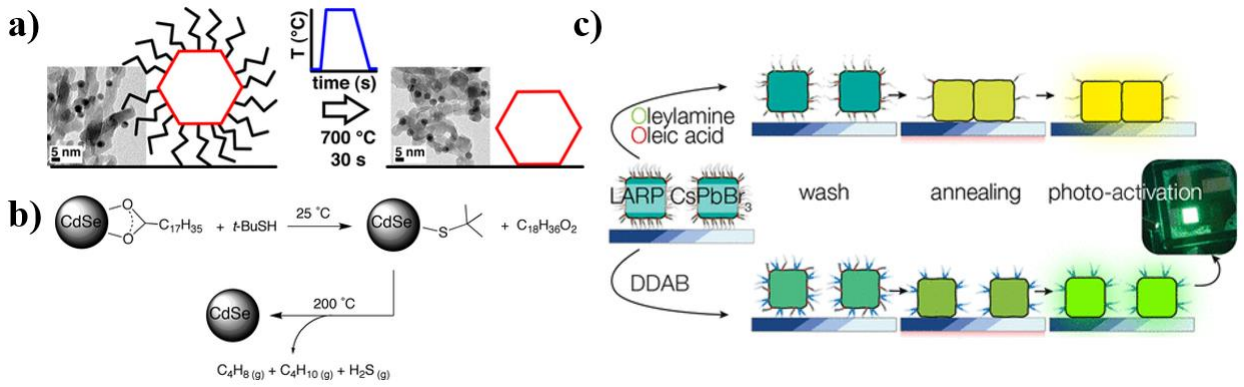


**Figure 1-17.** (a) Efficient removal of organic ligands by thermal annealing.[71] (Reprinted with permission from ref. 71, Copyright 2015, American Chemical Society.) (b) Ligand exchange on CdSe NCs by thermal annealing for improving photocurrent.[72] (Reprinted with permission from ref. 72, Copyright 2012, American Chemical Society.) (c) Surface engineering of perovskite QDs for efficient LEDs.[73] (Reprinted with permission from ref. 73, Copyright 2018, American Chemical Society.)

# Chapter 2: THz Spectroscopy and Sample Preparation

## 2.1 THz basics

In the thesis, we employ THz spectroscopy to investigate the colloidal stability as well as the charge carrier dynamics of NPLs in dispersion or thin films. We provide the fundamental basis on the THz spectroscopies including how it is generated, detected and what physical properties we can learn.

### 2.1.1 Introduction of THz spectroscopy

Lying between the microwave and infrared regions of the electromagnetic spectrum, Terahertz (THz, $10^{12}$ Hz) radiation consists of waves with frequencies between $10^{11}$ and $10^{13}$ Hz (i.e. 0.1-10 THz, or equivalently wavelengths between 30 μm and 3 mm). In the past twenty years, with the rapid development of effective generation and detection methods,[74,75] THz radiation has been widely employed as novel light sources to probe low-energy resonances (e.g. vibrational or phonon dynamics in solids), and charge carrier dynamics in semiconductors.[76,77,78]

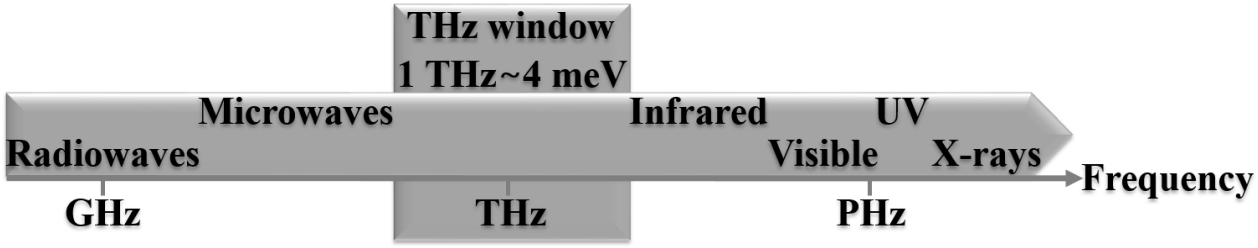


**Figure 2-1.** The location of the terahertz window in the electromagnetic spectrum.

### 2.1.2 THz generation

#### 2.1.2.1 THz generation from the photoconductive antenna

One of the first developed methods for THz generation is based on the photoconductive antenna mechanism. The basic THz radiation principle of the photoconductive antenna is shown in Figure 2-2.

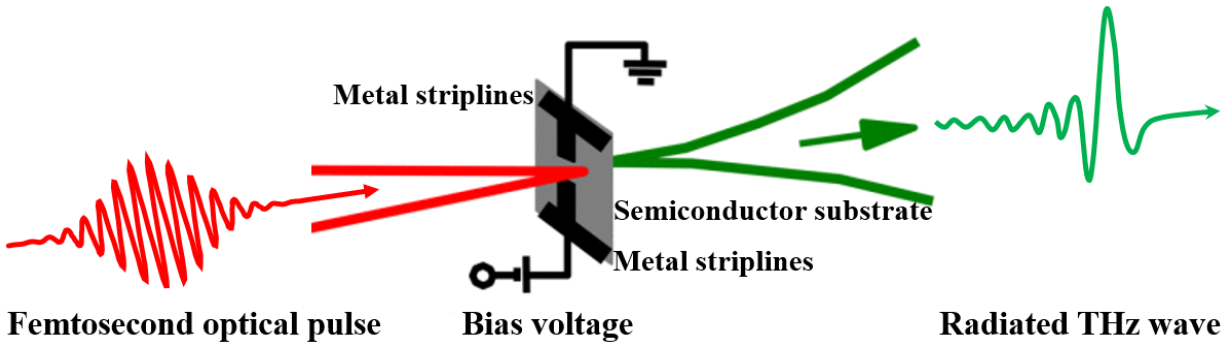


**Figure 2-2.** Schematic demonstration of THz generation based on the photoconductive antenna.[79] (Reprinted with permission from ref. 79, Copyright 2011, IEEE.)

A pair of metal strip lines (electrodes) with a μm gap is deposited on top of a semiconductor substrate (e.g., Si, InAs, and ZnTe).[80] A bias voltage ($V_b$) creates an electric field between the electrodes. When a femtosecond optical pulse illuminates the gap between electrodes, the photogenerated carriers of semiconductors in the gap could be accelerated by the external bias electric field.[81] Time-dependent transient current is expressed as:[82]

$$J(t) = N(t)e\mu_e E_{dc} \ (Equation\ 2.1)$$

Where $N(t)$ is the time-dependent density of photogenerated carriers, and $\mu_e$ is the carrier mobility. A fast current pulse $J(t)$ is set by the laser pulse duration, and RC time constant of the photoconductive antenna, and influenced by the carrier recombination dynamics. A fast decay time in the sub-ps to ps time scale enables it to cover a wide range of THz frequencies. The relationship between the generated THz (with a field strength of $E_{THz}$) and the current follows:[83]

$$E_{THz}(t) \propto \frac{1}{4\pi\varepsilon_0 c^2}\frac{dJ(t)}{\partial t} \ (Equation\ 2.2)$$

Where $\varepsilon_0$ is the vacuum permittivity, and $c$ is the speed of light in the vacuum.

The advantage of THz generation by photoconductive antenna lies in the achievable low background noise and thus high signal-to-noise ratio (e.g. over 1:100000).[84] On the other hand, the bandwidth of the THz emission largely relies on the photoresponse (e.g. the lifetime) of charge carriers, which is not always easy to control. Charge carriers in photoconductive semiconductor substrates with a relatively slow response often limit the high-frequency performance.[85] More importantly, high excitation often leads to the saturation of THz emission.[86]

#### 2.1.2.2 THz generation from optical rectification

Optical rectification (OR) is a second-order nonlinear optical process. It occurs only in non-centrosymmetric electro-optic crystals such as Zinc Telluride (ZnTe), Gallium Phosphide (GaP),

or Gallium Selenide (GaSe). The basic THz radiation principle of optical rectification is shown in Figure 2-3.

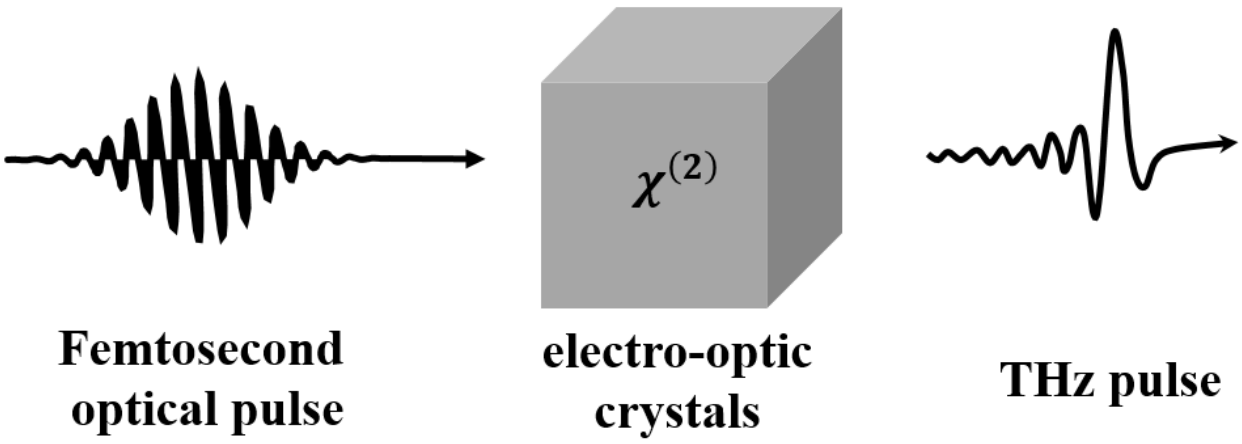


**Figure 2-3.** Schematic process of THz generation from optical rectification.

When the laser pulse interacts with the nonlinear medium, a low-frequency or even a *dc* electric polarization field can be generated to drive THz pulse generation. In 1962, Bass et. reported the phenomenon of OR.[87] In the report, they observed a dc polarization when an intense ruby laser was transmitted through potassium dihydrogen phosphate (KDP) and potassium di-deuterium phosphate ($KD_dP$) crystals.

In principle, the polarization $P$ generated in the medium by the incident optical pulse electric field $E$ can be expressed as:

$$P = \varepsilon_0\left(\chi^{(1)}E + \chi^{(2)}EE + \chi^{(3)}EEE + \cdots\right) \ (Equation\ 2.3)$$

Here $\chi^{(1)}$ is known as linear susceptibility, while $\chi^{(n)}$ (with n>1) is a n-order nonlinear coefficient. $\chi^2$ describes the second nonlinear optical effect, including OR.

To describe OR for THz generation, we start with a simple continuous wave (CW) with a frequency $\omega$ and amplitude $E_0$ following:

$$\bar{E}(t) = E_0 cos(\omega t) \ (Equation\ 2.4)$$

For a given laser beam with an electric field $\bar{E}(t)$. The second-order polarization is given by:

$$\bar{P}_2(t) = \varepsilon_0\chi^{(2)}E^2(t) = \varepsilon_0\chi^{(2)}E_0^2 cos(2\omega t) + \varepsilon_0\chi^{(2)}E_0^2 \ (Equation\ 2.5)$$

In the expanded form, the components of $cos(2\omega t)$ and $\varepsilon_0\chi^{(2)}E_0^2$ describe the second-harmonic generation (SHG*)* and optical rectification, respectively.

In a real situation, phase matching in nonlinear crystals (the crystal orientation, thickness, and dispersion) should be considered for THz generation from optical rectification. As the most

commonly used nonlinear crystals, ZnTe (several hundreds of μm thick) is used for THz generation of 0.1–3 THz via optical rectification. A 50 $\mu$m thick GaSe crystal is used for the generation of a higher THz frequency (31 THz).[88,89]

### 2.1.3 THz detection

#### 2.1.3.1 THz detection by photoconductive antenna

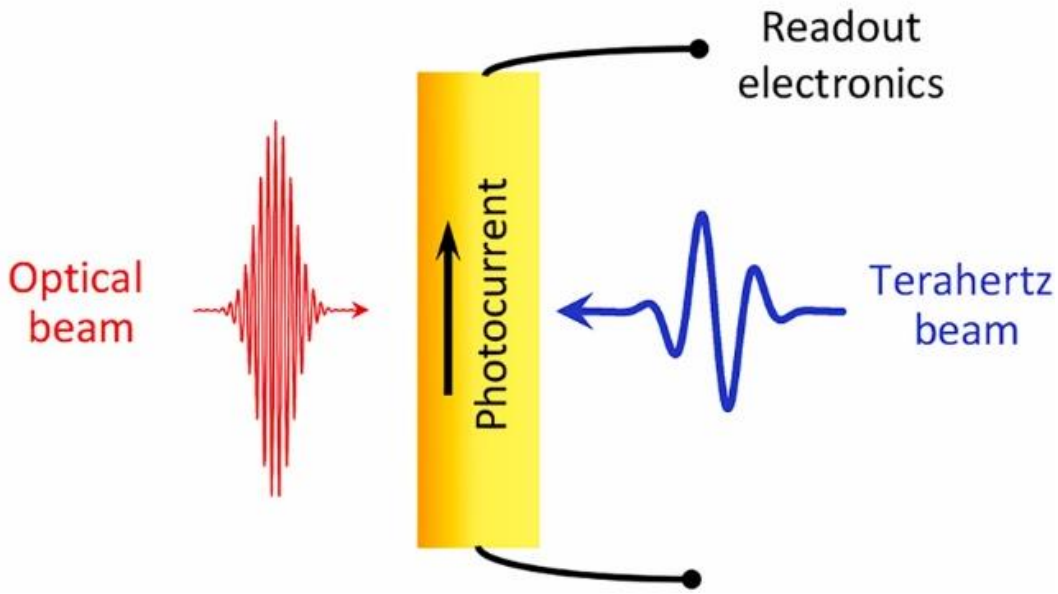


**Figure 2-4**. Schematic process of THz detection from the photoconductive antenna.[90]

Like the generation process, the detection of THz electromagnetic transients based on a femtosecond laser can be achieved by either photoconductive or nonlinear optical methods. The process of photoconductive antenna detection of THz is shown in Figure 2-4, and the process is opposite to the principle of the photoconductive antenna to generate THz.[82] Here, the photoconductor antenna receives the THz beam, which can accelerate the pump-induced photocarriers. The resulting photocurrent is proportional to the convolution of the terahertz field and the laser-induced photoconductivity. The THz field-induced current is expressed:

$$\bar{J}(t) = \bar{N} e \mu_e E(\tau) \ (Equation\ 2.6)$$

Here, $\bar{N}$ describe the average electron density in the photoconductive antenna and $\tau$ is the time delay between the THz pulses and the incident femtosecond optical pulse.

After passing through the external amplifying circuit and the lock-in amplifier, the amplified weak current value can be read out. This current is proportional to the THz electric field.

### 2.1.3.2 THz detection by electro-optic sampling

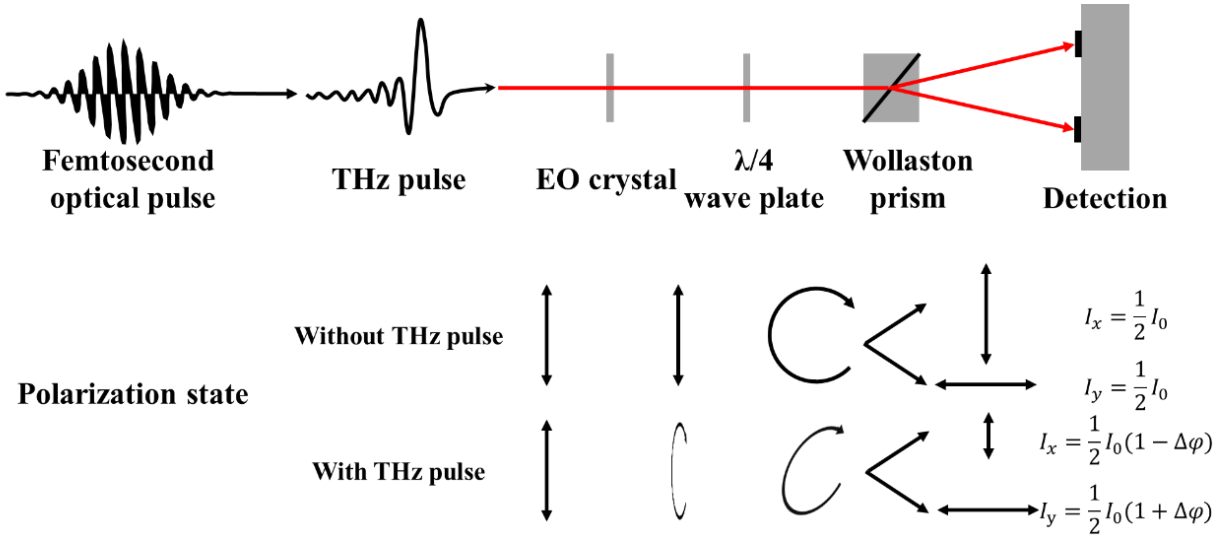


**Figure 2-5.** Schematic process of THz detection from the electro-optic sampling.

In addition to the photoconductive antenna for THz detection, the electric optical (EO) sampling technique has been widely used to detect THz pulses. The EO sampling technique utilizes the Pockels effect of EO crystals such as ZnTe, and GaP, probing the THz pulse with a femtosecond optical pulse.[91,92] The Pockels effect is a linear electro-optic effect in which the THz field induces birefringence in the nonlinear crystal; the induced birefringence is directly proportional to the THz electric field. Thus, the THz electric field can be determined by a change in the polarization state of the probe beam. A typical schematic diagram is shown in Figure 2-5. Without THz pulse, a linearly polarized probe pulses through the EO crystal and maintains its polarization states. By propagating through a quarter-wave plate and becoming circularly polarized. A Wollaston prism is further used to separate two orthogonally polarized components which can be detected by a pair of balanced detectors. Finally, the lock-in amplifier measures two signals, giving reading without the THz pulse:

$$I_x = \frac{1}{2} I_0 \ (Equation\ 2.7)$$

$$I_y = \frac{1}{2} I_0 \ (Equation\ 2.8)$$

Here, $I_0$ is the total intensity of the probe beam. $I_x$ and $I_y$ are signals from two photodiodes, respectively.

On the other hand, when the THz and probe pulse through the EO crystal together, the THz field induces birefringence in the EO crystal. This rotates the probe pulse polarization, making it elliptical and causing an imbalance between $I_x$ and $I_y$:

$$I_x = \frac{1}{2} I_0(1 - \Delta\varphi) \ (Equation\ 2.9)$$

$$I_y = \frac{1}{2} I_0(1 + \Delta\varphi) \ (Equation\ 2.10)$$

Here, $\Delta\varphi$ is the phase retardation between the two polarizations.

This difference between the $I_x$ and $I_y$ give the information about the THz pulse by using the following equation:

$$I_s = I_y - I_x = I_0 \Delta\varphi \propto E_{THz} \ (Equation\ 2.11)$$

## 2.2 Experimental setup

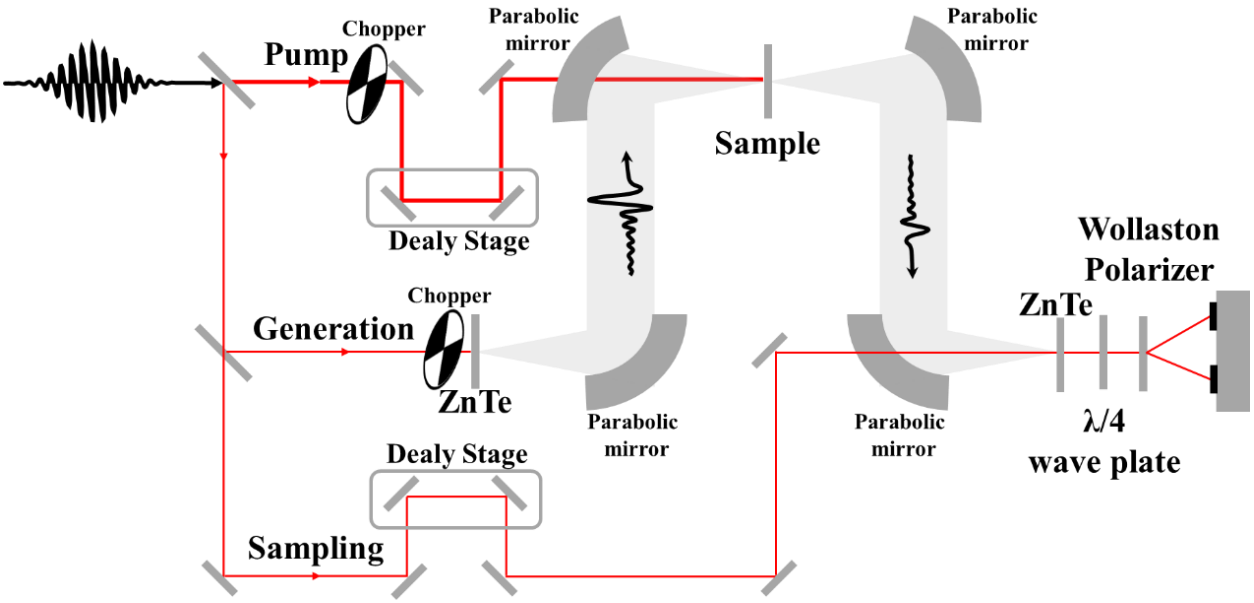


**Figure 2-6**. Schematic diagram of the THz setup employed in this thesis.

The system used in the experiment of this thesis is shown in Figure 2-6. The laser source is a Ti: sapphire regenerative amplifier system that generates pulses of central wavelength λ = 800 nm (1.55 eV). The pulse duration is ~ 50 fs. An ultrafast laser pulse is mainly divided into three parts: a pump, a generation, and a sampling beam. In detail, the pump is used to photo-excite the sample. The pump beam can be up-converted into 3.1 eV by second harmonic generation in a BBO or any

energies between 0.4 to 4.1 eV by an optical parametric amplifier (OPA). The reflected part of the light pulse is further split into a sampling and a generation beam. The generation beam through a 1-mm-thick ZnTe crystal generates THz pulses for probing the conductivity of samples. The pump and probe pulses were synchronized with a controllable delay (τ). In the following, we are going to introduce the experiments performed in our thesis based on this setup.

**Optical–pump terahertz–probe spectroscopy**

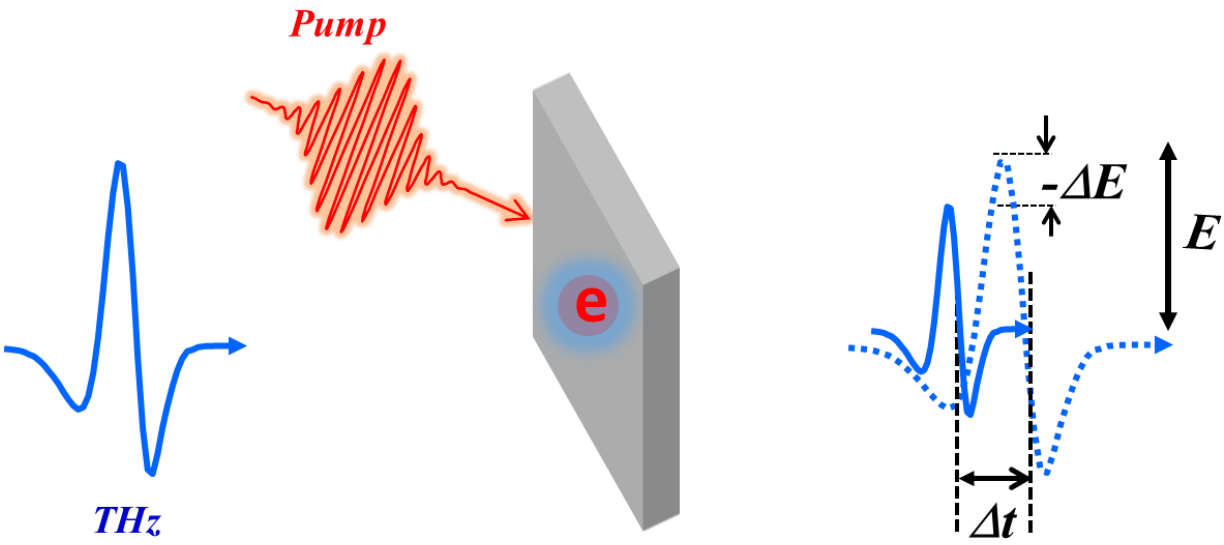


**Figure 2-7.** Schematics for the OPTP spectroscopy. The change in conductivity induced by the pump (in red), e.g. photoconductivity Δσ, is probed by a THz pulse (in blue). The relative change in the THz transmission (−ΔE/E) is linearly proportional to the real part of Δσ. The shift of the incoming THz-field E ($\Delta t$) comes from the presence of charge carriers (e.g. exciton and/or free carriers).

To shed light on charge carrier dynamics in NPL dispersion or solids, we employ optical-pump THz probe (OPTP) spectroscopy. An optical pulse in the VU-vis regime is utilized to excite samples. The THz pulse subsequently probes the conductivity of photogenerated charge carriers i.e. photoconductivity. The time evolution of photoconductivity can then be tracked by controlling the pump-probe delay time. By fixing the sampling time at the peak of the THz pulse, we can monitor the photo-induced amplitude change in THz transmission ($-\Delta E$). On the other hand, excitons as charge-neutral species, mainly induce a phase shift ($\Delta t$) in THz probe pulses.

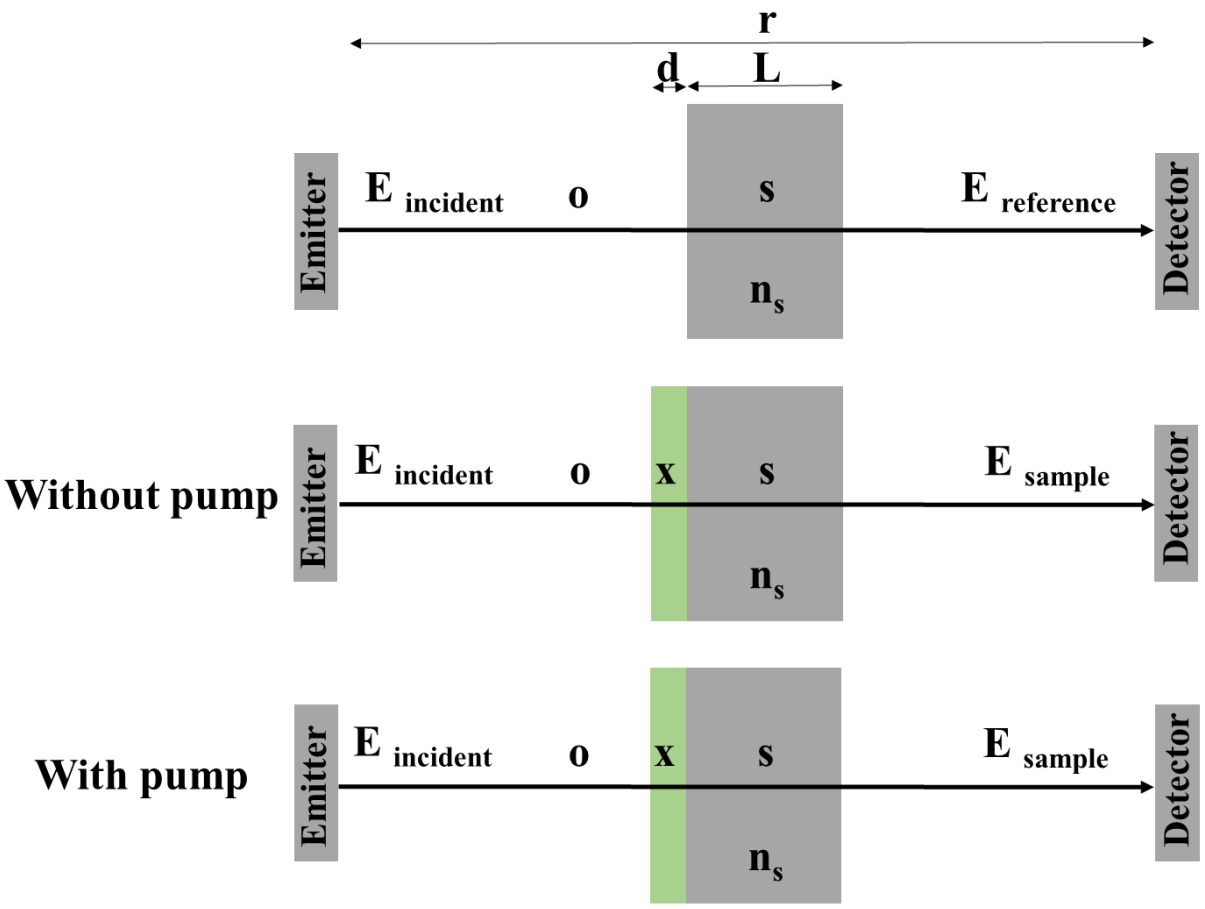


**Figure 2-8.** Propagation of the reference and sample signals through air and film on a substrate.

To determine the frequency-resolved complex THz conductivity of the material, we need to record the THz field transmitted through the reference substrate (e.g., fused silicon substrates in our studies) $E_{ref}$, and the sample $E_{sam}$. Such a sample geometry, as depicted in Figure 4-1, is directly used in my thesis to quantify the charge transport of NPL solids (with 10s of nm thickness) deposited on the fused silicon. Here o, $x$, $s$, and n represent the surrounding air, sample, supporting substrate, and refractive index, respectively. L and d are the thicknesses of the reference substrate and sample, respectively. Here r is the distance between the emitter and detector. We discuss two situations for extracting the (photo) conductivity $\sigma$ of samples without and with photoexcitation.

For studying the static conductivity of the sample, i.e. when there is no photoexcitation, the reference signal $E_{ref}$ and the sample signal $E_{sam}$ are as follows, according to Figure 2-8.

$$E_{ref} = E_{incident} * e^{i\omega(r-L)/c} * t_{os} * e^{i\omega L n_s/c} * t_{so} * MR_s \ (Equation\ 2.12)$$

$$E_{sam} = E_{incident} * e^{i\omega(r-L-d)/c} * t_{ox} * e^{in_x\omega d/c} * t_{xs} * MR_x * e^{in_s\omega L/c} * t_{so} * MR_s \ (Equation\ 2.13)$$

$MR_x$ and $MR_s$ are the multiple reflections of the sample and substrate, given by:

$$MR_x = \left[1 + r_{ox} * r_{xs} * e^{2in_x\omega d/c}\right]^{-1} \ (Equation\ 2.14)$$

$$MR_s = \left[1 + r_{xs} * r_{so} * e^{2in_s\omega L/c}\right]^{-1} \ (Equation\ 2.15)$$

$$T = \frac{E_{sam}}{E_{ref}} = \frac{e^{-i\omega d/c}}{t_{os}} * \frac{e^{in_x\omega d/c} * t_{0x} * t_{xs}}{1 + r_{ox} * r_{xs} * e^{2in_x\omega d/c}} \ (Equation\ 2.16)$$

Here $t_{xy}$ ($t_{os}$, $t_{ox}$, $t_{xs}$, or $t_{so}$) is Fresnel field transmission coefficients and $r_{xy}$ ($r_{ox}$or $r_{xs}$) is Fresnel field reflection coefficients. These are given by:

$$t_{xy} = \frac{2n_x}{n_y + n_x}; r_{xy} = \frac{n_y - n_x}{n_y + n_x} \ (Equation\ 2.17)$$

When the $n_o = 1$(refractive index of air),

$$\mathrm{T} = \frac{n_x(1 + n_s)e^{-i\omega d/c}}{n_x(1 + n_s) * \cos(n_x\omega d/c) - i(n_x^2 + n_s) * \sin(n_x\omega d/c)} \ (Equation\ 2.18)$$

When the thickness of the material is smaller than the THz wavelength d ≪ λ, thereby we could reduce the above longer equation to the short expression as:

$$T = \frac{(1 + n_s)}{(1 + n_s) - in_x^2\,\omega d/c} \ (Equation\ 2.19)$$

This is the so-called thin-film approximation.

For the refractive index of the sample ($n_x$), the permittivity of the sample ($\varepsilon_x$) is given by

$$\varepsilon_x = n_x^2 \ (Equation\ 2.20)$$

The photoconductivity $\sigma$, permittivity, and refractive index of the sample are related as

$$\sigma = -i\omega\varepsilon\varepsilon_0 = -i\omega n_x^2\varepsilon_0 = -i\omega n_x^2/Z_0\mathrm{c} \ (Equation\ 2.21)$$

Here $Z_0 = \mathrm{c}\varepsilon_0$ is the impedance of free space (for the conductive film). Then, we rewrite the formula using $i\sigma Z_0 = -in_x^2\omega/\mathrm{c}$.

$$T = \frac{(1 + n_s)}{(1 + n_s) + i\sigma Z_0 d} \ (Equation\ 2.22)$$

Therefore, the photoconductivity reads as:

$$\sigma = \frac{(1 + n_s)}{Z_0 d}\left(\frac{E_{ref} - E_{sam}}{E_{sam}}\right) \ (Equation\ 2.23)$$

When the sample is photoexcited,

$$\sigma_{umpump} = \frac{(1 + n_s)}{Z_0 d}\left(\frac{E_{ref} - E_{unpump}}{E_{unpump}}\right) \ (Equation\ 2.24)$$

$$\sigma_{pump} = \frac{(1+n_s)}{Z_0 d}\left(\frac{E_{ref} - E_{pump}}{E_{pump}}\right) \ (Equation\ 2.25)$$

The pump-induced conductivity change, e.g. photoconductivity $\Delta\sigma$ can be defined as:

$$\Delta\sigma = \sigma_{pump} - \sigma_{umpump} = \frac{(1+n_s)}{Z_0 d}\left(\frac{E_{ref} - E_{pump}}{E_{pump}}\right) - \frac{(1+n_s)}{Z_0 d}\left(\frac{E_{ref} - E_{unpump}}{E_{unpump}}\right)$$

$$= \frac{(1+n_s)}{Z_0 d}\left\{\left(\frac{E_{ref} - E_{pump}}{E_{pump}}\right) - \left(\frac{E_{ref} - E_{unpump}}{E_{unpump}}\right)\right\}$$

$$= \frac{(1+n_s)}{Z_0 d}\left(\frac{E_{ref}\,E_{unpump} - E_{ref}\,E_{pump}}{E_{pump}\,E_{unpump}}\right)$$

$$= \frac{(1+n_s)}{Z_0 d}\frac{E_{ref}}{E_{pump}}\left(\frac{E_{unpump} - E_{pump}}{E_{unpump}}\right)$$

$$= -\frac{(1+n_s)}{Z_0 d}\frac{\Delta E}{E_{unpump}}\left(\frac{E_{ref}}{E_{pump}}\right) \ (Equation\ 2.26)$$

As shown previously, $\frac{E_{ref}}{E_{pump}} = \frac{1}{T} = \frac{(1+n_s)+i\sigma Z_0 d}{(1+n_s)}$ $(Equation\ 2.27)$

By applying the thin-film approximation (as $d \ll \lambda$), one can neglect the contribution of the imaginary term, so that:

$$\frac{E_{ref}}{E_{pump}} \cong \frac{(1+n_s)}{(1+n_s)} = 1 \ (Equation\ 2.28)$$

This leads to the final photoconductivity form:

$$\Delta\sigma = -\frac{(1+n_s)}{Z_0 d}\frac{\Delta E}{E_{unpump}}\left(\frac{E_{ref}}{E_{pump}}\right) = -\frac{(1+n_s)}{Z_0 d}\frac{\Delta E}{E_{unpump}} \text{ or } -\frac{(1+n_s)}{Z_0 d}\frac{\Delta E}{E} \ (Equation\ 2.2)$$

## 2.3 Conductivity models

### 2.3.1 Drude model

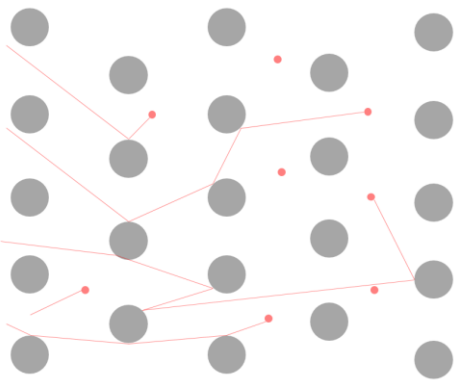

**Figure 2-9.** Schematic diagram of the Drude model electrons (shown in red) constantly bouncing between the heavier, relatively fixed positive ions (shown in grey).

In the Drude model, electrons and holes are treated as ideal classical gas, and their scattering to the lattice or defects are assumed to take place through a momentum randomized scattering event with a mean scattering time τ.

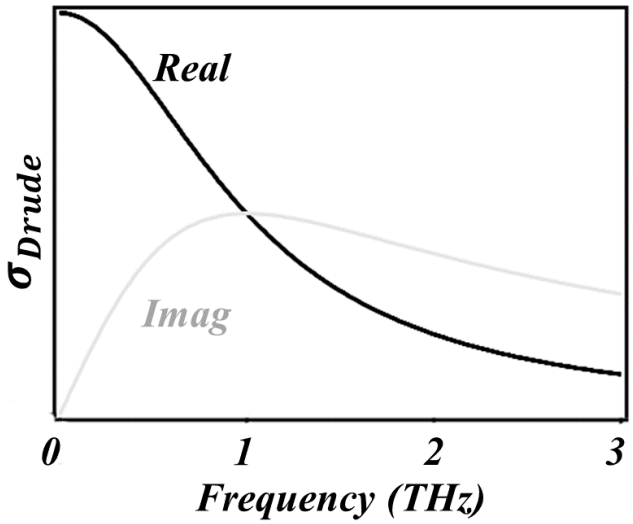


**Figure 2-10.** Drude conductivity versus angular frequency times scattering time.

#### 2.3.1.1 Deriving the Drude conductivity

We treated the conduction of charges classically following Newton's second law of motion. By applying a time-varying electric field $E(t)$ to electrons with drift velocity $V_d$ and an effective mass of $m$, the equation of motion for electrons reads:

$$F = ma = m\frac{dV_d}{dt} = m\frac{d^2r}{dt^2}$$

Here, r represents displacement and a is acceleration.

Two forces are acting on the charge carrier: the electric force $-eE(t)$ and the force caused by collisions $-F = -m\frac{V_d(t)}{\tau}$. By applying the equation of motion, we obtain:

$$m\frac{V_d}{\tau} = -eE(t) - m\frac{V_d(t)}{\tau}$$

$$-\frac{e}{m}E(t) = \frac{dV_d(t)}{dt} + \frac{V_d(t)}{\tau}$$

For a giving electric field with angular frequency $\omega$:

$$E(t) = E_0 e^{-i\omega t}$$

The drift velocity of carriers depends on the applying time-varying $E(t)$:

$$V_d(t) = V_0 e^{-i\omega t}$$

$$-\frac{e}{m}E_0 e^{-i\omega t} = \frac{d(V_0 e^{-i\omega t})}{dt} + \frac{V_d}{\tau} = V_0 e^{-i\omega t} * (-i\omega) + V_d e^{-i\omega t}/\tau = V_d(1 - i\omega\tau)/\tau$$

By converting the formula, we obtain the drift velocity as:

$$V_d(t) = E_0 e^{-i\omega t}\frac{e\tau}{m}\frac{1}{1 - i\omega\tau}$$

The carrier mobility $u$ can be defined as the proportionality factor between the drift velocity and the applied electric field:

$$u(\omega) = \frac{V_d(t)}{E(t)} = \frac{e\tau}{m}\frac{1}{1 - i\omega\tau}$$

The conductivity is the mobility of elections times the density of electrons $N$:

$$\sigma_{Drude}(\omega) = Neu(\omega) = \frac{Ne^2\tau}{m}\frac{1}{1 - i\omega\tau}$$

With the plasma frequency $\omega_p = \sqrt{\frac{e^2 N}{\varepsilon_0 m}}$,

$$\sigma_{drude}(\omega) = \frac{\omega_p^2 \varepsilon_0 \tau}{1 - i\omega\tau}$$

### 2.3.2 Drude-Smith model

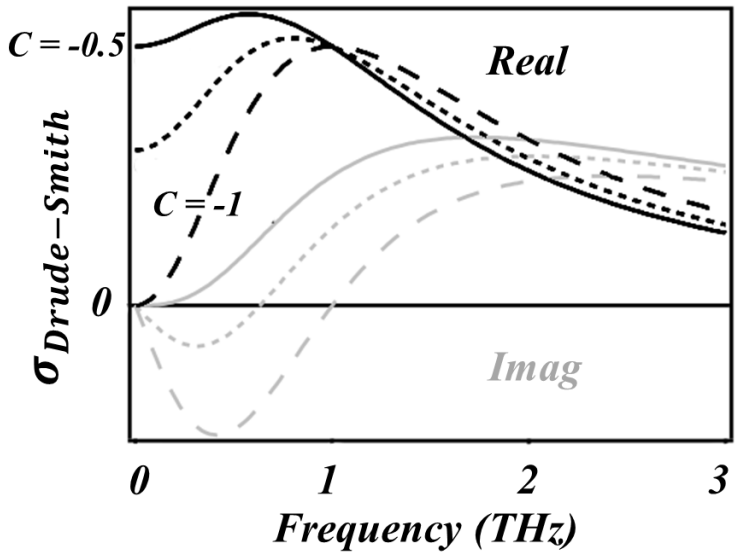


**Figure 2-11.** Drude-Smith conductivity versus angular frequency times scattering time for backscattering parameters.

In nanoscale materials with finite boundaries, the assumption of complete momentum randomizing scatting in the Drude model may be no longer valid (e.g. strong backscattering events to the grain boundaries).[93] As a modified version of the Drude model, the Drude-Smith model takes into account the possibility that charge carriers are scattered at e.g. grain boundary, leading to preferentially backward scattering, following:

$$\sigma_{Drude-Smith} = \frac{\omega_p^2 \varepsilon_0 \tau}{1 - i\omega\tau} * \left(1 + \frac{c}{1 - i\omega\tau}\right)$$

Here c is a parameter to describe the backscattering effect, which can vary between 0 and -1: while c = 0 describes full momentum randomized scattering (the classical Drude model) and c = −1 describes a full backscattering event.

## 2.4 Sample preparation

In this thesis, 4 ML CdSe NPLs were used for the THz spectroscopy study. In the following, we prepare experimental details on the sample preparation and thermal treatments.

### 2.4.1 Preparation of 4 ML CdSe NPLs

#### Chemicals

All reagents were purchased and used without further purification. 1-Octadecene (ODE, Technical Grade, 90 %, 1 L), oleic acid (OA, Technical Grade, 90 %, Sigma-Aldrich, 1 L), myristic acid (> 98%, Sigma-Aldrich, 500 g), cadmium acetate dihydrate ($Cd(OAc)_2.2H_2O$, 98%, Acros Organics, 50 g), Se (99.999 %, Alfa Aesar, 50 g), CdO (99%, Fisher Scientific, 250 g), trifluoroacetic anhydride (TFAA, TCI, Tokyo Chemical Industry, 100 mL), trifluoroacetic acid (99.5%, TFA, Tokyo Chemical Industry, 100 mL), triethylamine (99.5%, TEA, Alfa Aesar, 1 L), methanol (MeOH, HPLC Grade, VWR Chemicals, 5 L). N-Hexane (≥ 95%, Analytical Reagent Grade, 5 L) and acetonitrile ($CH_3CN$, HPLC grade, 2.5 L) were purchased from Fisher Scientific Chemical. Methyl acetate (99%, HPLC grade, 2.5 L) was purchased from Merck KGaA.

#### Synthesis of Cadmium myristate [$Cd(myristate)_2$]

Cadmium myristate ($Cd(myr)_2$) was synthesized following the procedure described by Rossinelli et al.[94] In a typical synthesis of a 100 mL three-necked flask, 5.75 g (44.78 mmol) of

CdO and 20 mL of acetonitrile were mixed and stirred at room temperature (RT, 500 rpm). And then, 0.7 mL (9.15 mmol) of trifluoroacetic acid (TFA) and 6.2 mL (43.98 mmol) of trifluoroacetic anhydride (TFAA) were slowly added to the mixture. Then, the mixture was stirred for an additional 10 min at RT. Afterward, the reaction mixture was heated up to 50 °C under stirring for 60 min. In another 500 mL beaker, 100 mL of 2-propanol, 14 mL (100.44 mmol) of triethylamine (TEA), and 10.23 g (44.80 mmol) of myristic acid were mixed. Then the cadmium trifluoroacetate solution was added slowly to the 500 mL baker while stirring (500 rpm). The product-white precipitate was vacuum-filtered and washed several (more than 4) times with 50 mL of cold methanol. Finally, the final product was collected, dried in a vacuum oven at 40 °C overnight, and stored under ambient conditions for further use.

**Synthesis of 4 Monolayer (4 ML) CdSe NPLs with varied lateral sizes nm (NPLs-5, 10, 15, and 20)**

The 4 ML CdSe NPLs were prepared by modifying the procedure published by Rebecca et al.[58] In a typical synthesis of a 100 mL three-necked flask, 170 mg (0.3 mmol) of $Cd(myr)_2$, 12 mg (0.15 mmol) of Se, and 15 mL of ODE were mixed. Then the mixture was degassed under a vacuum, heated up to 100 °C in 10 min, and refluxed at 100 °C for 13 min. Then, we turn off the vacuum and turn on the argon. Based on the inert atmosphere, the solution was heated up to 240 °C within 16 min. 80 mg (0.3 mmol) of $Cd(ac)_2.2H_2O$ was added quickly to the mixture at 188 °C. After 6 min at 240 °C, the reaction mixture was quickly cooled down by a water bath. During the cooling step, 0.5 mL of OA was added at 185 °C. Finally, 5 mL of hexane was added to the mixture and centrifuged at 5000 rpm for 5 min. The supernatant was discarded, and the precipitate was dispersed in 5 mL hexane and centrifuged at 8000 rpm for another 5 min. The supernatant (4 ML+3 ML) was collected and stored. After one week, the remaining 3 ML NPLs precipitated could be removed by centrifugation at 8000 rpm for 5 min. The 4 ML NPLs in hexane were precipitated by using methyl acetate in a 1:1 volume ratio to remove residual ODE and oleic acid. Finally, the mixture was stored in the fridge at 5 °C for 1 h followed by another centrifugation at 8000 rpm for 10 min. The precipitate was dispersed in hexane. The dispersed NPLs could be stored in hexane for several months. By tuning the reaction time to 5- 8 min at 240 °C, one can readily control the lateral size of NPLs from 5*5 to 20*20 $nm^2$.

### 2.4.2 Thermal annealing treatments

**Thermal annealing treatments of 4 ML CdSe NPLs in the air at different temperatures**

A solution drop-casting method was used to prepare the 4 ML CdSe NPLs film. 20 μL solutions of as-synthesized NPLs ($1.07 \times 10^{-6}$ M, based on the absorption) were transferred by pipette and then dropped on cleaned fuse silicon (1 cm × 1 cm). The as-synthesized NPLs film was placed in the middle of a tube furnace and then heated to a targeted temperature (200, 225, 250, 300, 325, 335, 340, or 350 °C) for 30 min with a heating rate of 5 °C $min^{-1}$ in the air. Finally, it was naturally cooled down to room temperature in 120 min. The obtained samples were named NPLs-X °C.

**Thermal Annealing Treatments of 4 ML CdSe NPLs at 300 °C with Different Gas**

The process was the same as described in the rapid thermal annealing treatment in the air at different temperatures except that the gas atmosphere is argon or hydrogen. The temperature was kept at 300 °C. Finally, the representative sample was named NPLs-Ar-300 °C or NPLs-$H_2$-300 °C.

**Figure 2-12.** The CVD system used in this thesis.

# Chapter 3: Anisotropic and Hyperbranched InP Nanocrystals via Chemical Transformation of in situ Produced $In_2O_3$

This chapter is based on the following publication:

Anisotropic and hyperbranched InP nanocrystals via chemical transformation of in situ produced $In_2O_3$. Shuai Chen, Andreas Riedinger. Chem. Commun., 2022, 58, 9246. This article is licensed under a Creative Commons Attribution 3.0 Unported Licence. We can use material from this article in other publications without requesting further permissions from the RSC.

My contributions to the project were conceiving and designing the experiments, and synthesis of the InP nanocrystals. Furthermore, I performed transmission electron microscopy characterization of InP nanocrystals. Michael Steiert and Christoph Sieber did the XRD measurements, and Prof. Mischa Bonn attended the fruitful discussions.

## 3.1 Introduction

The synthesis of colloidal nanocrystals (NCs) with regular and controllable morphology and size is at the core of nanomaterials research.[96,97,98] Many synthesis approaches have been developed to produce high-quality nanoparticles, nanorods, nanowires, or other nanostructures for metals, semiconductors, and oxides.[99,100,101,102] The control over morphology and functionalization in preparation and synthesis are important parts of the development of nanotechnology and are the basis for exploring the properties of nanostructures and their applications.[103,104,105]

Indium phosphide (InP) is one of the most widely studied III–V compound semiconductor nanocrystals in colloidal form. InP nanowires (NWs) have attracted considerable interest due to their versatility in electronics and optoelectronics.[106,107,108,109] And InP quantum dots are drawing a large interest as a potentially less toxic material for lighting applications and electrochemical reduction of $CO_2$.[110,111,112] Potentially, there are still many different shapes of InP NCs waiting for their discovery.

Until now, various types of P precursors have been reported to synthesize InP NCs, such as single-source precursor ($In(PBut_2)_3$),[113] magic-sized clusters (MSCs),[114] elemental phosphorus precursor,[115] trioctylphosphine (TOP),[116] $PH_3$ gas,[117] aminophosphine,[118] metal phosphorus ($Na_3P$),[119] and most widely, tris(trimethylsilyl) phosphine $P(SiMe_3)_3$.[120] However, many of these

P precursors, in particular $P(SiMe_3)_3$, are air and water sensitive, hazardous, and/or expensive. Therefore, alternative, safer, and cheaper P precursors are very desirable.

Among various phosphites, triphenyl phosphite (TPOP) would be the most effective P precursor for InP synthesis, since three benzene rings would stabilize the partial charges for In-P monomer formation.[122] Interestingly, TPOP is reported as an effective phosphorus source for synthesizing various metal phosphide nanocrystals such as $Ni_2P$, MoP, $Co_2P$, $Fe_2P$, and $Cu_3P$.[121] Recently, Lee et al. used TPOP to synthesize bulk InP.[122] A black powder appeared after the purification process but was not dispersible in solvents. This is a promising method because TPOP can form InP phases, it is a cheap and non-pyrophoric, non-toxic chemical. However, so far, no control over size and shape with TPOP as a precursor for InP nanomaterials has been reported.

Here, we show how this can be achieved by choosing the right synthetic conditions in the reaction between indium chlorides and carboxylates and TPOP in the presence of hexadecylamine (HDA) in ODE, to yield InP NCs with control over size and shape. We show that by changing the temperature, we mainly gain control over the shape that spans from wires to tetrahedrons to hyperbranched NCs. The size of InP NCs could be controlled by the hot injection of TPOP. We also investigate the formation of InP. We find that $In_2O_3$ is formed first, and converted to InP upon the addition of TPOP.

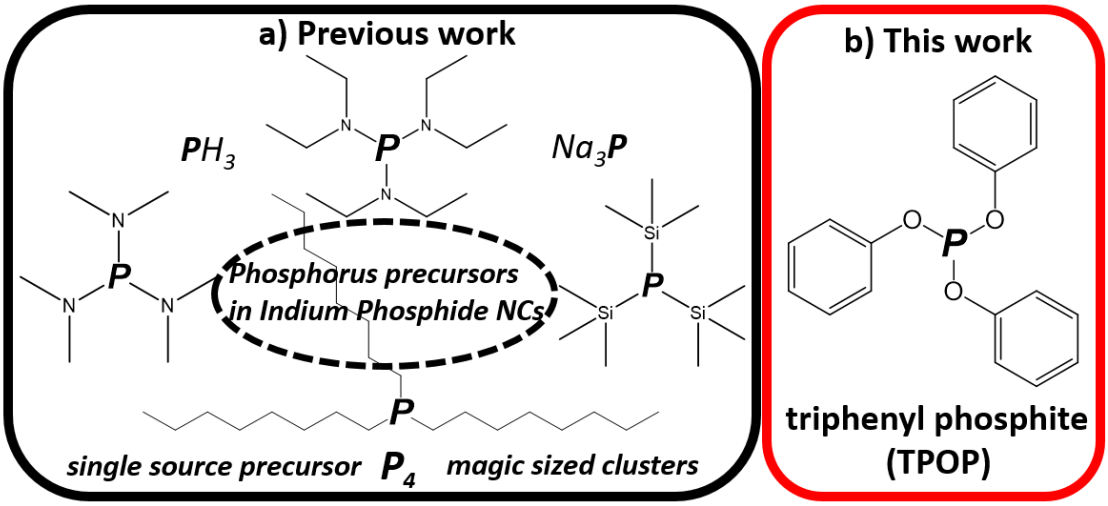


**Figure 3-1.** Phosphorus precursors in the synthesis of indium phosphide NCs.

## 3.2 Experimental part:

### 3.2.1 Chemicals and materials:

All reagents were purchased and used without further purification. 1-Octadecene (ODE), indium chloride, indium oxide, indium bromide, indium iodide, hexadecaneamine (HDA), and triphenyl phosphite (TPOP) were purchased from Acros chemicals.

### 3.2.2 Synthesis of InP nanocrystals

**Synthesis of indium phosphide at different temperatures.** In a typical synthesis, 0.5 mmol of $InCl_3$, and 0.5 mmol $In(ac)_3$ were mixed with 5 mmol of HDA, 1.5 mL of TPOP, and 15 mL of ODE. The obtained mixture was heated under argon flow to 150 °C in 15 min and maintained at this temperature for 60 min to dissolve the metal precursor and to ensure the removal of traces of low-boiling-point impurities. Afterwards, the solution was heated to 230 °C, 235 °C, 255 °C, 300 °C, 320 °C and kept at that temperature for 30 min. Then, the mixture was allowed to cool naturally to room temperature. Finally, NPs were thoroughly purified by multiple precipitations and dispersion steps, using 2-propanol for precipitation and hexane for dispersion.

**Synthesis of indium phosphide with the hot injection of TPOP.** In a typical synthesis, 0.5 mmol of $InCl_3$, and 0.5 mmol of $In(ac)_3$ were mixed with 5 mmol of HDA, and 15 mL of ODE. The obtained mixture was heated under argon flow to 150 °C in 15 min and maintained at this temperature for 60 min. Then, during the second step to heat at 300 °C for 30 min, we added 1.5 mL of TPOP to the reaction at 270 °C. Then, the mixture was allowed to cool naturally to room temperature. Finally, NPs were thoroughly purified by multiple precipitations and dispersion steps, using 2-propanol for precipitation and hexane for dispersion.

**Tracking the reaction process during the synthesis of indium phosphide.** In a 100 mL three-necked flask, $InCl_3$ (0.5 mmol), $In(ac)_3$ (0.5 mmol), HDA (5 mmol), and TPOP (1.5 mL) were mixed in ODE (15 mL). The mixture was heated up to 150 °C in 15 min in an inert atmosphere (argon) and refluxed at 150 °C for 15 min. The solution was heated up to 300 °C within 15 min. At 230 °C, 240 °C, 250 °C, 260 °C, 280 °C, and 300 °C, we took out the sample to measure XRD and TEM.

**Tracking the intermediate states during the heating process with and without TPOP.** In a 100 mL three-necked flask, $InCl_3$ (0.5 mmol), $In(ac)_3$ (0.5 mmol), and HDA (5 mmol) were

mixed in ODE (15 mL). Then the temperature was increased to 150 °C and 270 °C. Later, we got the sample from 150 °C and 270 °C. When the temperature reached 270 °C, we added TPOP to this reaction and took the sample out of this reaction at this temperature. Finally, we measured the PXRD and TEM of those samples.

**Tracking the transition state process of $In_2O_3$ to form InP.** In a 100 ml three-necked flask, $InCl_3$ (0.5 mmol), $In(ac)_3$ (0.5 mmol), and HDA (5 mmol) were mixed in ODE (15 mL). Then the temperature was increased to 150 °C and 270 °C. At 270 °C, we took out the sample one time. Then, we added TPOP to this reaction. After TPOP addition, 5 min, 10 min, 13 min, 15 min, 18 min, 25 min, and 33 min, we took out the samples to measure the XRD to track the transition state process.

**Co-decomposition experiments of chloride ion sources with commercial $In_2O_3$.** In a 100 mL three-necked flask, $NH_4Cl$ (1.5 mmol), ammonium acetate (1.5 mmol), $In_2O_3$ (0.5 mmol), HDA (5 mmol), and TPOP (1.5 mL) were mixed in ODE (15 mL). The mixture was heated up to 150 °C and refluxed at 150 °C for 60 min. Later, the solution was heated up to 300 °C within 15 min and kept at this temperature for 30 min. Finally, NPs were thoroughly purified by multiple precipitations and dispersion steps, using 2-propanol for precipitation and hexane for dispersion.

**Effects of other halides (Br/ I).** In a 100 mL three-necked flask, $InBr_3$/ $InI_3$ (0.5 mmol), $In(ac)_3$ (0.5 mmol), HDA (5 mmol), and TPOP (1.5 mL) were mixed in ODE (15 mL). The mixture was heated up to 150 °C and refluxed at 150 °C for 60 min. Later, the solution was heated up to 300 °C within 15 min and kept at this temperature for 30 min. Finally, NPs were thoroughly purified by multiple precipitations and dispersion steps, using 2-propanol for precipitation and hexane for dispersion.

**The effects of acetic acid.** In a 100 ml three-necked flask, $InCl_3$ (0.5 mmol), $In(ac)_3$ (0.5 mmol), HDA (5 mmol), and TPOP (1.5 mL) were mixed in ODE (15 mL). Later, we added different amounts of acetic acid (10 uL, 20 uL, 30 uL, or 40 uL) in different reactions. The mixture was heated up to 150 °C and refluxed at 150 °C for 60 min. Later, the solution was heated up to 300 °C within 15 min and kept at this temperature for 30 min. Finally, NPs were thoroughly purified by multiple precipitations and dispersion steps, using 2-propanol for precipitation and hexane for dispersion.

### 3.3. Result and discussion

Here, the InP NCs were prepared by a one-pot reaction of indium chloride and indium acetate in a mixture of TPOP as a phosphorus source and HDA as a stabilizer in ODE as the solvent. In a typical synthesis, 0.5 mmol of $In(ac)_3$, 0.5 mmol of $InCl_3$, 5 mmol of HDA, and 1.5 mL of TPOP were mixed with 15 ml of ODE. The mixture was heated up to 150 °C in 15 minutes under an argon atmosphere and kept at 150 °C for 60 minutes. Then, the mixture was heated to a higher temperature (230 °C-320 °C) within several minutes and kept at this temperature for 30 min.

The temperature dependence of the nanoparticle size and shape was investigated for a range of 230 °C-320 °C. In these experiments, all other variables remained constant. The transmission electron microscopy (TEM) images reveal the differently shaped nanomaterials resulting from varying temperatures (see Figure 3-2). The temperature affects the NCs' size and shape, ranging from nanowires to tetrahedrons and hyperbranched NCs. As powder X-ray diffraction (PXRD) revealed, all products displayed a cubic InP crystal phase in the space group $F_{-43m}$, with a = b = c = 0.587 nm (see Figure 3-2). The appreciable diffraction peaks at 2Θ = 26.34, 30.48, 43.58, and 51.78 are assigned to the (111), (200), (220), and (311) planes of InP (PDF#65-0233), respectively.

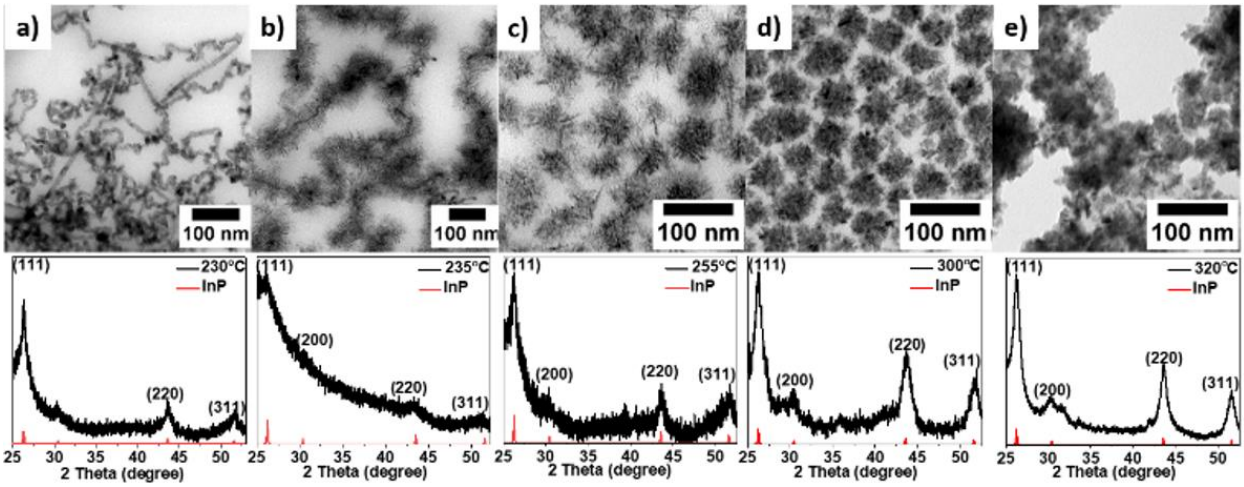


**Figure 3-2.** TEM images and PXRD patterns of indium phosphide NCs synthesized at different temperatures, ranging from 230 °C to 320 °C. At lower temperatures, InP wires are formed (a). Increasing the temperature leads first to branching on the wires (b), then to hyperbranched spherical InP nanoparticles (c). Increasing the temperature above 300 °C leads to a reduced length of the branches (d) and finally, NCs are sintered together into large aggregates (e).

Our experiments found that the molar ratio of the $InCl_3$: $In(ac)_3$ was a key factor that affects the formation of indium phosphide NCs. With only $InCl_3$ or $In(ac)_3$ as In precursor, the color of

the solution did not change even during prolonged heat treatment, and no product could be precipitated from the reaction solution (Figure 3-3). However, InP particles formed when we utilized mixtures of $In(ac)_3$ and $InCl_3$ as the precursors. More importantly, only a molar ratio of 1:1 of $In(ac)_3$: $InCl_3$ resulted in the formation of regular InP NCs.

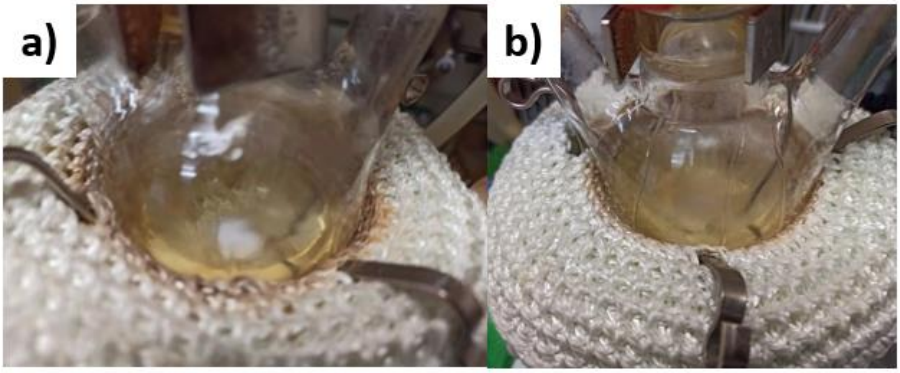


**Figure 3-3.** The reaction with only $InCl_3$ (a) or $In(Ac)_3$ (b).

As InP is synthesized by the one-pot heating-up method. Here we used the one-pot heating-up method to track the transient reaction process at different temperatures (230 °C, 240 °C, 250 °C, 260 °C, 280 °C, and 300 °C) to see the transient change of the morphologies and phases of products. For the experiment, we added $InCl_3$, $In(ac)_3$, HDA, TPOP, and ODE at the beginning. Then the obtained mixture was heated to 150 °C under argon flow in 15 min and maintained at this temperature for 60 min. Later, the mixture was heated to 300 °C in 15 min. We quickly took out the products at the target temperature during the second step. To confirm the morphologies and phase of the intermediate products, we measured their TEM and PXRD. As we can see from the result (Figures A3-1, 2), the InP forms at 230 °C, and later it aggregates from big particles. So the morphologies and phases of intermediate products could be determined by those results.

Furthermore, we investigated the impact of the hot injection of TPOP instead of heating the complete mixture in a one-pot reaction scheme. At room temperature, we added $InCl_3$, $In(ac)_3$, HDA, TPOP, and ODE to the flask. Since the color of the mixture had already become intensely dark at 270 °C. When the temperature reached 270 °C, we injected different amounts of TPOP into the reaction mixture. Figure 3-4 displays representative TEM micrographs and the PXRD patterns of the InP NCs produced following this procedure.

It is interesting to note that the NCs' size increased when decreasing the amount of TPOP. For example, when we injected 1 mL of TPOP into the solution, we were able to synthesize the biggest hyperbranched NCs with a diameter of around 160 nm (Figure 3-4e). Figures 3-4a, b, c,

and d show TEM images of InP NCs with sizes of around 20 nm, 70 nm, 80 nm, and 120 nm, which were synthesized at injection amounts of 3 mL (Figure A3-7), 2.5 mL (Figure A3-6), 2 mL (Figure A3-5), 1.5 mL (Figure A3-4), and 1 mL (Figure A3-3) of TPOP, respectively. PXRD patterns reveal that the NCs are all in the cubic InP phase, with an $F_{-43m}$ space group (Figure 3-4f).

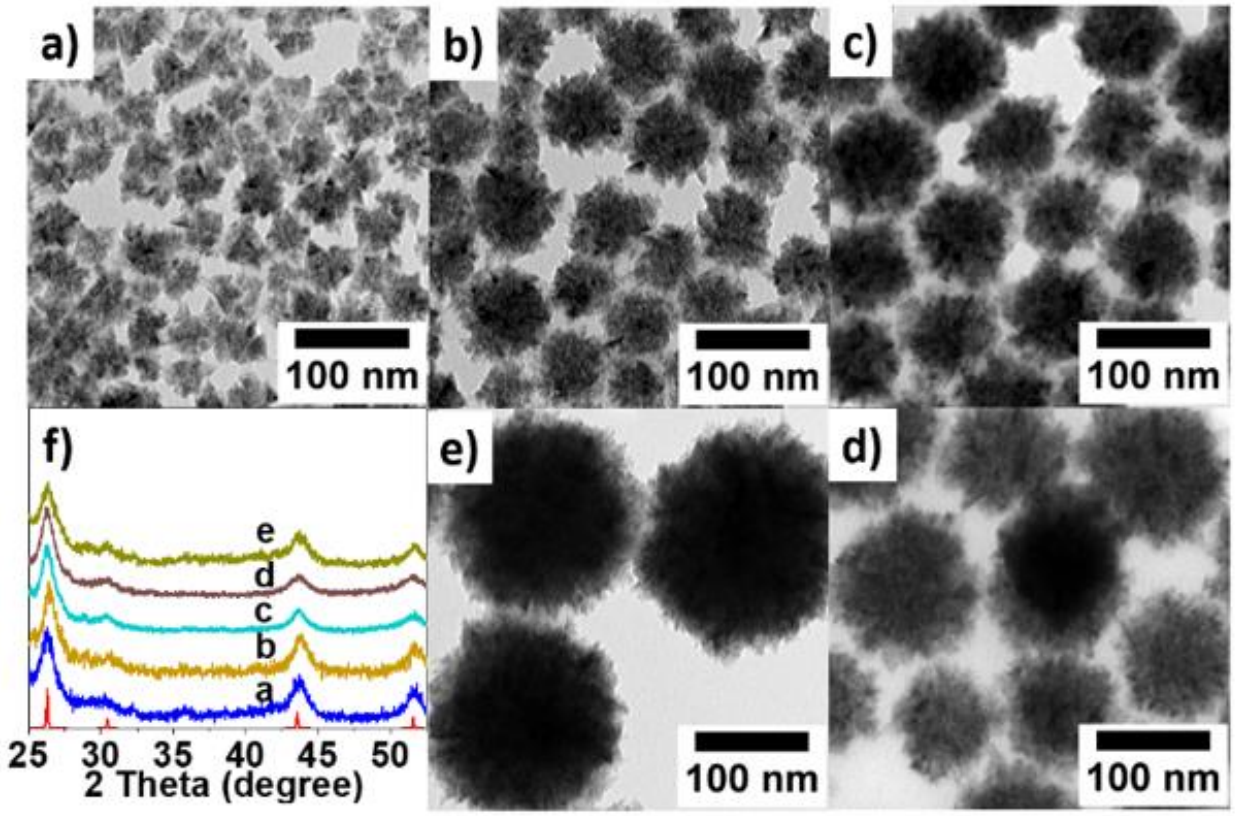


**Figure 3-4.** TEM images and PXRD of InP NCs synthesized at different temperatures. (a) 230 °C. (b) 240 °C. (c) 250 °C. (d) 260 °C. (e) 280 °C. (f) 300 °C.

Interestingly, smaller, tetrahedron-shaped InP nanoparticles could be produced by spiking the reaction mixture with acetic acid. We got the idea of adding acetic acid from the literature.[124] In this paper, acetic acid was used to tune the shape of PbS nanoparticles from quasi-spherical particles via octahedrons to six-armed stars. So when we did the reaction, we added different amounts of acetic acid to the reaction. We found that by spiking the reaction mixture with more acetic acid, indeed, smaller tetrahedron-shaped InP nanoparticles with sizes in the range of 10-20 nm can be obtained (Figure 3-5).

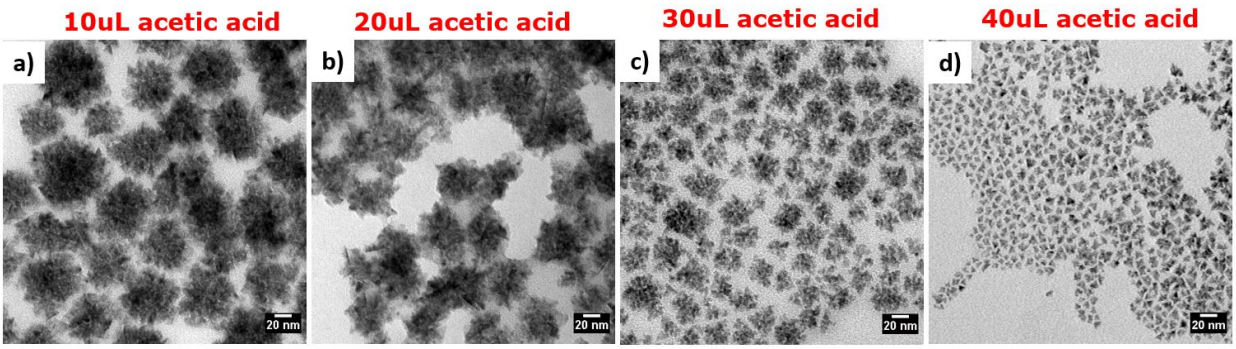


**Figure 3-5.** TEM of InP with different amounts of acetic acid added.

To shed some light on the InP nanomaterial formation, we monitored the formation of eventual intermediate products during a typical synthesis, as summarized in Figure 3-6. Firstly, we added $InCl_3$, $In(ac)_3$, HDA, and ODE to the reaction flask and heated the mixture to 150 °C for 60 min. Then we injected the TPOP at 270 °C. Aliquots were taken before and after TPOP addition and analyzed by TEM and PXRD. Interestingly, ~ 60 nm-sized InP hyper branch NCs (Figure 3-6b) formed from ~ 20 nm-sized $In_2O_3$ NCs (Fig. 3-6c).

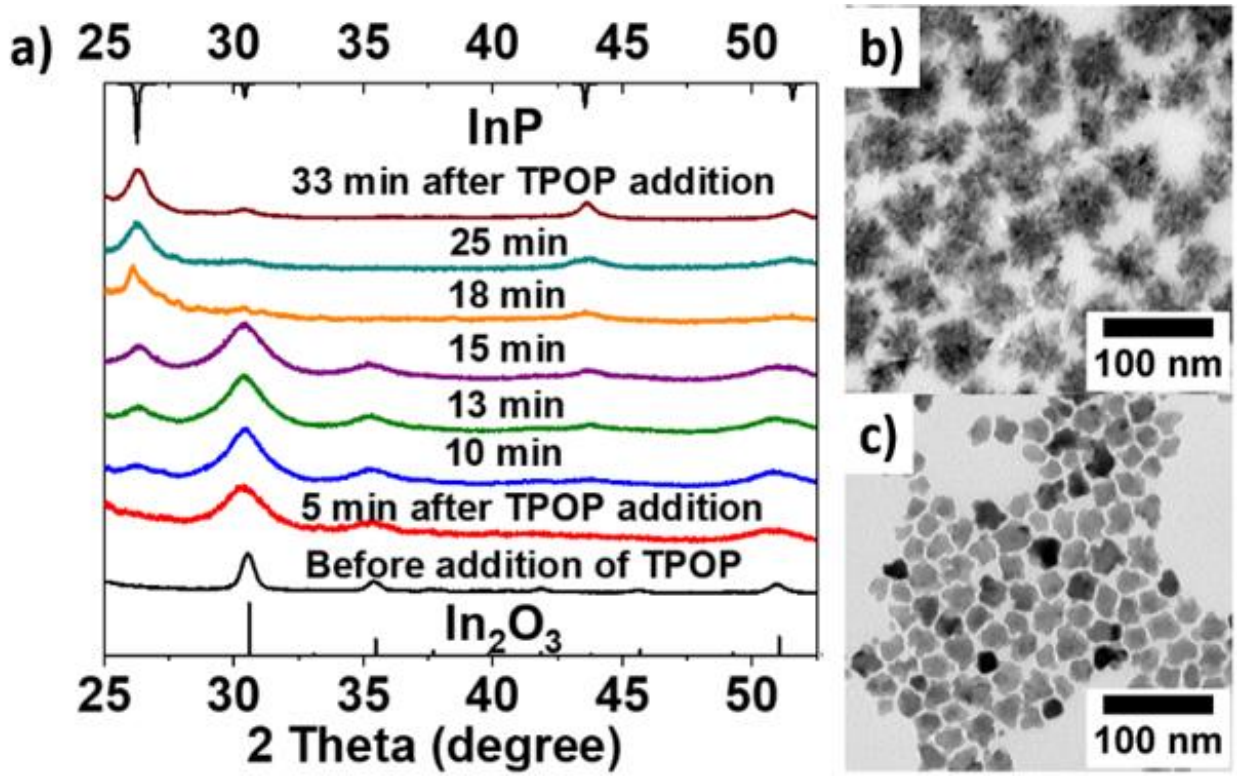


**Figure 3-6.** Illustration of $In_2O_3$ to form InP. (a) PXRD before and after the addition of TPOP. (b) TEM of InP NCs. (c) TEM of $In_2O_3$ NCs at 270 °C before the addition of TPOP.

During the heating process, we added $InCl_3$, $In(ac)_3$, HDA, and ODE at the beginning, and then the temperature was increased to 270 °C. During the process, we got the products at 150 °C (Figure 3-7a) and 270 °C (Figure 3-7b) before TPOP was added. So $In_2O_3$ is formed after 60 min at 150 °C, as the PXRD pattern was found to match the reference pattern of $In_2O_3$ (Figure 3-8). No additional peaks were observed, suggesting that few or no crystalline impurities were present. Then we injected the TPOP at 270 °C, and the PXRD patterns for samples collected after 5, 10, 13, 15, 18, 25, and 33 min. It showed the progressive transformation of the $In_2O_3$ NCs to InP NCs. The planes on these NPs (generally (111) or (220)) are readily available for P diffusion.[125] After 33 min, the complete transformation of the $In_2O_3$ NCs into hyperbranched InP NCs was confirmed by PXRD and TEM (Fig. 3-12).

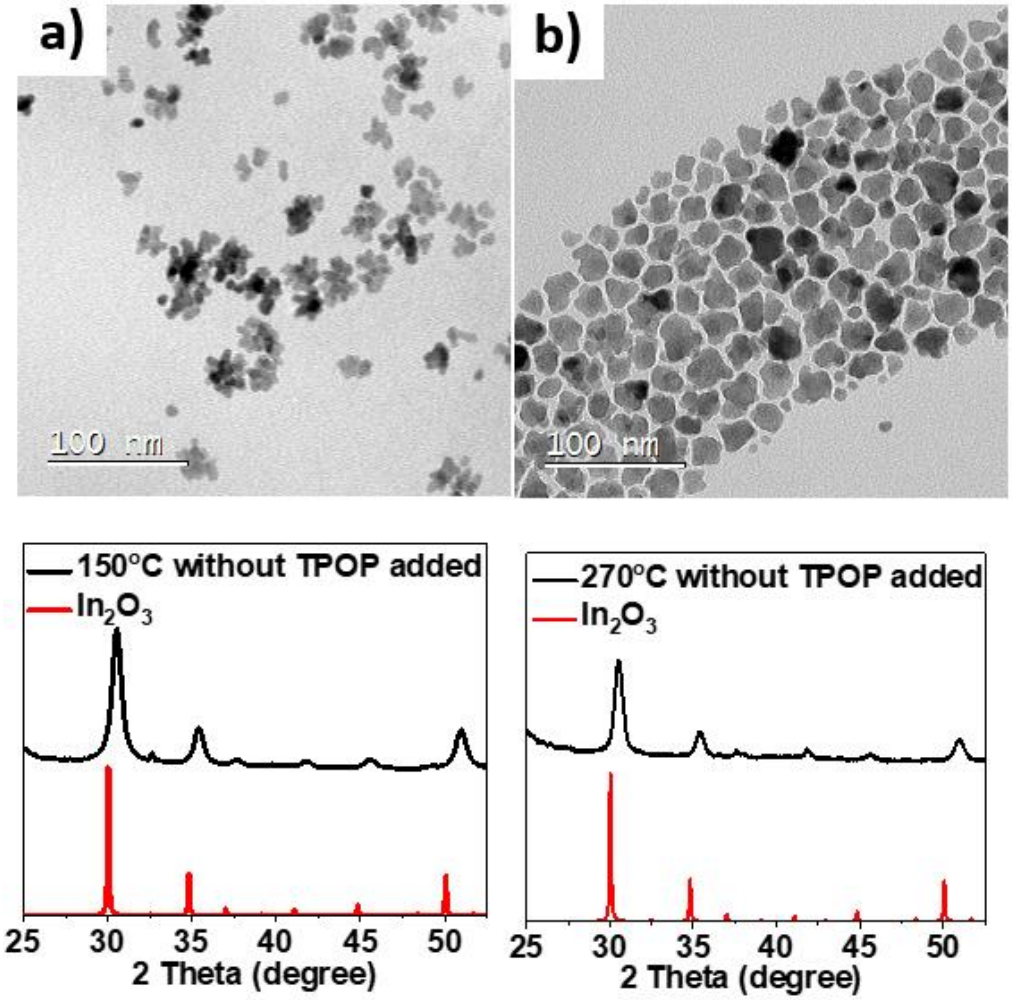


**Figure 3-7.** TEM images and PXRD of the intermediate states without TPOP were added. The intermediate states during the heating process need to be captured (150 °C-270 °C), without TPOP added. (a) 150 °C without TPOP added. (b) 270 °C without TPOP added.

Based on this interesting observation, commercial $In_2O_3$ was used to conduct the reaction under the same situation. For the experiment, we added chloride ions as acetate sources with commercial $In_2O_3$ at the beginning. Unfortunately, we could not yield InP NCs (Figure 3-8). This hints that the transformation from $In_2O_3$ to InP only works when the oxide NCs are produced from $In(ac)_3$ and $InCl_3$. We speculate that the halide on the oxide NCs' surface plays an important role in this reaction.

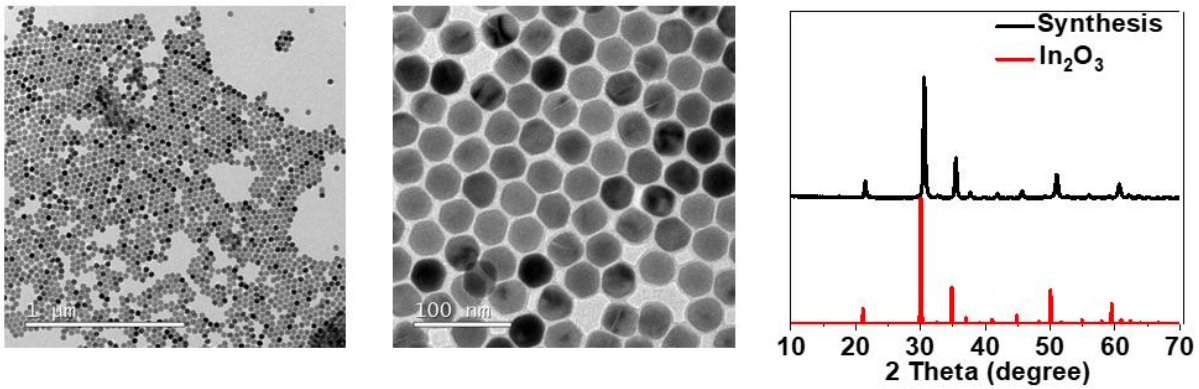


**Figure 3-8.** The co-decomposition experiments of chloride ion sources with commercial $In_2O_3$.

For reaction, $InBr_3$ and $InI_3$ have been examined to prove the important role of halide. From the results, we found that they also formed the InP, and the morphologies are similar. From the results, we found that they also formed the InP, and the morphologies were similar (Figure 3-9). For example, the halide ion influences the formation of nickel nanoparticles and their conversion into hollow nickel phosphide.[126]

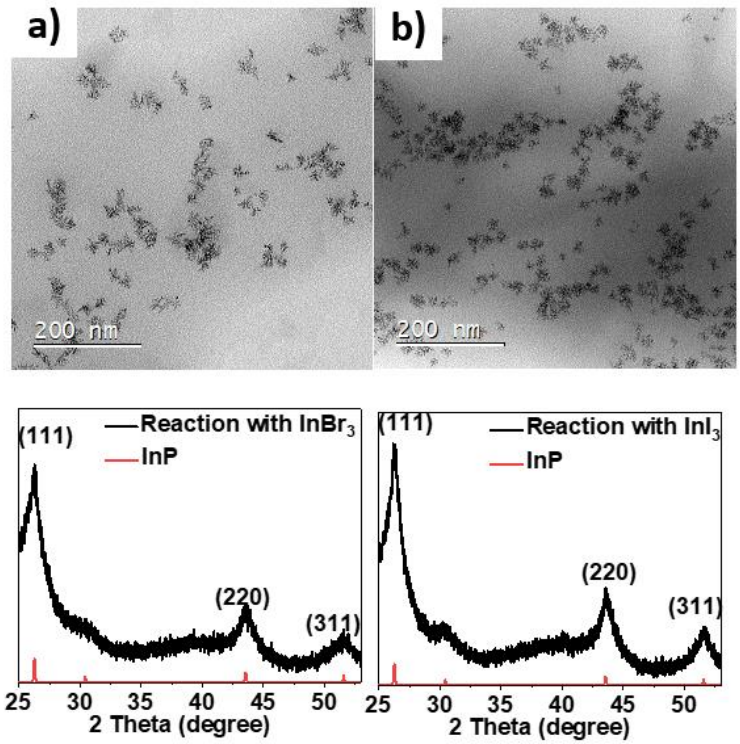


**Figure 3-9.** The reaction with $InBr_3$ (a) or $InI_3$ (b).

The transformation of metal oxides to metal phosphides is known for a variety of nanomaterials, yet not for InP. Brock et al.,[123] studied NiO nanoparticles that enable their transformation into $Ni_2P$ phosphides by solution-phase reaction with trioctyl phosphine (TOP) at temperatures of 385 °C. Sun et al.,[125] reported that bimetallic phosphides, Co-Fe-P could be obtained by the reaction between Co-Fe-O nanoparticles and TOP at high temperatures for 12 h. Surprisingly, we were able to yield InP NCs at lower temperatures in around 2 h.

In summary, our experiments revealed that the formation of InP proceeds via the chemical transformation of in situ-produced $In_2O_3$ NCs by a simple one-pot reaction.

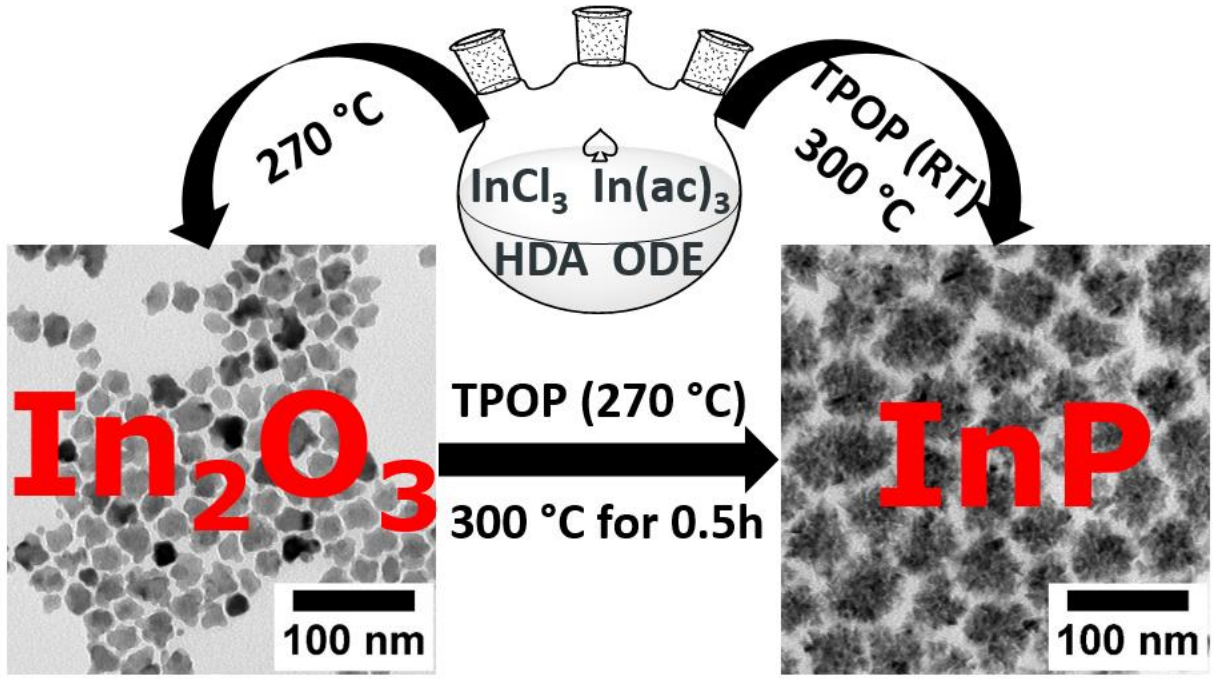


**Figure 3-10.** From $In_2O_3$ NCs to InP NCs.

### 3.4 Conclusion

We present a facile approach to nanostructured InP via a high-temperature (230-320 °C) reaction of indium chloride and indium acetate with TPOP. In the synthesis, the co-presence of acetate and chloride is necessary for the formation of InP NCs and facilitates the anisotropic growth of InP into either wires, tetrahedrons, or hyperbranched NCs. The size of the NCs is controlled by the amount of (hot injected) TPOP. Our experiments revealed that the formation of InP proceeds via the chemical transformation of in situ-produced $In_2O_3$ NCs. Our approach provides a new approach to indium phosphides with control of morphology and size. This new approach to anisotropic and hyperbranched InP nanomaterials is especially interesting for applications that require large surface areas, such as catalysis and energy storage applications.

# Chapter 4: Solvation Forces Affect the Colloidal Stability of CdSe Nanoplatelets

My contributions to this project were conceiving and designing the experiments, synthesis, characterization (UV-vis, TEM, THz spectroscopy), and data analysis of CdSe nanoplatelets. Nanning Petersen and Martin Girard helped with the molecular dynamics simulations. Heng Zhang, Wenhao Zheng, and Jaco J Geuchies discussed the data of THz spectroscopy.

## 4.1 Introduction

Colloidal semiconductor nanoparticles (NPs) have attracted significant scientific attention due to their size-dependent optical and electronic properties.[127,128,129,130,131] As discussed in Chapter 1.3.3, several forces, including van der Waals (vdW) attractions, electrostatic interactions (for polar solvents), and solvation forces, can contribute to free energy and the interaction between NPs and thus the colloidal stability: the ability/tendency of NPs to remain dispersed in solution without aggregation or sedimentation over time. Tuning one or more of the forces mentioned above allows for controlling colloidal stability. An increase (or reduction) in the attraction between NPs will lower (increase) colloidal stability, which lowers (or enhances) the critical concentration at which the NPs start to aggregate. A recently published molecular dynamics simulation study by Petersen et al. showed that solvation forces play a crucial role in dictating CdSe nanoplatelets (NPLs) interactions and, thus, colloidal stability in octane solvents.[54] They found that large facet areas, short surface ligand length, and high ligand grafting density lead to strong solvation forces between NPLs, enhancing attraction between them.[54] They put forward that the ligand-capped CdSe NPL is an ideal model for studying solvation forces between NPs. Several advantageous features of NPLs, including a large facet-to-NPLs size ratio and a dense ligand shell, favor strong solvent layering and, thus, strong solvation forces for NPLs.[133,134,135,136,137] The NPL-NPL van der Waals attraction, on the other hand, is found to be very weak,[54] negligible compared to the solvation forces. While the simulation work by Petersen et al. provided theoretical insights into the critical role of solvation forces in tuning the NPL stability, its direct experimental access remains largely unexplored, yet critical for testing the prediction. Generally, little attention has been paid to elucidating the role of solvents on the colloidal stability of NPLs.

In this study, we applied a combined experimental and simulation approach to study the aggregation process of CdSe NPLs in dispersion. Employing optical pump-THz probe (OPTP) spectroscopy, we experimentally show that both the facet area of NPLs and the solvent nature (solvent alkane length) play critical roles in governing the colloidal stability of NPLs. By increasing the NPL concentration, the aggregation of NPLs occurs to enhance the inter-NPL coupling and, thus, the conductivity of photogenerated charge carriers, which OPTP can readily capture. In line with the simulation by Petersen et al. (for both previously published work and extended simulation for this study), we show that increasing facet areas of NPL and the length of alkane solvent hamper the stability of NPL dispersion: larger CdSe NPLs with longer alkane solvent aggregate more easily than small ones with short alkane solvent. The combined experimental and simulation investigation pointed out the critical role of the NPL solvation forces in dictating the colloidal stability, which is relevant for the NPL processing for optoelectronic devices.

## 4.2. Result and discussion

### 4.2.1 Synthesis and characterization

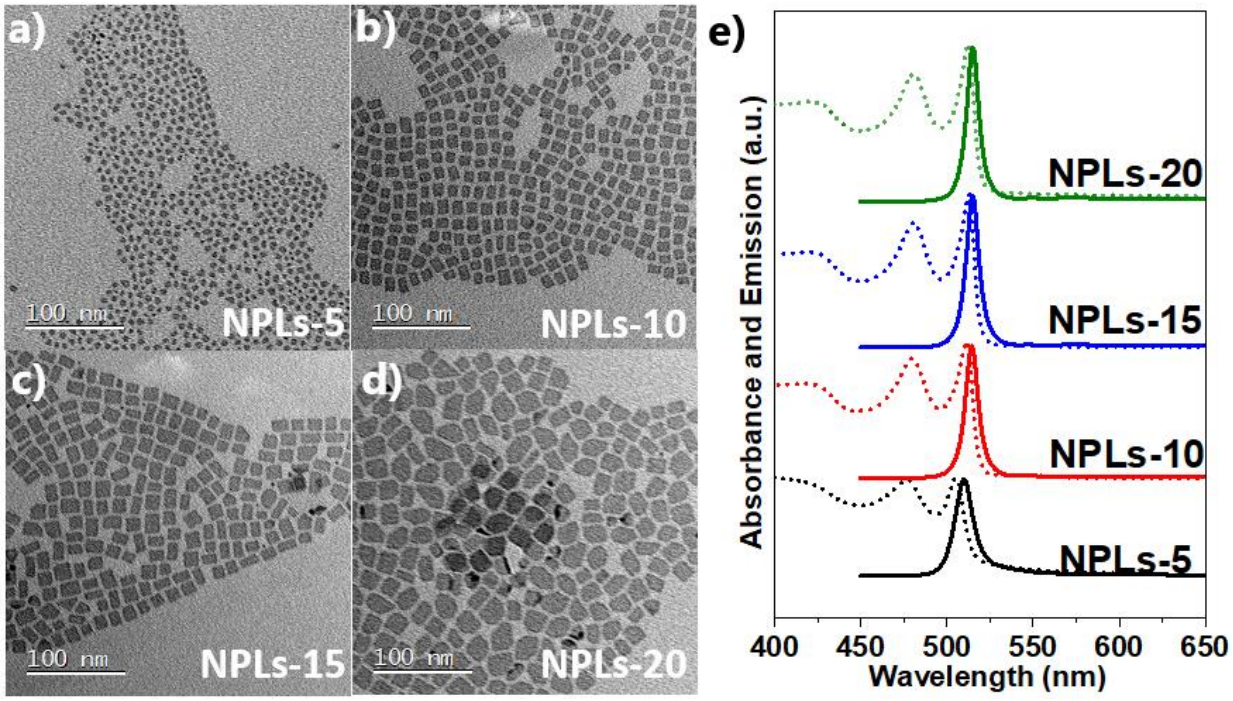


**Figure 4-1.** Characterizations of synthesized 4 ML CdSe NPLs with varied facet areas. (a-d) TEM image of the four NPLs with an average side-length of (a) ~5 nm, (b) ~10 nm, (c) 15 nm, and (d)

20 nm. The samples are marked as NPLs-L, with L as the side length of NPLs (in nm). (e) Absorption and PL spectra of CdSe NPLs dispersed in hexane.

We synthesized a series of zinc-blende 4 ML CdSe NPLs with a fixed thickness of 1.4 nm, capped with myristate ligands, following a previously reported procedure with minor modification (for details, see Chapter 2).[134] By adjusting the growth time, four nearly square-shaped 4 ML CdSe NPLs with tunable side lengths of ~5, ~10, ~15, and ~20 nm (corresponding to facet areas ranging from 24, 119, 215, and 420 $nm^2$) are synthesized. Typical morphologies of the samples are captured by transmission electron microscopy (TEM) studies shown in Figure 4-1 (a-d). For convenience, we term samples here as NPLs-L, with L as the averaged side lengths of the NPLs in nm (with L = 5, 10, 15, and 20, respectively).

We further measured the absorption and emission spectra of all samples, as presented in Figure 4-1e. For the 4 ML CdSe NPLs, sharp peaks around 480 and 512 nm involve the light and heavy hole transitions, respectively. As we can see, except for a minor ~7 nm shift from NPLs-5 to NPLs-10, no spectral shift in both absorption and photoluminescence (PL) spectra are observed with further increasing facet area. These results are in line with a previous report[138] stating that the electronic structure of the NPLs is predominantly controlled by the strong quantum confinement induced by the limited thickness, and lateral confinement plays a minor role in determining the optical absorption for the samples used here.

### 4.2.2 Lateral area matters: tracking size-dependent NPLs aggregation kinetics

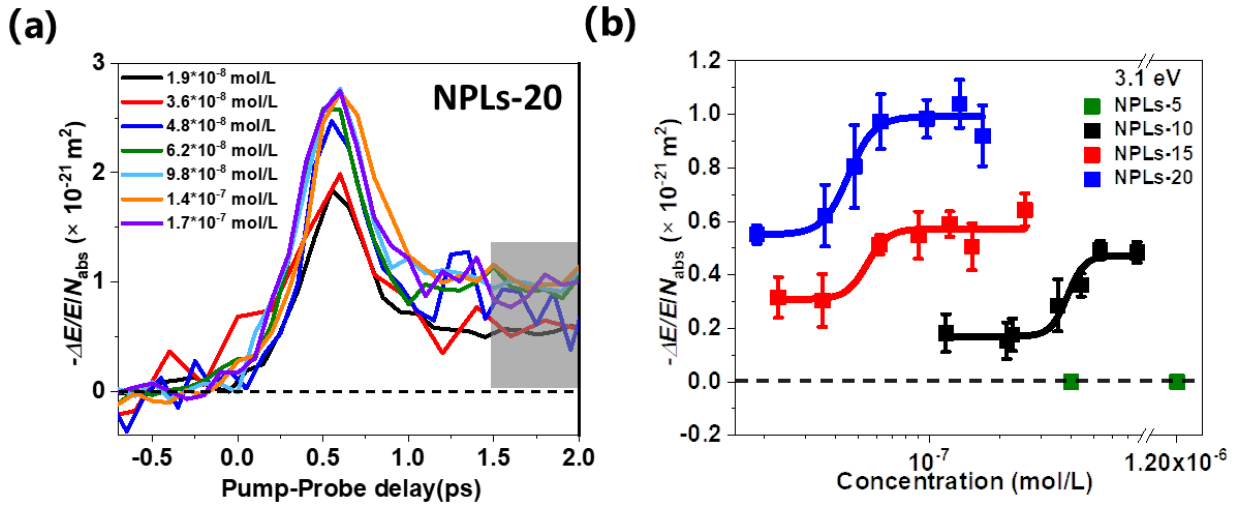


**Figure 4-2.** Investigation of charge carrier dynamics in CdSe NPLs dispersion by THz spectroscopy, divided by the absorbed photon density $N_{abs}$. (a) The concentration-dependent, time-

resolved THz conductivity following 3.1 eV excitation for NPLs-20. (b) Summary of the concentration-dependent photoconductivity averaged between 1.5 ps to 2 ps of the real part of the photoconductivity normalized to the absorbed photon density following 3.1 eV excitation for NPLs-5, 10, 15, and 20.

To shed light on the concentration-dependent aggregation of CdSe NPLs, optical pump-THz probe (OPTP) spectroscopy is employed to study the electrical properties of NPLs in dispersion by measuring their photoconductivities ($\Delta\sigma$). The schematic OPTP study is illustrated in Figure 2-7 in Chapter 2. In short, we optically promote electrons from the valence band to the conduction band in the NPLs by utilizing an ultrafast (~100 fs, 400 nm) laser pulse. The pump-induced change in the conductivity, i.e., photoconductivity $\Delta\sigma$, is probed by a THz pulse with a duration of ~1 ps. Note that $\Delta\sigma$ is a complex quantity, containing real (R) and imaginary (I) parts: $\Delta\sigma=\Delta\sigma_R + i\Delta\sigma_I$. Free charge carriers and bound charge states, e.g., excitons, possess distinctly different dispersion in the THz frequency window (up to 2.5 THz here). The THz field ($E$) accelerates free carriers, attenuating the THz field. The photo-induced THz attenuation ($\Delta E$) is linearly proportional to the real part of photoconductivity $\Delta\sigma_R$. On the other hand, excitons, as charge-neutral species, mainly induce a phase shift in THz probe pulses. This phase shift is related to the polarizability of excitons and proportional to the imaginary part of the photoconductivity $\Delta\sigma_I$.

In our 4 ML CdSe NPLs, pulsed excitation creates (exciton-dominated) charge species. When the NPLs form dimers or stacks, the electronic coupling between the NPLs increases. Free carrier generation can result from enhanced inter-NPL charge separation, and potentially also the mobility of the free charge carriers is expected to increase with increasing NPL aggregation. As such, one would expect an increase in the photoconductivity $\Delta\sigma_R$ with increasing inter-NPL coupling. This transition in the photoconductivity in the aggregation process can be measured by the OPTP experiments,[58] which can report on the aggregation of NPLs. In our study, we exploited this effect to distinguish single NPLs and assembled NPLs to evaluate the critical concentration at which aggregation of NPLs begins. For NPLs-5 dispersed in hexane, the THz response is purely excitonic, as evident from the zero real and purely imaginary THz photoconductivity. This observation holds, even at extremely high concentrations (Figure A4-1). The effect can be rationalized by a combination of strong exciton effect in NPLs-5 (so that the majority, if not 100%, of charge carriers are in exciton states), and moderate mobility of free carriers (if any) due to the imposed structural

strong confinement as the lateral size of NPL is smaller than the Bohr radius of CdSe semiconductors.

We then further studied NPLs with large lateral sizes. The UV-vis absorption spectra of NPLs-20 with different concentrations are shown in Figure A4-2c. As the absorbance of the heavy hole transition increases by a factor of ~ 10 (from 0.11 to 1.02), the corresponding NPLs concentration increases linearly from $1.9 \times 10^{-8}$ to $1.7 \times 10^{-7}$ mol/L. Importantly, no significant peak shift in absorption is observed upon a change in the concentration. Following optical excitations, THz photoconductivity in the NPLs-20 dispersion evolves with the concentrations as shown in Figure 4-2a and Figure A4-2f. The dynamics are dominated by the imaginary $\Delta\sigma$, which indicates that a significant portion of charge carriers are in the exciton state even for NPLs-20. On the other hand, we observe a finite contribution in the real part of the photoconductivity for all concentrations studied. We assign this signal to free charge carrier generation and their finite conductivity thanks to the reduced confinement effects in NPL aggregates.[58] Similar effects have been observed in NPLs-10 and 15 (see details in Figure A4-2). To make a fair photoconductivity comparison for all 4 NPL sizes with different concentrations, we normalize all the $\Delta\sigma$ data to the absorbed photon density ($N_{abs}$). We summarize the size- and concentration-dependent real photoconductivity (average 1.5 ps to 2 ps) in the NPLs dispersion under the excitation photon energy of 3.1 eV for all the samples in Figure 4-2b. As we can see, for sufficiently large NPLs (NPLs-10, 15, and 20), the photoconductivity undergoes a sigmoidal-type transition by increasing the concentration. Here, we assign the concentration-independent conductivity in the diluted limit to the intrinsic intra-NPL free carrier generation and transport (whose amplitude intuitively increases with the lateral size). Aggregation in the high concentration limit, is expected to further enhance the free carrier population and mobility, resulting in the photoconductivity transition observed in Figure 4-2b. Our assignment of the NPL aggregation-induced sigmoidal photoconductivity transition is further supported by two observations: (1) the critical concentration for aggregation is reduced with the NPLs facet area: i.e. the larger the NPLs, the easier they aggregate. This result is fully in line with recent simulation results by Petersen in which the solvation force was claimed to increase with the facet area: the larger the NPLs, the easier they turn to aggregate. This effect leads to the transition in the photoconductivity appearing at lower concentrations for bigger facet areas. (2) we investigate complementarily concentration-dependent PL emission quantum yield. In principle, in the diluted limit, the PL efficiency normalized to the

concentration ($\eta_{PL}$/c) is expected to show no dependence on the concertation (or, in other words, the PL efficiency increases linearly with concentration). With further concentration increase, $\eta_{PL}$/c goes down. This can be rationalized as follows: the aggregation favors inter-NPL charge transport (CT) or energy transfer (ET, e.g., via the Förster-mechanism). The enhanced CT or ET reduces PL quantum yields, as they result in charge separation, increasing their non-radiative recombination via defects (as charges can map out much larger space to encounter defects).[140,141] Our experimental result, as shown in Figure A4-3, aligns nicely with the expectation and previous reports. More importantly, the critical concentration at which $\eta_{PL}$/c starts to decrease is close to the aggregation *c* quantified by OPTP measurement.

### 4.2.3 The solvent nature matters: tracking solvent length-dependent NPLs aggregation

In the next step, we studied the effect of different solvents on NPLs aggregation. We studied four alkanes with different lengths (hexane, octane, decane, and dodecane). As shown in Figure A4-4, concentration-dependent photoconductivity is measured with different solvents following 400 nm excitations. We summarize the peak value of photoconductivity in Figure 4-3. As we can see, the critical aggregation concentration drops with increasing solvent alkane length. This result indicates that the attraction between the NPLs increases with the solvent alkane length.

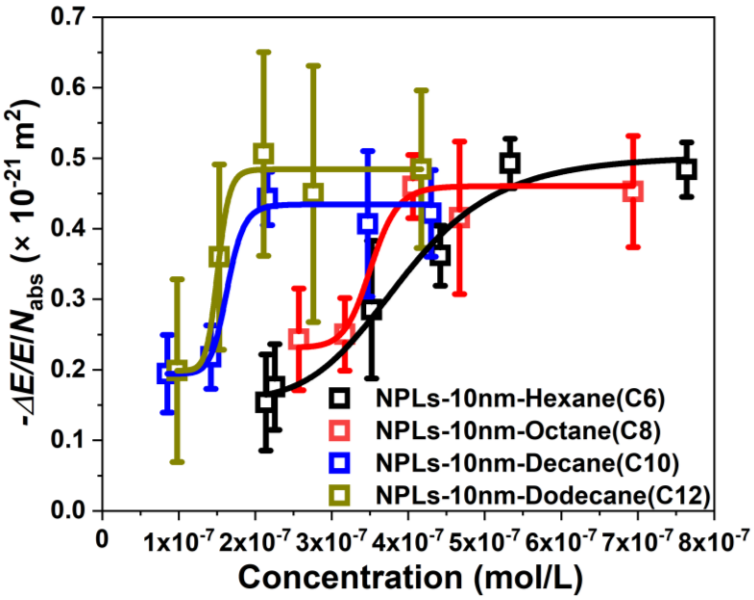


**Figure 4-3.** Summary of the concentration-dependent photoconductivity average 1.5 ps to 2 ps of the real part of the one-dimensional conductivity normalized to the absorbed photon density following 3.1 eV excitation for NPLs in hexane, octane, decane, and dodecane.

To shed light on the role of solvent length in dictating solvation force and, thus, NPL aggregation processes, our colleagues Nanning Petersen, Valsson Omar, and Martin Girard at MPIP further extended their coarse-grained molecular dynamic simulations to study the effect of the alkane length on the NPL interaction, particularly for our solvents. The simulation procedure follows that described in their early publication,[54] and the model is briefly shown in Figure 4-4a. NPLs, modeled by surface beads, have a thickness of 1.5 nm and a base facet area of 35.6 $nm^2$. The surface beads serve as grafting points for the ligand molecules. We use the MARTINI force field to describe the interactions of the ligand and solvent molecules. Within the MARTINI model, one bead represents four $CH_x$ atom groups. This type of description has the advantage of reducing the number of particles in the simulation compared to an all-atom approach, thus considerably reducing the computational effort.

The myristic acid ligands have 14 C atoms (including the functional group). Therefore, within the MARTINI model, myristic acid can be modeled by three or four ligand beads. Petersen et al. have shown that the ligand length influences the strength of the pair interaction.[54] With increasing ligand length, the attraction between the NPLs is reduced. To get a lower bound of the attraction, the myristic acid ligands were simulated by four ligand beads. The solvent molecules are described by one to four beads, screening hexane to hexadecane.

Following Petersen's paper,[54] by using molecular dynamic simulations, we study the free energy in the face-to-face orientation of the NPLs (Figure 4-4).[142] The zero point of free energy was placed in the first minimum. Although the strength of the interaction increases with the alkane length, all four curves are qualitatively similar in their shape. The computational effort increases with increasing alkane length due to the increasing viscosity and the increasing number of beads in the simulation. Therefore, only the beginning of the free energy curves with 3 and 4 solvent beads were fully converged (Figure 4-4b). Here the free energy difference between the first minimum and the bulk (10 nm distance) defines the attraction, in other words, defines the solvation forces. Even though the exact bulk free energy values for three and four beads have not been calculated, it can be concluded that the solvation forces between the NPLs increase strongly with the alkane length. These simulation results further confirm the conclusion of Petersen et al.[54] that solvation forces crucially influence the CdSe NPLs interaction, and dominate it.

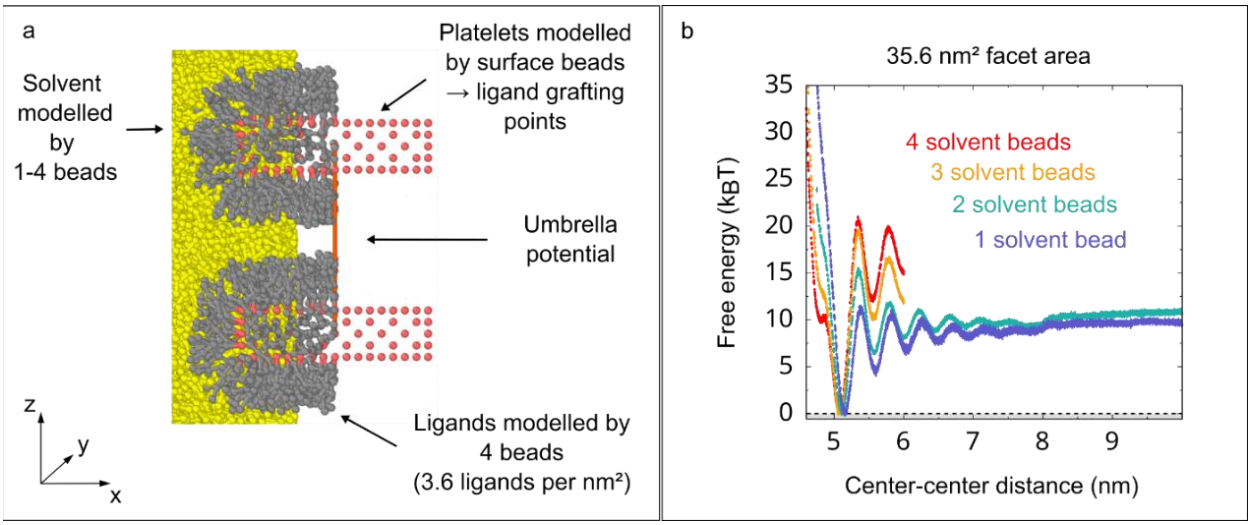


**Figure 4-4.** Molecular dynamic simulations by the MARTINI force field. (a) The model system setup. Surface beads are shown in red, ligand beads in gray, and solvent beads in yellow. We calculate the free energy curves in the face-to-face orientation of the NPLs. (b) We compare the effect of different solvent molecule lengths on the free energy curve and the NPL pair interaction.

### 4.3. Conclusion

In this chapter, OPTP was used to study the aggregation of 4 ML CdSe NPLs in the dispersion. We demonstrate experimentally that both the facet area of NPLs and the solvent nature (e.g. the alkane length) matter for the NPLs' colloidal stability. We observed that increasing NPLs' facet area and solvent length leads to a decrease in the critical concentration at which aggregation starts. The former effect is perfectly in line with the recent simulation results by Petersen in which the solvation forces were found to increase with the facet area NPLs, causing aggregation. Furthermore, our simulation result shows that the solvation force increases with the alkane length, leading to a strong NPLs aggregation effect in solvents with a long alkane length. Our studies not only unveil the critical physiochemical factors governing the NPLs dispersion stability but also establish THz spectroscopy as a sensitive probe to the microscopic aggregation of nanoscale materials. Our method will be particularly powerful for studying the colloidal stability of semiconducting nanomaterials with weak or PL emission.

# Chapter 5: Ligand Decomposition Governs the Inter-Nanoplatelet Distance and Coupling Strength by Thermal Annealing

My contributions to this project were conceiving and designing the experiments, synthesis, characterization (UV-vis spectroscopy, TEM, THz spectroscopy), and data analysis of CdSe nanoplatelets. Raman spectroscopy was done by Samir H. Al-Hilfi. Guangbo Chen and Xinliang Feng helped with the TGA-MS analysis. Heng Zhang, Wenhao Zheng, Lucia Di. Virgilio, Jaco J Geuchies, and Junren Wang discussed the data of TEM and THz spectroscopy.

## 5.1 Introduction

Colloidal nanocrystals (NCs) are solution-processable building blocks for cost-efficient electrical and optoelectronic devices,[143,144,145] including field effect transistors, light-emitting diodes, photovoltaic devices, and photodetectors.[146,147,148,149] Among different NCs (zero-dimensional quantum dots (QDs),[150] one-dimensional nanorods, etc.),[151] CdSe nanoplatelets (NPLs) are promising two-dimensional (2D) semiconductors with lateral extension up to over 100 $nm^2$ and an atomically precise thickness.[58,152,153] The confinement in the thickness direction, which is tunable by controlling the NPLs' layer numbers, has been shown to dominate the electronic and optical properties of CdSe NPLs.[155,156] Due to 2D quantum confinement and reduced dielectric screening, photogenerated electrons and holes in NPLs are subject to enhanced Coulomb interactions. This leads to the formation of strongly bound electron-hole pairs, so-called excitons in NPLs. So far, an extremely high exciton binding energy, i.e., the ionization energy needed to dissociate excitons into free carriers, on the order of over 100s of meV has been reported in CdSe NPLs (e.g. ~ 170 meV for 4 monolayers (ML) NPLs).[157,158] The strong exciton effect results in excellent optical properties including giant oscillator strength,[159,160] and strong fluorescence quantum yields[161] (up to unity, which is highly desirable for light emission applications).

In conjunction with the thickness-tunable excellent optical properties, the 2D geometry makes NPLs ideal materials to potentially conduct charge carriers for light-to-electrical energy conversion applications, including solar cells and light detectors. In this regard, understanding the exciton dissociation and free carrier generation mechanism in NPLs solids is fundamentally important for high-performance electronic and optoelectronic devices.

The key to achieving efficient free carrier generation and enhanced charge transport properties (e.g., high carrier mobility) lies in "connecting" the NCs to allow sufficiently strong inter-NC electronic coupling. The coupling strength between NCs has been well-known and shown to increase exponentially with decreasing NC-NC distance.[162,163,164,165,166,167,168] In the QD community, so far, two methods have been demonstrated to effectively modulate the distance between NCs and thus their coupling strength: ligand exchange and thermal annealing. First, replacing the lengthy native ligands (e.g., cadmium myristate) with shorter ones (including both organic and inorganic) has been widely investigated.[163,164,165,169] For instance, Talapin et al. employed short inorganic ligands ($S^{2-}$, $SnS_6^{4-}$, $Te^{2-}$, $Se^{2-}$, or $HSe^-$) to cap QDs and achieved band-like transport in their solids with high electron mobility and photoconductivity.[170,171] Second, the key idea behind the thermal annealing strategy lies in removing surface ligands to gradually "fuse" QDs, which leads to an enhanced photoresponse. For instance, octylamine-capped PbS NCs annealed at 220 °C were reported to show a 200-fold increase in the short circuit current.[172] $CsPbX_3$ NCs were shown to possess significantly increased photocurrent after annealing.[173,174] CdSe NCs exhibited excellent electrochemical photocurrent, even after a mild heating treatment at 200 °C.[175]

In comparison to the QD field, there are fewer experimental efforts toward fabricating strongly coupled NPL solids and understanding their charge transport properties. In this direction, some preliminary work has been done by employing ligand exchange in 2D NPLs. For instance, Nadja et al. synthesized polymer-encapsulated NPL stacks and then manipulated the NPL-NPL distance. Reducing the inter-NPL distance, as expected, increases the photocurrent in devices.[176] While effort is still needed to understand the ligand exchange in 2D NPLs, even less research effort has been made to understand one of the most intuitive ways for linking NPLs: thermal annealing. This method should allow modulating inter-NC distance, and thereby optical properties and charge transport, in a very straightforward manner.

In this work, we combine optical absorption, transmission electron microscopy (TEM), and thermogravimetric analysis with mass spectroscopy (TGA-MS), and provide experimental evidence that the thermal stability of the surface ligands (e.g., their thermal decomposition) governs the inter-NPL distance and thus electronic coupling strength. Employing ultrafast terahertz (THz) spectroscopy, we show that the enhanced electronic coupling increases the free carrier generation efficiency as well as the short-range mobility in NPL solids. Our study provides

a new insight for employing thermal treatments as an intuitive and effective method to tune the optical and electrical properties of NPL solids.

## 5.2 Results and discussion

### 5.2.1 Synthesis and characterization

In the study, we used 4 ML CdSe NPLs with zinc-blende structure, which were prepared following the method reported by Ithurria.[177] As illustrated in Figure 5-1a, the NPLs consisted of 4.5 CdSe monolayers. The TEM images revealed rectangular-shaped 4 ML CdSe NPLs with lateral sizes of 12.0 ± 3.4 nm by 15.7 ± 2.6 nm (Figure 5-1b). The absorption spectra possess two pronounced excitonic peaks at 512 and 480 nm as shown in Figure 5-1c, which can be assigned to the heavy hole (HH) and the light hole (LH) transitions respectively.[178,155] The photoluminescence (PL) emission peak at 513 nm has a full width at half-maximum (FWHM) below 9 nm (equivalently, 32.5 meV) (Figure 5-1c). Both absorption and PL data are consistent with results previously reported for 4 ML CdSe NPLs.[58]

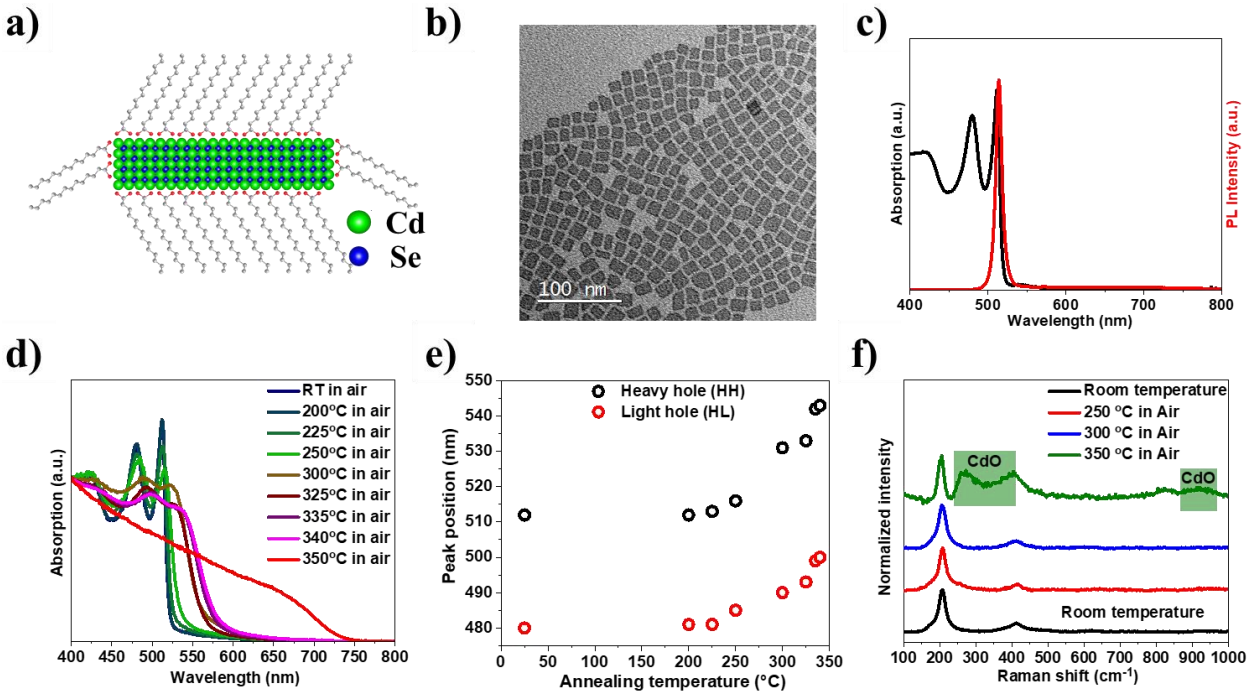


**Figure 5-1.** Characterizations of 4 ML CdSe NPLs. (a) Atomic structure illustration of 4 ML CdSe NPLs, which contain 5 ML of Cd atoms and 4 ML Se in the structure. The chelating carboxylate ligand is bound to the surface Cd atom to make the system charge neutral. (b) The TEM image of

face-down 4 ML CdSe NPLs. (c) Absorption (black) and PL emission (red) spectra of 4 ML CdSe NPLs. (d) Temperature-dependent absorption spectra and (e) the inferred absorption peaks of 4 ML CdSe NPLs in air. (f) Raman spectra of the 4 ML CdSe NPLs film with native ligands (black), annealing at 250 °C (red), 300 °C (blue), and 350 °C (olive) in the air.

To understand the effect of different annealing treatments on the ligand thermal stability and tuning the inter-NPL distance (and thus the electronic coupling strength), we combine optical absorption, TEM, TGA, and THz spectroscopy to characterize 4 ML CdSe NPLs in thin-films using different annealing temperatures (T). The samples are prepared by drop-casting 20 μL solutions of as-synthesized 4 ML CdSe NPLs ($1.07 \times 10^{-6}$ M, estimated from the absorption spectrum) on fused silica substrates (1 cm × 1 cm). The as-prepared NPLs film was annealed in a tube furnace heated to a target T between 200-350 °C for 30 min in the air (for more details, see the supporting information). Samples are then cooled down to room temperature in 120 min for further characterization.

### 5.2.2 UV-vis analysis

As shown in Figure 5-1d, increasing the annealing T leads to a gradual change in the optical absorption including a significant redshift of the lowest exciton (i.e., the HH transition) transition, when going beyond ~ 250 °C. Annealing treatments are expected to reduce the distance between the NPLs by presumably removing the capping ligands (see the discussion on the detailed mechanism later).[175,179,180,181,182] This results in enhanced inter-NPL coupling strength and thus loosened quantum and dielectric confinement in NPLs, which explains the absorption changes. Above 340 °C, a gentle increase of annealing T (e.g., from 340 to 350 °C) triggers a sudden transition from a sharp excitonic-like transition to a broader absorption feature with an absorption onset shift from 543 nm to ~700 nm. The inferred bandgap energy (see the Tauc plot in Figure A5-1) is 1.70 eV for the sample which was annealed at 350 °C, and is close to the bandgap of the bulk CdSe (1.74 eV or ~ 710 nm).[183,184] This result indicates that NPLs are fused into bulk-like aggregates (see TEM images below and in Figure A5-2) above an annealing T of 340 °C.

### 5.2.3 Raman spectroscopy analysis

To further shed light on the thermal annealing procedure, we performed Raman spectroscopy on NPLs film under different annealing T (Figure 5-1f). Two characteristic Raman modes at ~ 208

and 410 $cm^{-1}$ can be well assigned to the longitudinal optical (LO) and 2 LO phonon modes of 4 ML CdSe NPLs, which is consistent with literature reports.[185] By annealing the NPL film at 350 °C, we observe three newly emerged peaks at 290, 392, and 938 $cm^{-1}$ (marked in green) which can be attributed to CdO.[186] Together with the absorption data, we can conclude that along with the formation of bulk CdSe, oxide formation takes place simultaneously by annealing at 350 °C. Formation of CdO likely takes place at the surface of the CdSe aggregates following (at least completely) ligand removal.

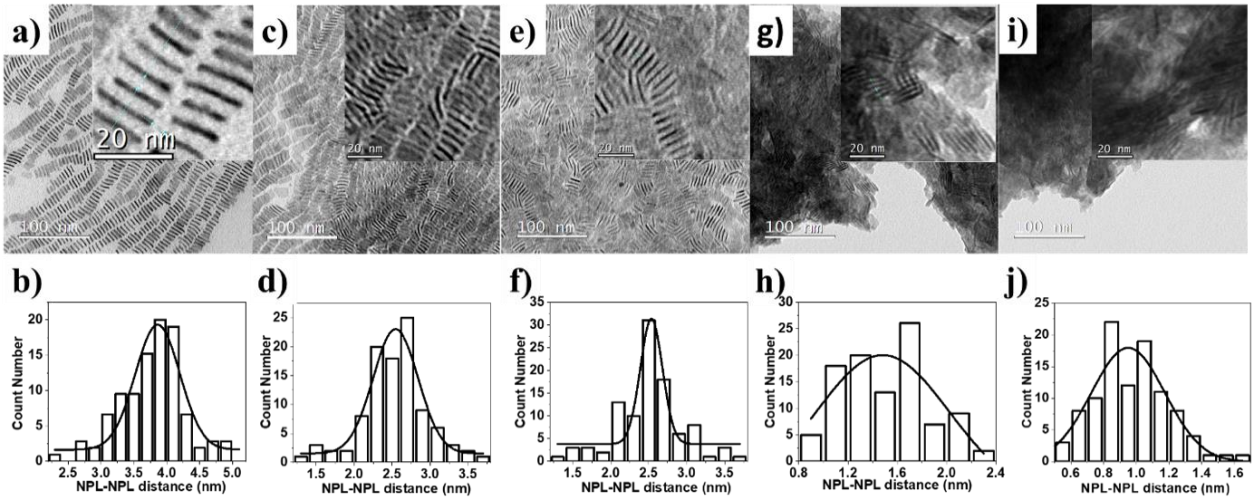


**Figure 5-2.** TEM images of 4 ML CdSe NPLs as-synthesized (a), after annealing at 80 °C (c), 250 °C (e), 300 °C (g), and 340 °C (i). The NPL-NPL distances are 3.8± 0.5 nm (a), 2.5 ± 0.4 nm (c), 2.5 ± 0.5 nm (e), 1.5 ± 0.4nm (g), and 1.0 ± 0.2 nm (i), respectively. Histograms of the NPL-NPL distance of 4 ML NPLs as-synthesized (b), after annealing at 80 °C (d), 250 °C (f), 300 °C (h), and 340 °C (j). ~ 100 NPL-NPL distances were analyzed.

### 5.2.4 TEM analysis

We performed TEM on NPLs films to obtain direct information on the morphology change (e.g., the inter-NPL distance change) after the thermal treatment. The as-prepared 4 ML CdSe NPLs films assemble in an edge-up geometry with a 3.8 ± 0.5 nm face-to-face stacking distance, as shown in Figures 5-2a, b. This inter-NPL distance is slightly higher than twice the Cd-myristate ligand length (nominally ~1.7 nm).[187] By further increasing the annealing T, as shown in Figure 5-2c (for 250 °C) and Figure 5-2e (for 300 °C), the edge-up configuration is maintained. The inter-NPL distance gradually drops with increasing T. More precisely, we observe that the first decrease in inter-NPL distance occurs at already at a low T, at around 80 °C (from 3.8 nm to ~ 2.5 nm),

which is slightly above the evaporation point of the solvent used to disperse the NPLs (hexane, 69 °C). This effect may be related to the evaporation of solvent molecules trapped in the voids of the NPL film, in line with previous reports.[181] By further increasing T, the distance remains nearly unchanged until 250 °C, after which it decreases further to below 1 nm at 340 °C. Finally, the film annealing at 350 °C results in the formation of clusters or the "necking" of NPL leading to a fused solid (Figure A5-2). In this narrow T range, combining the absorption result (i.e. the sudden changes from weak "excitonic" to bulk-like absorption), Raman data (i.e. the emergence of oxidation signal) and TEM analysis, we conclude that ligands are gradually removed from the NPL surface between 250-340 °C, and undergo a remarkably sudden removal of residual ligands between 340 - 350 °C.

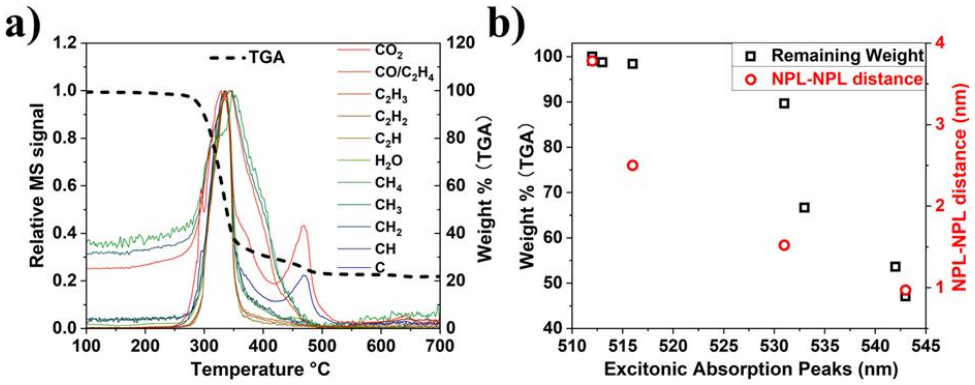


**Figure 5-3.** (a) Thermogravimetric Analysis with Mass-Spectrometry curve for the decomposition of Cd(myr)2. (b) Correlation between the TGA weight loss and the NPL-NPL distance versus the excitonic absorption peak for treatments until 340 °C.

### 5.2.5 Thermogravimetric analysis with mass-spectrometry (TGA-MS) analysis

To better understand the desorption of the potent myristic acid-related capping ligands, we conducted TGA-MS to study the decomposition of $Cd(myr)_2$. In an ideal situation, we would have conducted the study for $Cd(myr)_2$ capped 4 ML CdSe NPLs, but we have insufficient CdSe NPLs to do so. Such a simplified study can still provide molecular insights into the effects of thermal treatment. Figure 5-3a presents the normalized T-dependent gas release kinetics. First, the TGA curve shows two important weight loss steps, with the first step at a temperature range of ~250 - 350 °C with 62 wt. % loss (the T range that is relevant to our studies). In this region, the recorded gases detected by MS include various oxygen-containing molecules of organic molecules (i.e., CO, $CO_2$, and $H_2O$), and carbon-rich fragments (such as $CH_3$, $CH_2$, $C_2H_3$, and $C_2H_2$). Increasing the

temperature from 355 °C to 475 °C results in a second weight loss step with 11% more weight loss (Table A5-1). The released gases in the second step are only C and $CO_2$. We believe the first decomposition reactions happen during the first step, as most ligands were lost from the NPL solid and turned to gases. Furthermore, based on the MS signals, all the C-H containing parts of the ligands were released in the first step as well, while only C and C-O species were detected in the second step. Finally, given the rich gases (for both oxidized and C-based ones) releases and their similar kinetics, we exclude a scenario in which all the ligands decompose simultaneously in a step-by-step fashion, by losing $-CH_3$, or $-CH_2-$ groups (by simple decomposition or oxidation) one by one.

When we thermally anneal the ligand-capped NPL film in the air, we propose that $O_2$ oxidizes the Cd-myristate ligands to liberate gases. As a result, the ligand density decreases at high temperatures, thus gradually decreasing the inter-NPL distance. This proposal is consistent with previous reports. David et al. reported the decomposition and fragmentation products of CdSe QDs with the tertbutylthiol ligand.[175] Isobutene and isobutane were observed as the major volatile products during TGA measurements, and CxHy was removed first. This provides fine control on inter-NPL distance. In addition, SEM-EDX analysis shows a similar Cd/Se ratio for annealed NPLs, and a reduced amount of C content with increased annealing T, further supporting the conclusion of selectively removing ligands during the thermal annealing process (Table 5-1). In Figure 5-3b, we demonstrate that the weight loss by heat treatment can correlate perfectly with the NPL-NPL distance (by TEM) and shifts in the absorption, providing a direct correlation between the thermal decomposition of ligands to the morphology modulation, and as a result, to the physical properties of NPL solids.

| 4 ML CdSe NPLs | Cd | Se | C | Cd: Se |
|---|---|---|---|---|
| Native Myristate Ligand | 13.51 wt% | 10.81 wt% | 75.67 wt% | 1.25 |
| 250℃ in the air | 22.63 wt% | 18.44 wt% | 58.93 wt% | 1.23 |
| 300℃ in the air | 36.71 wt% | 29.63 wt% | 33.66 wt% | 1.24 |

**Table 5-1.** Elemental compositions of as-prepared CdSe NPLs, NPLs-Air-250 °C, and NPLs-Air-300 °C determined by SEM-EDX analysis.

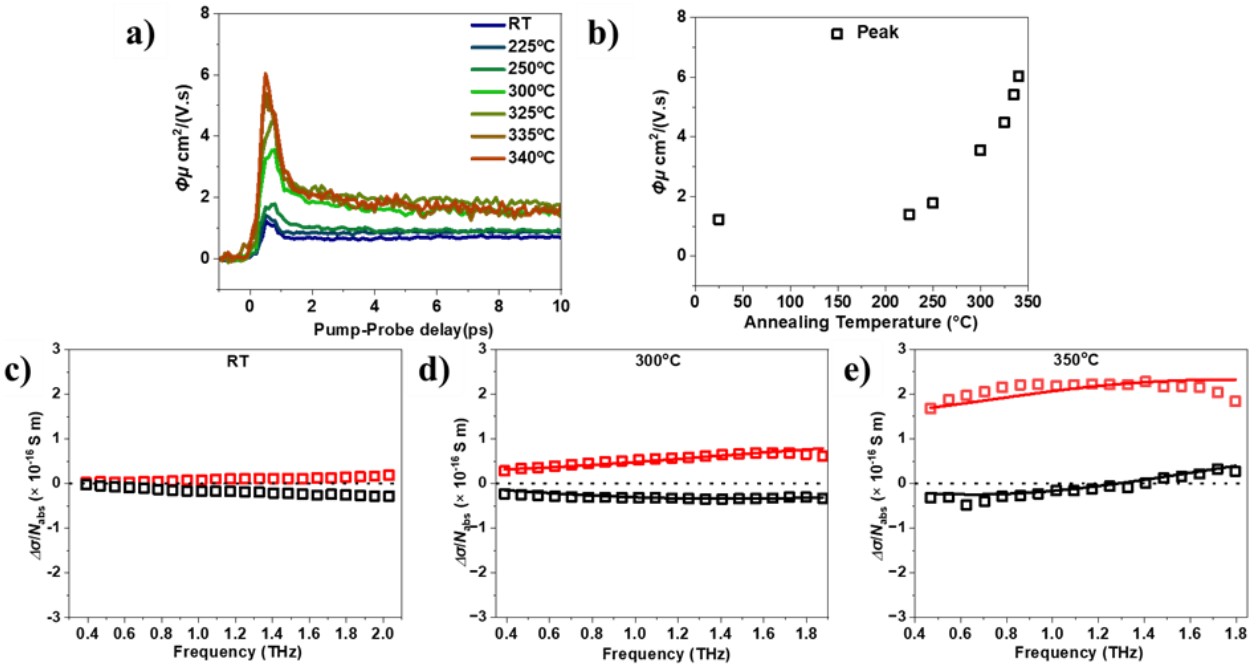


**Figure 5-4.** (a) Annealing-T-dependent photoconductivity dynamics by optical-pump-THz probe (OPTP) spectroscopy following 3.10 eV photoexcitation. (b) Normalized OPTP peak in (a) as a function of annealing T. Frequency-resolved photoconductivity spectra of (c) 4 ML CdSe NPLs with native ligand, (d) NPLs-300 °C and (e) NPLs-350 °C, respectively. The data are measured at 0.2 ps after the OPTP peak. The data are fitted by the Drude-Smith model, as described in the main text. The red and black solid lines represent the real and imaginary parts of the complex THz photoconductivity as modeled with the Drude-Smith model, respectively.

### 5.2.6 Photoconductivity measurements by THz spectroscopy

To investigate the effect of the shortened ligand length on the optoelectronic properties following thermal annealing at varied T, we employ contact-free, optical pump-THz probe (OPTP) spectroscopy to measure the time- and frequency-resolved photoconductivity with sub-ps time resolution. The pump-induced change in the conductivity, i.e., photoconductivity $\Delta\sigma$, is proportional to the photoinduced THz absorption ($\Delta E = E_{pump} - E$) at varying pump-probe delays, where Epump and E represent the transmitted THz field with and without photoexcitation (See Methods section). Figure 5-4a compares the photoconductivity dynamics of NPL films annealed at different T, normalized to the absorbed photon densities ($N_{abs}$). Though displaying a similar dynamic evolution within 10 ps, the different films show distinctly varied intensities. Specifically,

in line with all the structure and thermal analysis above, with increasing T over 250 °C, the OPTP intensity increases substantially, which is further demonstrated clearly in Figure 5-4b. Since $(\Delta\sigma)/N_{abs}$ is proportional to the product of the photon-to-free-carrier quantum yield $\phi$ and charge mobility $\mu$, the enhanced OPTP signal at elevated annealing T is attributed to a higher free carrier population and/or improved charge transport properties. As the averaged ligand length becomes shorter with annealing, the electronic coupling between the adjacent layers increases, which could give rise to an enhanced out-of-plane dielectric screening and reduced quantum confinement. These effects will greatly reduce the exciton binding energy and, thus, raise the proportion of the free electrons and holes. Besides, the out-of-plane charge transport across the adjacent NPLs will increase because of the enhanced inter-NPL electronic coupling.

To confirm and disentangle these two contributions from the free carrier density and charge mobility, we conducted THz time-domain spectroscopic (THz-TDS) analysis at a given pump-probe delay time. THz-TDS provides the frequency-resolved complex photoconductivity spectra, including the real and imaginary parts, as shown in Figures 5-4(c-e). At RT, the photoconductivity spectrum shows an exciton-dominated response with a finite real part and a pronounced negative imaginary part, which can be described by a Lorentz model.[188] This is in line with the large exciton binding energy of 170 meV in 4 ML CdSe NPLs with native ligands, which leads to a dominant exciton population. At high annealing T, the photoconductivity spectra change, as illustrated in Figures 5-4d and 5-4e, and are dominated by the real component, indicating the free-carrier-dominated dynamics. The conductivity dispersion can be adequately described by the so-called Drude-Smith model:[188]

$$\sigma_{Drude-Smith} = \frac{\omega_p^2 \varepsilon_0 \tau}{1 - i\omega\tau}\left(1 + \frac{c}{1 - i\omega\tau}\right)$$

Here, $\tau$, $\omega_p$, and $\varepsilon_0$ are the effective scattering time, plasma frequency, and vacuum permittivity, respectively. In this model, free carriers dominate the photo-response and experience preferential back-scattering resulting from spatial confinement due to e.g., grain boundaries or interfaces.[189,190] This effect is evaluated quantitatively by the parameter c ranging from -1 to 0. When $c$ = 0, the free carriers undergo a Drude-like transport with a momentum-randomizing scattering; for $c$ = -1, these free carriers are subject to a complete back-scattering with strong confinement. As shown in Table 5-2, the extracted parameter c from the fits increases with increasing the annealing T, which indicates reduced confinement of the photogenerated free

carriers as the interlayer distance becomes smaller. When T = 350 °C, there is a significant and sudden jump of the parameter c and scattering time: for the former, it reduces from close to -0.95 to -0.67, and for the latter, there is a large increase from 40-50 to ~70 fs. This result is in line with our expectation, in which a structural transition from quasi-2D to 3D with the complete removal of the interlayer ligands. Both parameters have changed in a direction to substantially enhance the short-range charge carrier mobility at the dc limits, following $\mu = \frac{e\tau}{m^*}(1 + c)$, by increasing the annealing T from 250 to 350 °C. The free carrier density increases gradually by T, and the free carrier generation quantum yields are estimated to increase from ~1.0 % to 2.8% between 250 to 350 °C based on the fitting.

| Annealing temperature (°C) | τ (fs) | c | Carrier density ($m^{-3}$) |
|---|---|---|---|
| 250 | $43 \pm 3$ | $-0.95 \pm 0.01$ | $4.17 \times 10^{21} \pm 1 \times 10^{19}$ |
| 300 | $44 \pm 2$ | $-0.87 \pm 0.01$ | $8.35 \times 10^{21} \pm 2 \times 10^{19}$ |
| 325 | $47 \pm 5$ | $-0.89 \pm 0.03$ | $8.54 \times 10^{21} \pm 5 \times 10^{19}$ |
| 335 | $49 \pm 4$ | $-0.83 \pm 0.01$ | $9.08 \times 10^{21} \pm 3 \times 10^{19}$ |
| 350 | $69 \pm 5$ | $-0.67 \pm 0.02$ | $12.10 \times 10^{21} \pm 2 \times 10^{19}$ |

**Table 5-2.** The obtained Drude-Smith parameters for different temperatures.

## 5.3 Conclusion

In summary, we report that thermal annealing represents an effective strategy to tune the optical absorption and electrical properties of NPL assemblies by controlling the inter-NPL distance. The underlying mechanism for such morphology control lies in the stability of the surface ligands: we observe a direct correlation between the T-dependent ligand decomposition and the NPL-NPL distance shortening (by TEM), the strong red-shift in the absorption band edge (by UV-vis studies), and furthermore, the enhanced electrical transport within the NPL films. Our results illustrate a straightforward manner to control the interfacial electronic coupling strength for developing functional optoelectronics through thermal treatments.

# Chapter 6: Summary and Conclusion

Thanks to their excellent optical properties including size-tunable photoluminescence, cadmium/lead chalcogenide nanocrystals (NCs, e.g. nanoplatelets) have shown great promise for optoelectronics, in particular for light emission applications. The toxicity of cadmium/lead, on the other hand, has hampered their device integration and further commercialization. In addition, processing NCs from solution into optoelectronic devices requires a detailed understanding of the colloidal stability of NCs in dispersion, which has not been well-studied. Finally, understanding and controlling the inter-NC electronic coupling on the transport effects of photogenerated charge carriers play a fundamentally important role in optimizing device performance. To this end, we are dedicated to understanding the synthesis mechanism of nontoxic InP semiconducting nanocrystals, unveiling the key parameters regulating the colloidal stability of CdSe NPLs dispersion, and probing the charge carrier dynamics in CdSe NPLs thin films.

Following the introduction and motivation presented in **Chapter 1**, we presented the materials synthesis details and techniques used in the thesis in **Chapter 2**. **Chapter 3** presents a facile approach to synthesizing nontoxic, nanostructured InP via a high-temperature (230–320 °C) reaction with the co-presence of indium chloride and indium acetate with triphenyl phosphite. Our work revealed that the formation of InP proceeds via the chemical transformation of pre-synthesized $In_2O_3$ NCs.

In **Chapter 4**, we investigate the colloidal stability or aggregation process of CdSe NPLs by combining THz photoconductivity measurements and simulations. We experimentally demonstrate that increasing NPLs' facet area or the solvent length leads to decrease in the critical concentration at which NPL starts aggregation. Simulations by our collaborators Peterson et.al have revealed the dominant role of the solvation forces in determining the NC stability: increasing the facet area of NPLs and the length of the solvent increase the NPL solvation force to induce aggregation.

In **Chapter 5**, we employ thermal annealing as an effective method to control the inter-NPL distance, further the optical absorption and electrical properties of assembled NPL solids. We provide a direct correlation between the T-dependent ligand decomposition and the NPL-NPL distance shortening (by transmission electron microscopy), the strong red shift in the absorption

band edge (by UV-vis studies), and the enhanced electrical transport within NPL films. The TGA-MS analysis confirms that the ligand decomposition at elevated temperatures decreases gradually the inter-NPL distance and thus enhances the electrical properties of NPL solids.

Overall, this thesis provides a new way to synthesize nontoxic anisotropic and hyperbranched InP NCs. In addition, we demonstrate how the solvation force governs the colloidal stability, and how to control the electronic coupling in NPL solids for enhanced charge transport properties by thermal annealing.

# Appendix

## Chapter 3

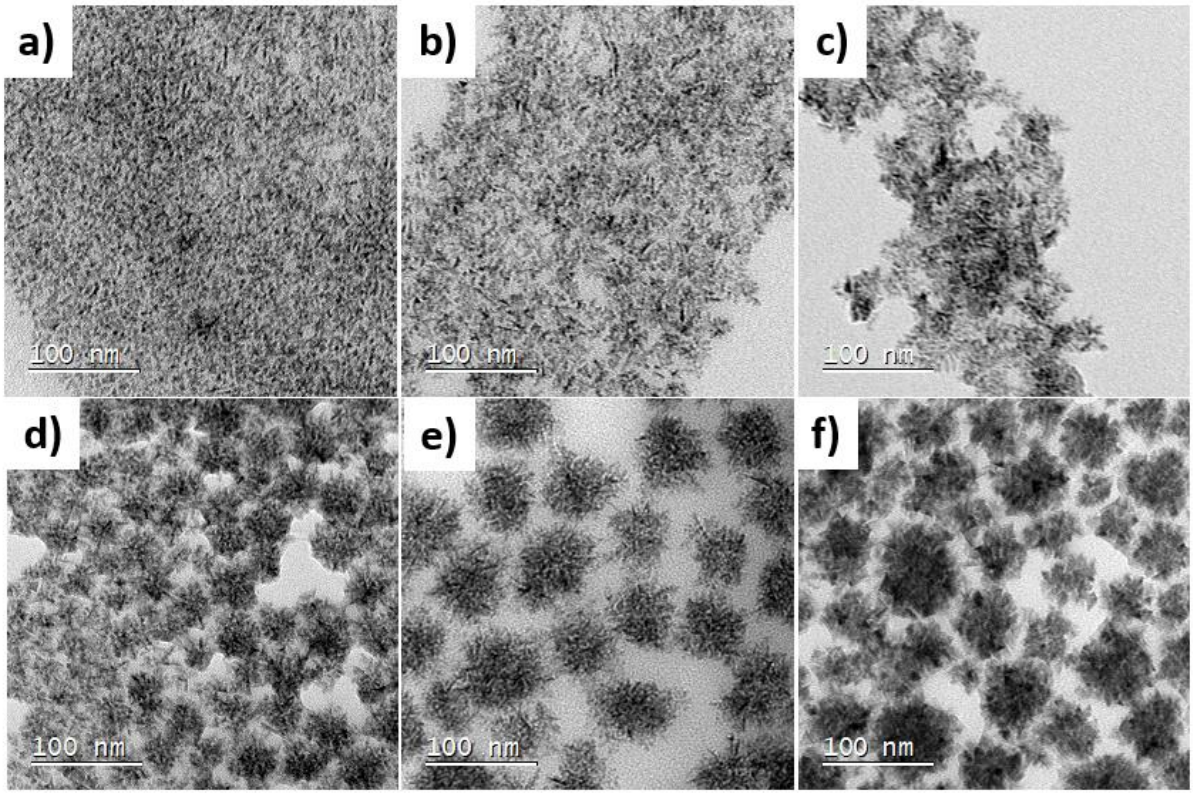


**Figure A3-1.** TEM images of InP NCs synthesized at different temperatures. (a) 230 °C. (b) 240 °C. (c) 250 °C. (d) 260 °C. (e) 280 °C. (f) 300 °C.

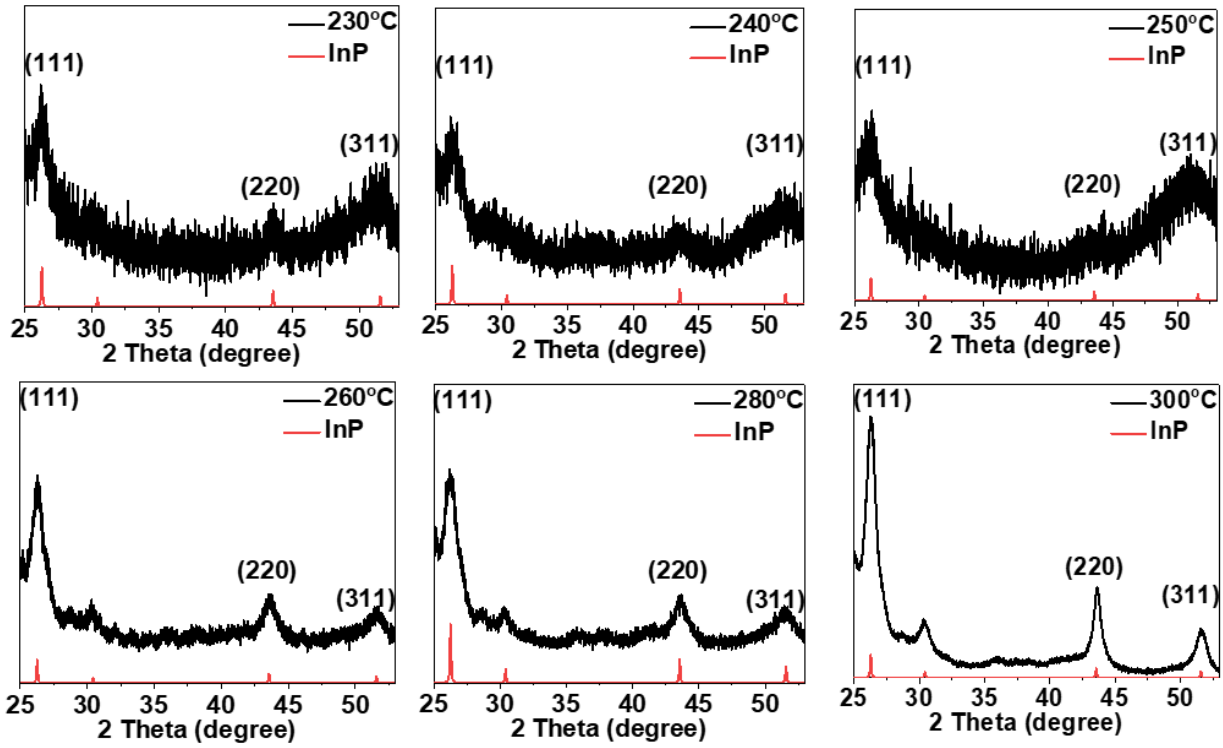


**Figure A3-2.** PXRD of InP NCs synthesized at different temperatures. (a) 230 °C. (b) 240 °C. (c) 250 °C. (d) 260 °C. (e) 280 °C. (f) 300 °C.

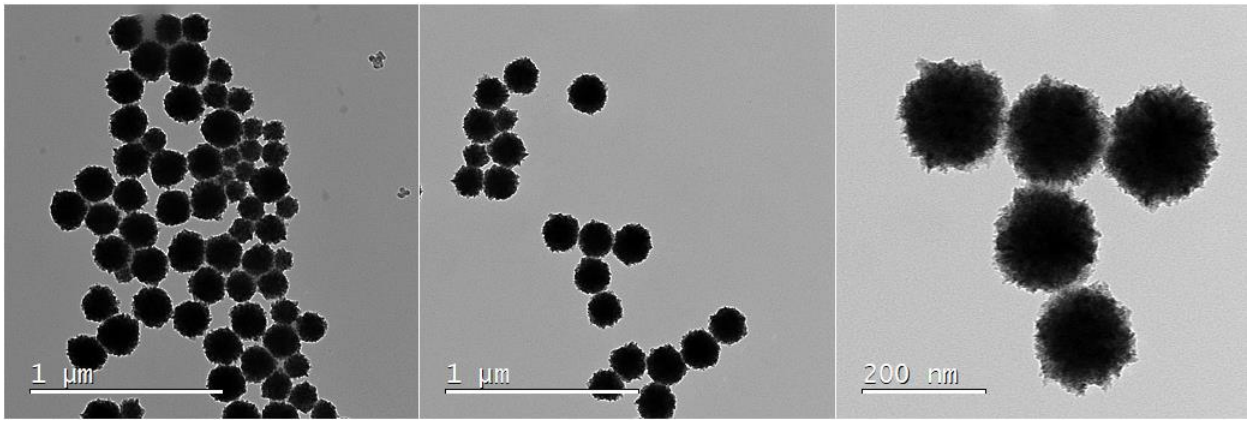


**Figure A3-3.** TEM of InP with 1 mL TPOP added.

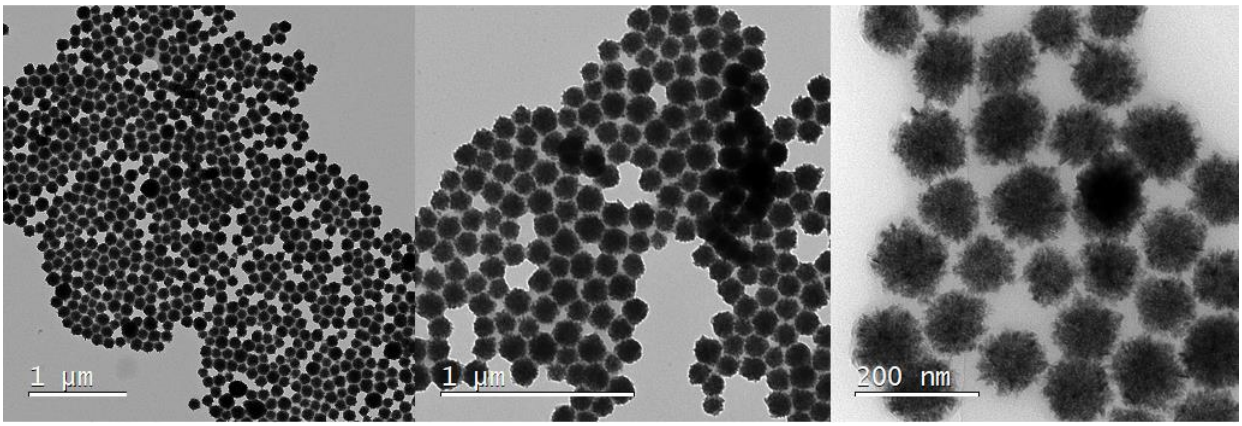


**Figure A3-4.** TEM of InP with 1.5 mL TPOP added.

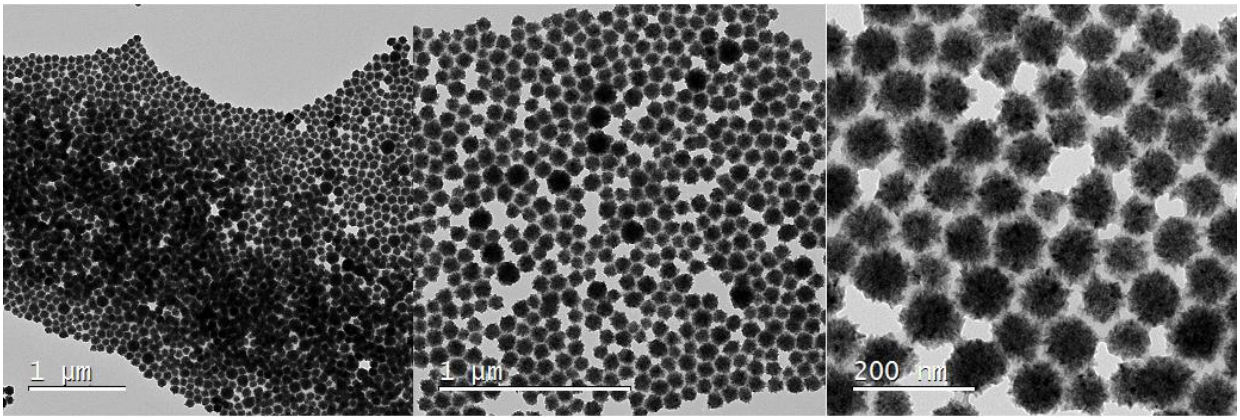


**Figure A3-5.** TEM of InP with 2 mL TPOP added.

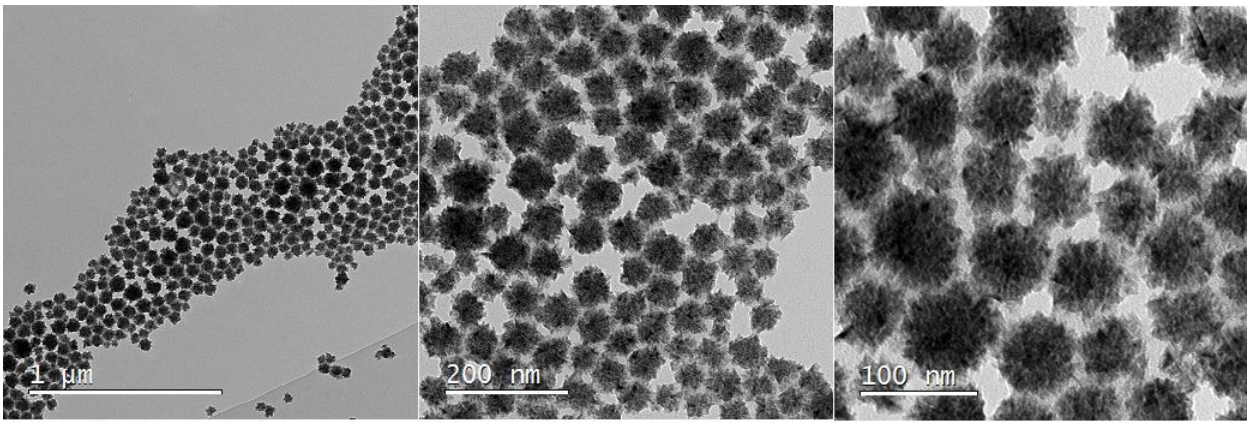


**Figure A3-6.** TEM of InP with 2.5 mL TPOP added.

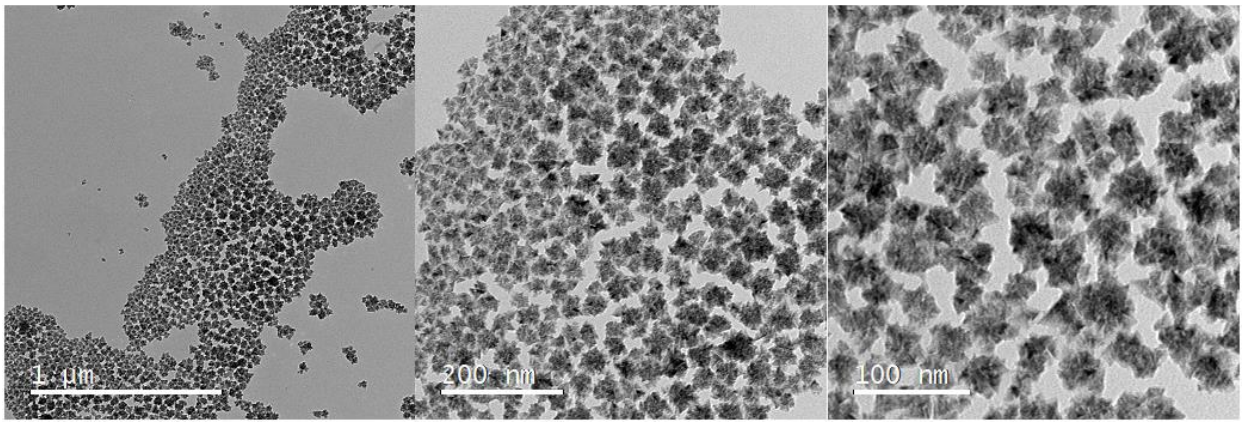


**Figure A3-7.** TEM of InP with 3 mL TPOP added.

## Chapter 4

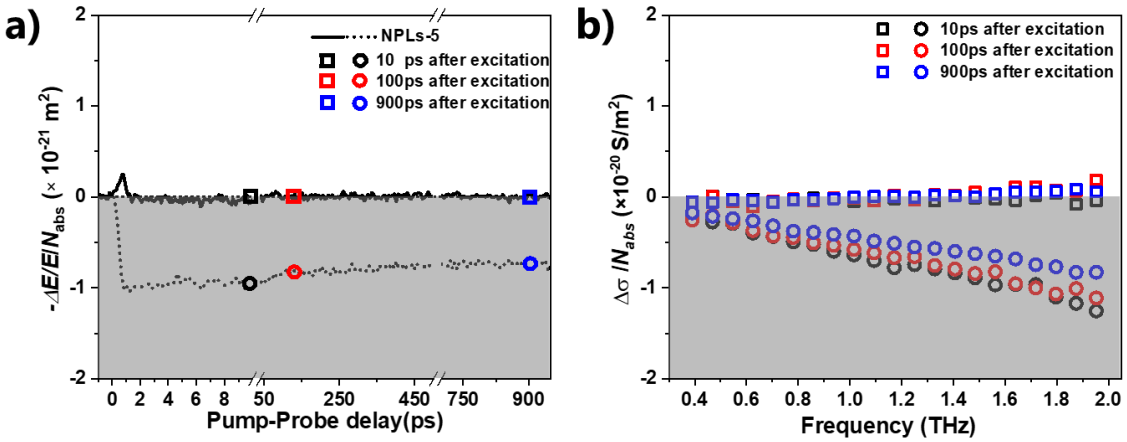


**Figure A4-1.** (a) The time-resolved THz conductivity following 3.1 eV excitation. (b) Frequency-resolved THz conductivity was measured at 10, 100, and 900 ps after photoexcitation following excitations of 3.1 eV excitation.

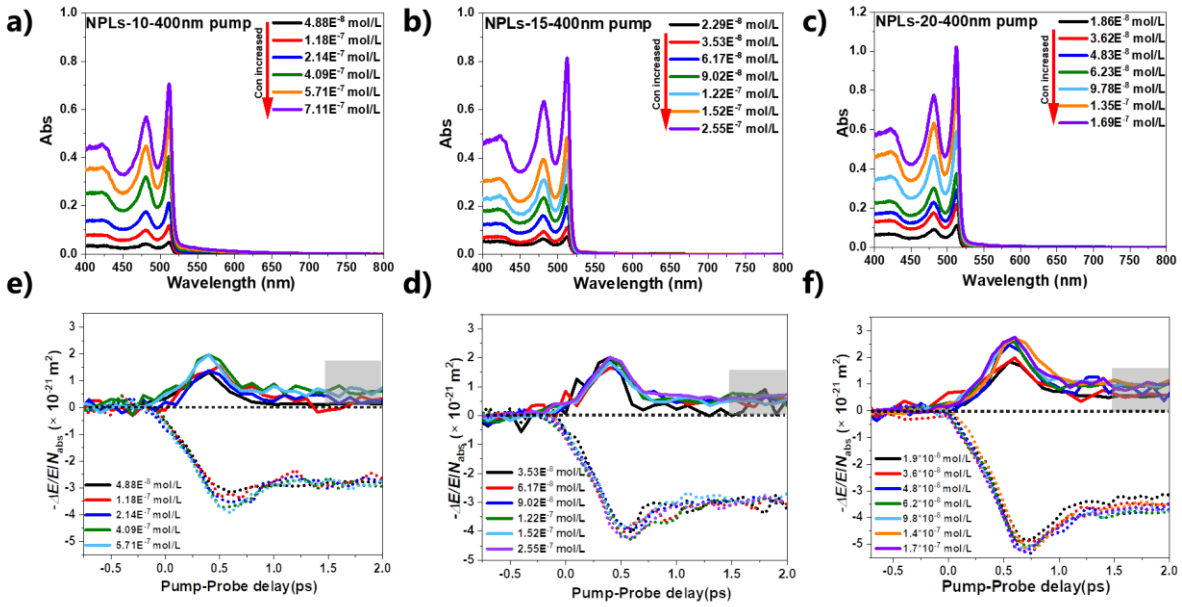


**Figure A4-2.** The UV-vis absorption spectra of NPLs-10 (a), 15 (b), and 20 (c) with different concentrations. The concentration-dependent, time-resolved THz conductivity following 3.1eV excitation of NPLs-10 (e), 15 (d), and 20 (f) respectively.

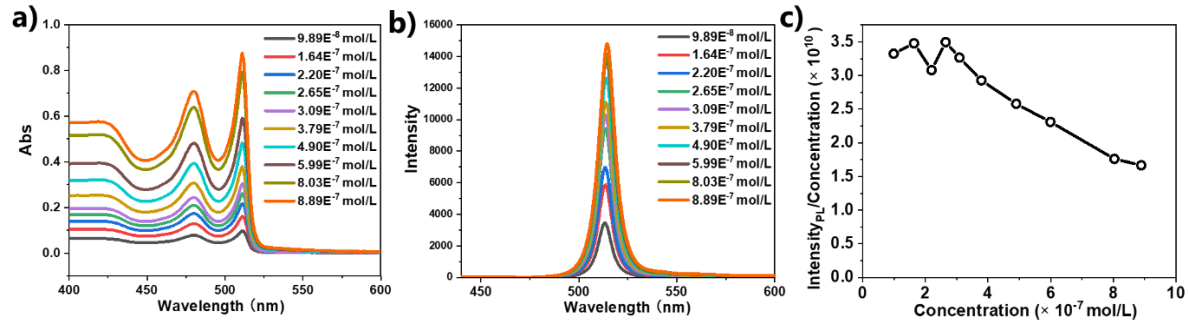


**Figure A4-3.** The UV-vis absorption (a) and PL (b) spectra of NPLs-10 with different concentrations. (c) The ratio between (a) and (b).

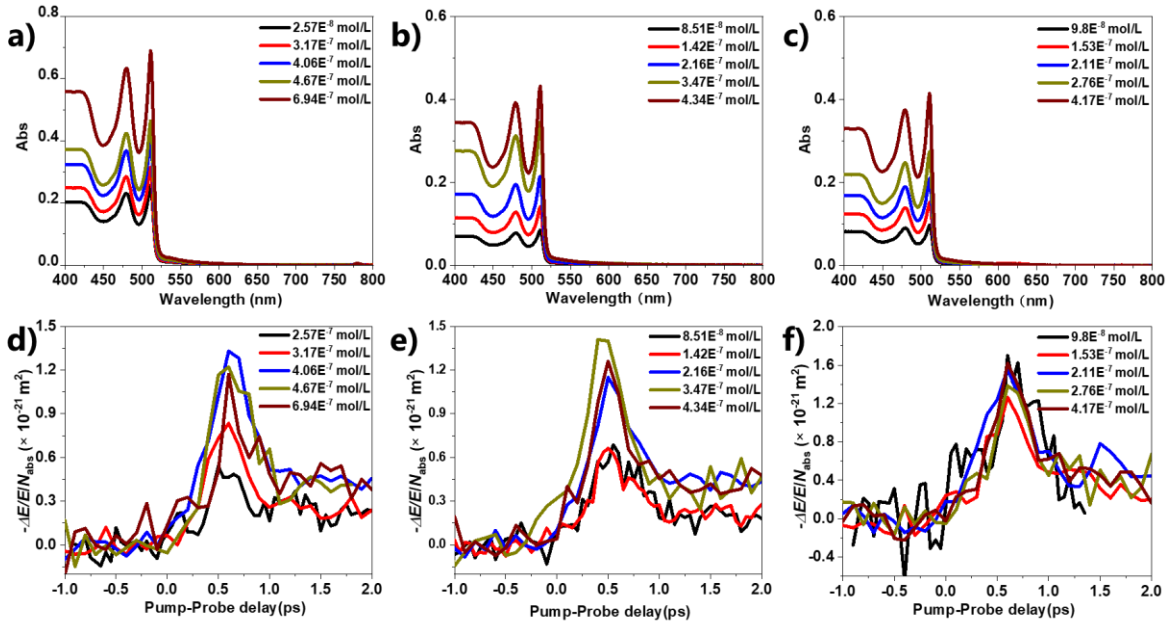


**Figure A4-4.** The UV-vis absorption spectra of NPLs in octane (a), decane (b), and dodecane (c) with different concentrations. The concentration-dependent, time-resolved THz conductivity following 3.1eV excitation of NPLs- in octane (d), decane (e), and dodecane (f) respectively.

## Chapter 5

### Characterization:

### Transmission Electron Microscopy (TEM):

TEM grid. Conventional bright-field TEM imaging was carried out on a JEOL JEM-1400 microscope equipped with an accelerating voltage of 120 kV. NPLs' sizes were measured from the TEM images by using Image J. The distance NPL-NPL was measured from the TEM images by using Digital Micrograph.

### UV−Vis Absorption Spectroscopy:

The absorption spectra of the dispersion and film were measured using an Agilent Cary 60 UV-Vis spectrometer between 300-1000 nm or an Avantes UV-Vis spectrometer between 400-800 nm consisting of Avantes Ava Light-DH-S-BAL as the UV−Vis light source passing through

a neutral density filter (optical density = 2.0) and fiber-coupled to an Avantes Sens Line Ava Spec-HSC-TEC detector.

**Raman Spectroscopy:**

The Raman spectra 4 ML CdSe NPLs films under various temperatures and gas were recorded with a confocal Raman spectrometer (alpha 300 R, ×10 objective, 600 grooves/mm grating, 5 mw) with a 532 nm excitation and 10 seconds integration.

**Scanning Electron Microscopy**:

SEM imaging was performed on a Zeiss LEO Gemini 1530 Scanning Electron Microscope (Zeiss) with an accelerating voltage of 3 kV.

**Thermogravimetric Analysis with Mass-Spectrometry**:

The TGA-MA measurements were conducted on an STA 449 F5 Jupiter (Netzsch) coupled with an MS Aëolos® (Netzsch).

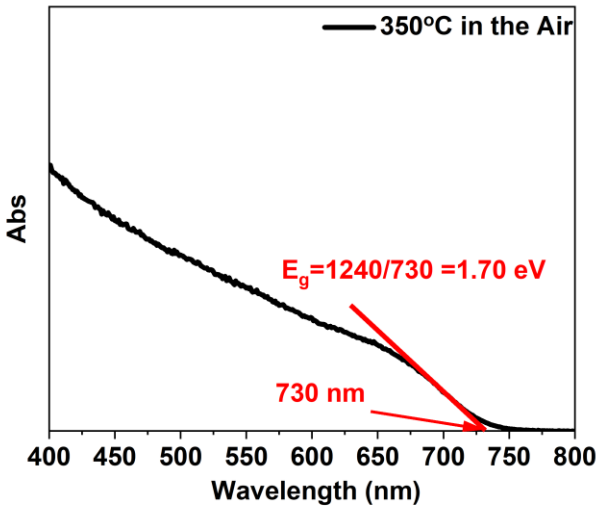


**Figure A5-1**. Absorption spectra of 4 ML CdSe NPLs film annealing at 350 °C in the air for 30 min.

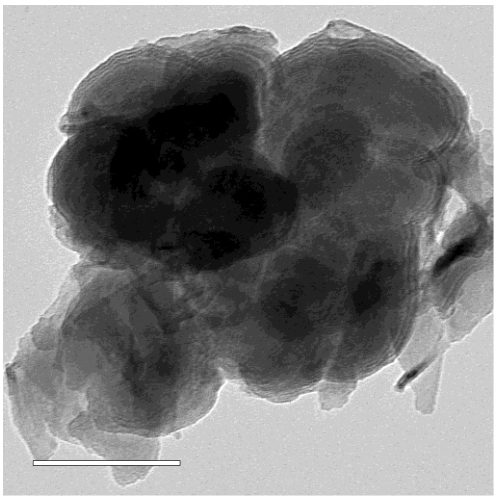

**Figure A5-2**. TEM images of 4 ML CdSe NPLs after annealing at 350 °C in the air.

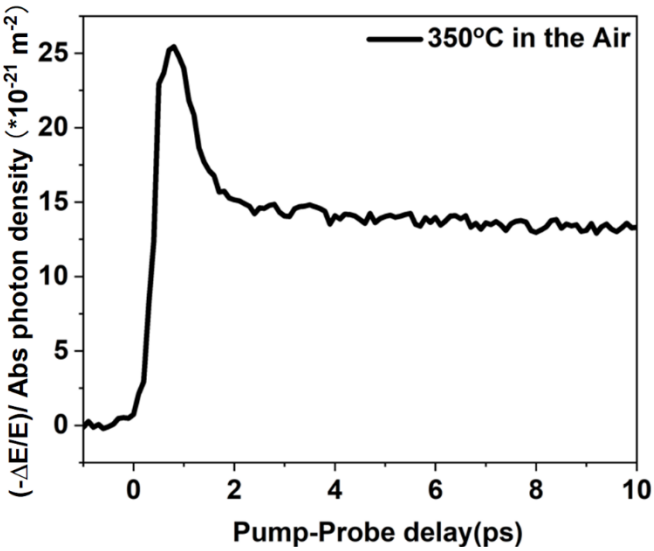


**Figure A5-3**. The photoconductivity dynamics by optical-pump THz probe technique following 3.10 eV photon excitation of annealing at 350 °C in the air.

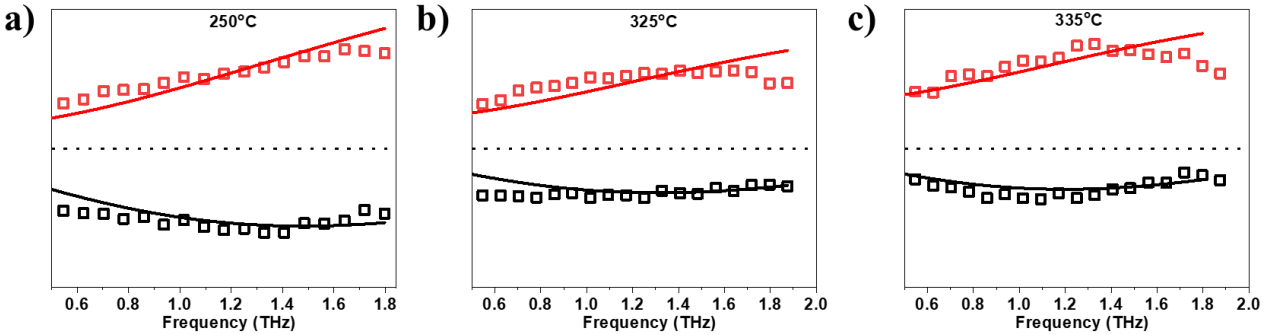

**Figure A5-4**. Frequency dependence THz conductivity at 0.2 ps after 400 nm excitation of (a) NPLs-250 °C, (b) NPLs-325 °C, and (c) NPLs-335 °C. The lines are fitted to the Drude-Smith model (the red solid for the real, and the black dash for the imaginary).

| Temperature °C | 25 | 200 | 250 | 284 | 300 | 355 | 475 |
|---|---|---|---|---|---|---|---|
| Weight % | 100% | 99.06% | 98.41% | 96.13% | 89.65% | 36.26% | 24.68% |

**Table A5-1.** The weight loss with the temperature range.

## Reference

(1) Faraday, M. X. The Bakerian Lecture: Experimental Relations of Gold (and Other Metals) to Light. *Philos. Trans. R. Soc.* **1857**, 147, 145-181.

(2) Talapin, D. V.; Shevchenko, E. V. Introduction: Nanoparticle Chemistry. *Chem. Rev.* **2016**, 116 (18), 10343-10345.

(3) Mueller, T.; Malic, E. Exciton Physics and Device Application of Two-Dimensional Transition Metal Dichalcogenide Semiconductors. *npj 2D Mater. Appl.* **2018**, 2 (1), 29.

(4) Ekimov, A.; Onuschenko, A. Quantum Size Effect in Three-Dimensional Microscopic Semiconductor Crystals. *JETP Lett.* **1981**, 34 (6), 363.

(5) Rossetti, R.; Nakahara, S.; Brus, L. E. Quantum Size Effects in the Redox Potentials, Resonance Raman Spectra, and Electronic Spectra of CdS Crystallites in Aqueous Solution. *J. Chem. Phys.* **1983**, 79 (2), 1086-1088.

(6) Peng, Z. A.; Peng, X. G. Formation of High-Quality CdTe, CdSe, and CdS Nanocrystals Using CdO as Precursor. *J. Am. Chem. Soc.* **2001**, 123 (1), 183–184.

(7) Kortshagen, U. R.; Sankaran, R. M.; Pereira, R. N.; Girshick, S. L.; Wu, J. J.; Aydil, E. S. Nonthermal Plasma Synthesis of Nanocrystals: Fundamental Principles, Materials, and Applications. *Chem. Rev.* **2016**, 116 (18), 11061-11127.

(8) Knowles, K. E.; Hartstein, K. H.; Kilburn, T. B.; Marchioro, A.; Nelson, H. D.; Whitham, P. J.; Gamelin, D. R. Luminescent Colloidal Semiconductor Nanocrystals Containing Copper: Synthesis, Photophysics, and Applications. *Chem. Rev.* **2016**, 116 (18), 10820-10851.

(9) Jing, L.; Kershaw, S. V.; Li, Y.; Huang, X.; Li, Y.; Rogach, A. L.; Gao, M. Aqueous Based Semiconductor Nanocrystals. *Chem. Rev.* **2016**, 116 (18), 10623-10730.

(10) Krahne, R.; Morello, G.; Figuerola, A.; George, C.; Deka, S.; Manna, L. Physical Properties of Elongated Inorganic Nanoparticles. *Phys. Rep.* **2011**, 501 (3), 75-221.

(11) Peng, L.; Cho, W.; Zhang, X.; Talapin, D.; Ma, X. Observation of Biexciton Emission from Single Semiconductor Nanoplatelets. *Phys. Rev. Materials* **2021**, 5, L051601.

(12) Konstantatos, G.; Sargent, E. Colloidal Quantum Dot Optoelectronics and Photovoltaics; *Cambridge University Press*, **2013**.

(13) Warner, J. H.; Hoshino, A.; Yamamoto, K.; Tilley, R. D. Water-Soluble Photoluminescent Silicon Quantum Dots. *Angew. Chem. Int. Ed.* **2005**, 44 (29), 4550-4554.

(14) Fok, E.; Shih, M.; Meldrum, A.; Veinot, J. G. C. Preparation of Alkyl-Surface Functionalized Germanium Quantum Dots via Thermally Initiated Hydrogermylation. *Chem. Commun.* **2004**, (4), 386-387.

(15) Li, Y.; Liu, E. C. Y.; Pickett, N.; Skabara, P. J.; Cummins, S. S.; Ryley, S.; Sutherland, A. J.; O'Brien, P. Synthesis and Characterization of CdS Quantum Dots in Polystyrene Microbeads. *J. Mater. Chem.* **2005**, 15 (12), 1238-1243.

(16) Wang, Q.; Seo, D.-K. Synthesis of Deep-Red-Emitting CdSe Quantum Dots and General Non-Inverse-Square Behavior of Quantum Confinement in CdSe Quantum Dots. *Chem. Mater.* **2006**, 18 (24), 5764-5767.

(17) Kamal, J. S.; Omari, A.; Van Hoecke, K.; Zhao, Q.; Vantomme, A.; Vanhaecke, F.; Capek, R. K.; Hens, Z. Pyroelectricity of Lead Sulfide (PbS) Quantum Dot Films Induced by Janus-Ligand Shells. *J. Phys. Chem. C* **2012**, 116 (8), 5049-5054.

(18) Jun, Y.-w.; Koo, J.-E.; Cheon, J. One-Step Synthesis of Size Tuned Zinc Selenide Quantum Dots a Temperature Controlled Molecular Precursor Approach. *Chem. Commun*. **2000**, (14), 1243-1244.

(19) Huang, Z.; Hao, J.; Blackburn, J. L.; Beard, M. C. Pyroelectricity of Lead Sulfide (PbS) Quantum Dot Films Induced by Janus-Ligand Shells. *ACS Nano* **2021**, 15 (9), 14965-14971.

(20) Ahmad, W.; He, J.; Liu, Z.; Xu, K.; Chen, Z.; Yang, X.; Li, D.; Xia, Y.; Zhang, J.; Chen, C. Lead Selenide (PbSe) Colloidal Quantum Dot Solar Cells with >10% Efficiency. *Adv. Mater.* **2019**, 31 (33), 1900593.

(21) Yu, H.; Li, J.; Loomis, R. A.; Wang, L.-W.; Buhro, W. E. Two-Versus Three-Dimensional Quantum Confinement in Indium Phosphide Wires and Dots. *Nat. Mater.* **2003**, 2 (8), 517-520.

(22) Wang, F.; Yu, H.; Jeong, S.; Pietryga, J. M.; Hollingsworth, J. A.; Gibbons, P. C.; Buhro, W. E. The Scaling of the Effective Band Gaps in Indium−Arsenide Quantum Dots and Wires. *ACS Nano* **2008**, 2 (9), 1903-1913.

(23) Reiss, P.; Carriere, M.; Lincheneau, C.; Vaure, L.; Tamang, S. Synthesis of Semiconductor Nanocrystals, Focusing on Nontoxic and Earth-Abundant Materials. *Chem. Rev.* **2016**, 116 (18), 10731-10819.

(24) Cotta, M. A. Quantum Dots and Their Applications: What Lies Ahead? *ACS Appl. Nano Mater.* **2020**, 3 (6), 4920-4924.

(25) Micic, O. I.; Curtis. C. J.; Jones, K. M.; Sprague, J. R.; Nozik, A. J. Synthesis and Characterization of InP Quantum Dots. *J. Phys. Chem.* **1994**, 98 (19), 4966–4969.

(26) Gibson, S. J.; van Kasteren, B.; Tekcan, B.; Cui, Y.; van Dam, D.; Haverkort, J. E. M.; Bakkers, E.; Reimer, M. E. Tapered InP Nanowire Arrays for Efficient Broadband High-Speed Single-Photon Detection. *Nat. Nanotechnol.* **2019**, 14 (5), 473-479.

(27) Kwon, Y.; Oh, J.; Lee, E.; Lee, S. H.; Agnes, A.; Bang, G.; Kim, J.; Kim, D.; Kim, S. Evolution from Unimolecular to Colloidal-Quantum-Dot-like Character in Chlorine or Zinc Incorporated InP Magic Size Clusters. *Nat. Commun.* **2020**, 11 (1), 3127.

(28) Click, S. M.; Rosenthal, S. J. Synthesis, Surface Chemistry, and Fluorescent Properties of InP Quantum Dots. *Chem. Mater.* **2023**, 35 (3), 822–836.

(29) Achorn, O. B.; Franke, D.; Bawendi, M. G. Seedless Continuous Injection Synthesis of Indium Phosphide Quantum Dots as a Route to Large Size and Low Size Dispersity. *Chem. Mater.* **2020**, 32 (15), 6532–6539.

(30) Kim, K.; Yoo, D.; Choi, H.; Tamang, S.; Ko, J. H.; Kim, S.; Kim, Y. H.; Jeong, S. Halide-Amine Co-Passivated Indium Phosphide Colloidal Quantum Dots in Tetrahedral Shape. *Angew. Chem. Int. Ed.* **2016**, 55 (11), 3714-3718.

(31) Kim, Y.; Choi, H.; Lee, Y.; Koh, W.-K.; Cho, E.; Kim, T.; Kim, H.; Kim, Y.-H.; Jeong, H. Y.; Jeong, S. Tailored Growth of Single-Crystalline InP Tetrapods. *Nat. Commun.* **2021**, 12 (1), 4454.

(32) Xie, R. G.; Li. Z.; Peng, X. G. Nucleation Kinetics vs Chemical Kinetics in the Initial Formation of Semiconductor Nanocrystals. *J. Am. Chem. Soc.* **2009**, 131 (42), 15457–15466.

(33) Choi, S.-W.; Kim, H.-M.; Yoon, S.-Y.; Jo, D.-Y.; Kim, S.-K.; Kim, Y.; Park, S. M.; Lee, Y.-J.; Yang, H. Aminophosphine-Derived, High-Quality Red-Emissive InP Quantum Dots by the Use of an Unconventional in Halide. *J. Mater. Chem. C* **2022**, 10 (6), 2213-2222.

(34) Xie, L.; Zhao, Q.; Jensen, K. F.; Kulik, H. J. Direct Observation of Early-Stage Quantum Dot Growth Mechanisms with High-Temperature Ab Initio Molecular Dynamics. *J. Phys. Chem. C* **2016**, 120 (4), 2472-2483.

(35) Tamang, S.; Lincheneau, C.; Hermans, Y.; Jeong, S.; Reiss, P. Chemistry of InP Nanocrystal Syntheses. *Chem. Mater.* **2016**, 28 (8), 2491-2506.

(36) Leemans, J.; Dümbgen, K. C.; Minjauw, M. M.; Zhao, Q.; Vantomme, A.; Infante, I.; Detavernier, C.; Hens, Z. Acid–Base Mediated Ligand Exchange on Near-Infrared Absorbing, Indium-Based III–V Colloidal Quantum Dots. *J. Am. Chem. Soc.* **2021**, 143 (11), 4290-4301.

(37) Yu, S.; Fan, X.-B.; Wang, X.; Li, J.; Zhang, Q.; Xia, A.; Wei, S.; Wu, L.-Z.; Zhou, Y.; Patzke, G. R. Efficient Photocatalytic Hydrogen Evolution with Ligand Engineered All-Inorganic InP and InP/ZnS Colloidal Quantum Dots. *Nat. Commun.* **2018**, 9 (1), 4009.

(38) Cros-Gagneux, A.; Delpech, F.; Nayral, C.; Cornejo, A.; Coppel, Y.; Chaudret, B. Surface Chemistry of InP Quantum Dots: A Comprehensive Study. *J. Am. Chem. Soc.* **2010**, 132 (51), 18147-18157.

(39) Mićić, O. I.; Sprague, J.; Lu, Z.; Nozik, A. J. Highly Efficient Band-Edge Emission from InP Quantum Dots. *Appl. Phys. Lett.* **1996**, 68 (22), 3150-3152.

(40) Adam, S.; Talapin, D. V.; Borchert, H.; Lobo, A.; McGinley, C.; Castro, A. R. B. d.; Haase, M.; Weller, H.; Möller, T. The Effect of Nanocrystal Surface Structure on the Luminescence Properties: Photoemission Study of HF-Etched InP Nanocrystals. *J. Chem. Phys.* **2005**, 123 (8), 084706.

(41) Hughes, K. E.; Stein, J. L.; Friedfeld, M. R.; Cossairt, B. M.; Gamelin, D. R. Effects of Surface Chemistry on the Photophysics of Colloidal InP Nanocrystals. *ACS Nano* **2019**, 13 (12), 14198-14207.

(42) Stein, J. L.; Mader, E. A.; Cossairt, B. M. Luminescent InP Quantum Dots with Tunable Emission by Post-Synthetic Modification with Lewis Acids. *J. Phys. Chem. Lett.* **2016**, 7 (7), 1315-1320.

(43) Nasilowski, M.; Mahler, B.; Lhuillier, E.; Ithurria, S.; Dubertret, B. Two-Dimensional Colloidal Nanocrystals. *Chem. Rev.* **2016**, 116 (18), 10934-10982.

(44) Mir, S. H.; Yadav, V. K.; Singh, J. K. Recent Advances in the Carrier Mobility of Two-Dimensional Materials: A Theoretical Perspective. *ACS Omega* **2020**, 5 (24), 14203-14211.

(45) Hu, Z.; O'Neill, R.; Lesyuk, R.; Klinke, C. Colloidal Two-Dimensional Metal Chalcogenides: Realization and Application of the Structural Anisotropy. *Acc. Chem. Res.* **2021**, 54 (20), 3792-3803.

(46) Joo, J.; Son, J. S.; Kwon, S. G.; Yu, J. H.; Hyeon, T. Low-Temperature Solution-Phase Synthesis of Quantum Well Structured CdSe Nanoribbons. *J. Am. Chem. Soc.* **2006**, 128 (17), 5632-5633.

(47) Son, J. S.; Wen, X. D.; Joo, J.; Chae, J.; Baek, S. I.; Park, K.; Kim, J. H.; An, K.; Yu, J. H.; Kwon, S. G.; et al. Large-Scale Soft Colloidal Template Synthesis of 1.4 nm Thick CdSe Nanosheets. *Angew. Chem. Int. Ed.* **2009**, 48 (37), 6861-6864.

(48) Ithurria, D. S.; Dubertret, B. Quasi 2D Colloidal CdSe Platelets with Thicknesses Controlled at the Atomic Level. *J. Am. Chem. Soc.* **2008**, 130 (49), 16504–16505.

(49) Li, Q.; Lian, T. Area- and Thickness-Dependent Biexciton Auger Recombination in Colloidal CdSe Nanoplatelets: Breaking the "Universal Volume Scaling Law". *Nano Lett.* **2017**, 17 (5), 3152-3158.

(50) She, C.; Fedin, I.; Dolzhnikov, D. S.; Dahlberg, P. D.; Engel, G. S.; Schaller, R. D.; Talapin, D. V. Red, Yellow, Green, and Blue Amplified Spontaneous Emission and Lasing Using Colloidal CdSe Nanoplatelets. *ACS Nano* **2015**, 9 (10), 9475-9485.

(51) Christodoulou, S.; Climente, J. I.; Planelles, J.; Brescia, R.; Prato, M.; Martin-Garcia, B.; Khan, A. H.; Moreels, I. Chloride-Induced Thickness Control in CdSe Nanoplatelets. *Nano Lett.* **2018**, 18 (10), 6248-6254.

(52) Cho, W.; Kim, S.; Coropceanu, I.; Srivastava, V.; Diroll, B. T.; Hazarika, A.; Fedin, I.; Galli, G.; Schaller, R. D.; Talapin, D. V. Direct Synthesis of Six-Monolayer (1.9 nm) Thick Zinc-Blende CdSe Nanoplatelets Emitting at 585 nm. *Chem. Mater.* **2018**, 30 (20), 6957-6960.

(53) Chu, A.; Livache, C.; Ithurria, S.; Lhuillier, E. Electronic Structure Robustness and Design Rules for 2D Colloidal Heterostructures. *J. Appl. Phys.* **2018**, 123 (3), 035701.

(54) Petersen, N.; Girard, M.; Riedinger, A.; Valsson, O. The Crucial Role of Solvation Forces in the Steric Stabilization of Nanoplatelets. *Nano Lett.* **2022**, 22 (24), 9847–9853.

(55) Guillemeney, L.; Lermusiaux, L.; Landaburu, G.; Wagnon, B.; Abécassis, B. Curvature and Self-Assembly of Semi-Conducting Nanoplatelets. *Commun. Chem.* **2022**, 5 (1), 7.

(56) Tessier, M. D.; Biadala, L.; Bouet, C.; Ithurria, S.; Abecassis, B.; Dubertret, B. Phonon Line Emission Revealed by Self-Assembly of Colloidal Nanoplatelets. *ACS Nano* **2013**, 7 (4), 3332-3340.

(57) Abecassis, B.; Tessier, M. D.; Davidson, P.; Dubertret, B. Self-assembly of CdSe Nanoplatelets into Giant Micrometer-scale Needles Emitting Polarized Light. *Nano Lett.* **2014**, 14 (2), 710-715.

(58) Momper, R.; Zhang, H.; Chen, S.; Halim, H.; Johannes, E.; Yordanov, S.; Braga, D.; Blulle, B.; Doblas, D.; Kraus, T.; Bonn, M.; Wang, H. I;. Riedinger, A. Kinetic Control over Self-Assembly of Semiconductor Nanoplatelets. *Nano Lett.* **2020**, 20 (6), 4102–4110.

(59) Guzelturk, B.; Erdem, O.; Olutas, M.; Kelestemur, Y.; Demir, H. V. Stacking in Colloidal Nanoplatelets: Tuning Excitonic Properties. *ACS Nano* **2014**, 8 (12), 12524-12533.

(60) Miethe, J. F.; Schlosser, A.; Eckert, J. G.; Lübkemann, F.; Bigall, N. C. Electronic Transport in CdSe Nanoplatelet Based Polymer Fibres. *J. Mater. Chem. C* **2018**, 6 (40), 10916-10923.

(61) Antanovich, A.; Prudnikau, A.; Matsukovich, A.; Achtstein, A.; Artemyev, M. Self-Assembly of CdSe Nanoplatelets into Stacks of Controlled Size Induced by Ligand Exchange. *J. Phys. Chem. C* **2016**, 120 (10), 5764–5775.

(62) Antanovich, A.; Achtstein, A. W.; Matsukovich, A.; Prudnikau, A.; Bhaskar, P.; Gurin, V.; Molinari, M.; Artemyev, M. A Strain-Induced Exciton Transition Energy Shift in CdSe Nanoplatelets: the Impact of an Organic Ligand Shell. *Nanoscale* **2017**,9, 18042-18053.

(63) Dufour, M.; Qu, J.; Greboval, C.; Methivier, C.; Lhuillier, E.; Ithurria, S. Halide Ligands To Release Strain in Cadmium Chalcogenide Nanoplatelets and Achieve High Brightness. *ACS Nano* **2019**, 13 (5), 5326-5334.

(64) Diroll, B. T.; Schaller, R. D. Shape-Selective Optical Transformations of CdSe Nanoplatelets Driven by Halide Ion Ligand Exchange. *Chem. Mater.* **2019**, 31 (9), 3556-3563.

(65) Ji, C.; Buhro, W. E. Two-Phase Ligand Exchanges on CdSe Nanoplatelets. *Chem. Mater.* **2020**, 32 (12), 5290-5300.

(66) Sun, H.; Buhro, W. E. Reversible Z-Type to L-Type Ligand Exchange on Zinc Blende Cadmium Selenide Nanoplatelets. *Chem. Mater.* **2020**, 32 (13), 5814–5826.

(67) Diroll, B. T. Ligand-Dependent Tuning of Interband and Intersubband Transitions of Colloidal CdSe Nanoplatelets. *Chem. Mater.* **2020**, 32 (13), 5916-5923.

(68) Miethe, J. F.; Schlosser, A.; Eckert, J. G.; Lubkemann, F.; Bigall, N. C. Electronic Transport in CdSe Nanoplatelet based Polymer Fibres. *J. Mater. Chem. C* **2018**, 6 (40), 10916-10923.

(69) Graf, R. T.; Schlosser, A.; Zámbó, D.; Schlenkrich, J.; Rusch, P.; Chatterjee, A.; Pfnür, H.; Bigall, N. C. Interparticle Distance Variation in Semiconductor Nanoplatelet Stacks. *Adv. Funct. Mater.* **2022**, 32, 2112621.

(70) Palazon, F.; Di Stasio, F.; Lauciello, S.; Krahne, R.; Prato, M.; Manna, L. Evolution of $CsPbBr_3$ Nanocrystals upon Post-Synthesis Annealing Under an Inert Atmosphere. *J. Mater. Chem. C* **2016**, 4 (39), 9179-9182.

(71) Cargnello, M.; Chen, C.; Diroll, B. T.; Doan-Nguyen, V. V. T.; Gorte, R. J.; Murray, C. B. Efficient Removal of Organic Ligands from Supported Nanocrystals by Fast Thermal Annealing Enables Catalytic Studies on Well-Defined Active Phases. *J. Am. Chem. Soc.* **2015**, 137 (21), 6906-6911.

(72) Webber, D. H.; Brutchey, R. L. Ligand Exchange on Colloidal CdSe Nanocrystals Using Thermally Labile Tert-Butylthiol for Improved Photocurrent in Nanocrystal Films. *J. Am. Chem. Soc.* **2012**, 134 (2), 1085-1092.

(73) Moyen, E.; Jun, H.; Kim, H.-M.; Jang, J. Surface Engineering of Room Temperature-Grown Inorganic Perovskite Quantum Dots for Highly Efficient Inverted Light-Emitting Diodes. *ACS Appl. Mater. Interfaces* **2018**, 10 (49), 42647-42656.

(74) Burford, N.; El-Shenawee, M. Review of Terahertz Photoconductive Antenna Technology. *Opt. Eng.* **2017**, 56 (1), 010901.

(75) Ravi, K.; Huang, W. R.; Carbajo, S.; Nanni, E. A.; Schimpf, D. N.; Ippen, E. P.; Kärtner, F. X. Theory of Terahertz Generation by Optical Rectification Using Tilted-Pulse-Fronts. *Opt. Express* **2015**, 23 (4), 5253-5276.

(76) Ulbricht, R.; Hendry, E.; Shan, J.; Heinz, T. F.; Bonn, M. Carrier Dynamics in Semiconductors Studied with Time-Resolved Terahertz Spectroscopy. *Rev. Mod. Phys.* **2011**, 83 (2), 543-586.

(77) Kulkarni, A.; Evers, W. H.; van Waas, T. P.; Siebbeles, L. D. A. Photogeneration Quantum Yield and Character of Free Charges and Excitons in PbSe Nanorods. *J. Phys. Chem. C* **2020**, 124 (13), 7550-7557.

(78) Kunneman, L. T.; Schins, J. M.; Pedetti, S.; Heuclin, H.; Grozema, F. C.; Houtepen, A. J.; Dubertret, B.; Siebbeles, L. D. A. Nature and Decay Pathways of Photoexcited States in CdSe and CdSe/CdS Nanoplatelets. *Nano Lett.* **2014**, 14 (12), 7039-7045.

(79) Huang, Y.; Khiabani, N.; Shen, Y.; Li, D. Terahertz Photoconductive Antenna Efficiency. *In 2011 International Workshop on Antenna Technology (iWAT),* **2011**, 152-156.

(80) Woolard, D. L.; Loerop, W. R.; Shur, M. Terahertz Sensing Technology: Electronic Devices and Advanced Systems Technology; *World Scientific*, **2003**.

(81) Jepsen, P. U.; Jacobsen, R. H.; Keiding, S. R. Generation and Detection of Terahertz Pulses from Biased Semiconductor Antennas. *J. Opt. Soc. Am. B* **1996**, 13 (11), 2424-2436.

(82) Smith, P. R.; Auston, D. H.; Nuss, M. C. Subpicosecond Photoconducting Dipole Antennas. *IEEE J. Quantum Electron.* **1988**, 24 (2), 255-260.

(83) Benicewicz, P. K.; Roberts, J. P.; Taylor, A. J. Scaling of Terahertz Radiation From Large-Aperture Biased Photoconductors. *J. Opt. Soc. Am. B* **1994**, 11 (12), 2533-2546.

(84) Park, G.-S., Kim, Y. H., Han, H., Han, J. K., Ahn, J., Son, J.-H., Park, W.-Y., Jeong, Y. U. Eds. Ultrabroadband Terahertz Spectroscopy. In Convergence of Terahertz Sciences in Biomedical Systems, *Springer Netherlands,* **2012**, 219-229.

(85) Kim, D. S.; Citrin, D. S. Coulomb and Radiation Screening in Photoconductive Terahertz Sources. *Appl. Phys. Lett.* **2006**, 88 (16), 161117.

(86) Benicewicz, P. K.; Taylor, A. J. Scaling of Terahertz Radiation from Large-Aperture Biased InP Photoconductors. *Opt. Lett.* **1993**, 18 (16), 1332-1334.

(87) Bass, M.; Franken, P. A.; Ward, J. F.; Weinreich, G. Optical Rectification. *Phys. Rev. Lett.* **1962**, 9 (11), 446-448.

(88) Kübler, C.; Huber, R.; Tübel, S.; Leitenstorfer, A. Ultrabroadband Detection of Multi-Terahertz Field Transients with GaSe Electro-Optic Sensors: Approaching the Near Infrared. *Appl. Phys. Lett*. **2004**, 85 (16), 3360-3362.

(89) Wu, Q.; Zhang, X.-C. 7 Terahertz Broadband GaP Electro-Optic Sensor. *Appl. Phys. Lett.* **1997**, 70 (14), 1784-1786.

(90) Lu, P.-K.; Olvera, A. d. J. F.; Turan, D.; Seifert, T. S.; Yardimci, N. T.; Kampfrath, T.; Preu, S.; Jarrahi, M. Ultrafast Carrier Dynamics in Terahertz Photoconductors and Photomixers: Beyond Short-Carrier-Lifetime Semiconductors. *Nanophotonics* **2022**, 11 (11), 2661-2691.

(91) Wu, Q.; Litz, M.; Zhang, X. C. Broadband Detection Capability of ZnTe Electro-Optic Field Detectors. *Appl. Phys. Lett.* **1996**, 68 (21), 2924-2926.

(92) Jiang, Z.; Zhang, X. C. Electro-Optic Measurement of THz Field Pulses with a Chirped Optical Beam. *Appl. Phys. Lett.* **1998**, 72 (16), 1945-1947.

(93) Cocker, T. L.; Baillie, D.; Buruma, M.; Titova, L. V.; Sydora, R. D.; Marsiglio, F.; Hegmann, F. A. Microscopic Origin of the Drude-Smith Model. *Phys. Rev. B* **2017**, 96 (20), 205439.

(94) Rossinelli, A. A.; Riedinger, A.; Marqués-Gallego, P.; Knüsel, P. N.; Antolinez, F. V.; Norris, D. J. High-Temperature Growth of Thick-Shell CdSe/CdS Core/Shell Nanoplatelets. *Chem. Commun.* **2017**, 53 (71), 9938-9941.

(95) Deryaguin, B.; Landau, L. D., *Acta Physicochim. URSS* **1941**, 14 (633).

(96) Alivisatos, A. P. Semiconductor Clusters, Nanocrystals, and Quantum Dots. *Science* **1996**, 271 (5251), 933-937.

(97) El-Sayed, M. A. Small Is Different: Shape-, Size-, and Composition-Dependent Properties of Some Colloidal Semiconductor Nanocrystals. *Acc. Chem. Res.* **2004**, 37 (5), 326-333.

(98) Talapin, D. V.; Lee, J.-S.; Kovalenko, M. V.; Shevchenko, E. V. Prospects of Colloidal Nanocrystals for Electronic and Optoelectronic Applications. *Chem. Rev.* **2010**, 110 (1), 389-458.

(99) Reiss, P.; Carrière, M.; Lincheneau, C.; Vaure, L.; Tamang, S. Synthesis of Semiconductor Nanocrystals, Focusing on Nontoxic and Earth-Abundant Materials. *Chem. Rev.* **2016**, 116 (18), 10731-10819.

(100) Chen, Y.; Fan, Z.; Zhang, Z.; Niu, W.; Li, C.; Yang, N.; Chen, B.; Zhang, H. Two-Dimensional Metal Nanomaterials: Synthesis, Properties, and Applications. *Chem. Rev.* **2018**, 118 (13), 6409-6455.

(101) Tang, J.; Sargent, E. H. Infrared Colloidal Quantum Dots for Photovoltaics: Fundamentals and Recent Progress. *Adv. Mater.* **2011**, 23 (1), 12-29.

(102) Du, Y.-P.; Xie, G. Uniform ZnO Nanorods Derived from Lithium Ions as a Growth Controlling Agent in Non-Aqueous Medium. *CrystEngComm* **2011**, 13 (2), 437-439.

(103) Mao, J.; Cao, X.; Zhen, J.; Shao, H.; Gu, H.; Lu, J.; Ying, J. Y. Facile Synthesis of Hybrid Nanostructures from Nanoparticles, Nanorods, and Nanowires. *J. Mater. Chem.* **2011**, 21 (31), 11478-11481.

(104) Wang, H.; Jeong, H. Y.; Imura, M.; Wang, L.; Radhakrishnan, L.; Fujita, N.; Castle, T.; Terasaki, O.; Yamauchi, Y. Shape- and Size-Controlled Synthesis in Hard Templates: Sophisticated Chemical Reduction for Mesoporous Monocrystalline Platinum Nanoparticles. *J. Am. Chem. Soc.* **2011**, 133 (37), 14526-14529.

(105) Astruc, D. Introduction: Nanoparticles in Catalysis. *Chem. Rev.* **2020**, 120 (2), 461-463.

(106) Duan, X.; Huang, Y.; Cui, Y.; Wang, J.; Lieber, C. M. Indium Phosphide Nanowires as Building Blocks for Nanoscale Electronic and Optoelectronic Devices. *Nature* **2001**, 409 (6816), 66-69.

(107) Wang, J.; Gudiksen, M. S.; Duan, X.; Cui, Y.; Lieber, C. M. Highly Polarized Photoluminescence and Photodetection from Single Indium Phosphide Nanowires. *Science* **2001**, 293 (5534), 1455-1457.

(108) Wang, F.; Yu, H.; Li, J.; Hang, Q.; Zemlyanov, D.; Gibbons, P. C.; Wang; Janes, D. B.; Buhro, W. E. Spectroscopic Properties of Colloidal Indium Phosphide Quantum Wires. *J. Am. Chem. Soc.* **2007**, 129 (46), 14327-14335.

(109) Sun, J.; Yin, Y.; Han, M.; Yang, Z.-x.; Lan, C.; Liu, L.; Wang, Y.; Han, N.; Shen, L.; Wu, X.; et al. Nonpolar-Oriented Wurtzite InP Nanowires with Electron Mobility Approaching the Theoretical Limit. *ACS Nano* **2018**, 12 (10), 10410-10418.

(110) Chen, B.; Li, D.; Wang, F. InP Quantum Dots: Synthesis and Lighting Applications. *Small* **2020**, 16 (32), 2002454.

(111) Calvin, J. J.; Swabeck, J. K.; Sedlak, A. B.; Kim, Y.; Jang, E.; Alivisatos, A. P. Thermodynamic Investigation of Increased Luminescence in Indium Phosphide Quantum Dots by Treatment with Metal Halide Salts. *J. Am. Chem. Soc.* **2020**, 142 (44), 18897-18906.

(112) Grigioni, I.; Sagar, L. K.; Li, Y. C.; Lee, G.; Yan, Y.; Bertens, K.; Miao, R. K.; Wang, X.; Abed, J.; Won, D. H.; et al. $CO_2$ Electroreduction to Formate at a Partial Current Density of 930 mA $cm^{-2}$ with InP Colloidal Quantum Dot Derived Catalysts. *ACS Energy Lett.* **2021**, 6 (1), 79-84.

(113) Green, M.; O'Brien, P. A Novel Metalorganic Route for the Direct and Rapid Synthesis of Monodispersed Quantum Dots of Indium Phosphide. *Chem. Commun.* **1998**, (22), 2459-2460.

(114) Friedfeld, M. R.; Stein, J. L.; Cossairt, B. M. Main-Group-Semiconductor Cluster Molecules as Synthetic Intermediates to Nanostructures. *Inorg. Chem.* **2017**, 56 (15), 8689-8697.

(115) Thuy, U. T. D.; Huyen, T. T. T.; Liem, N. Q.; Reiss, P. Low-Temperature Synthesis of InP Nanocrystals. *Mater. Chem. Phys.* **2008**, 112 (3), 1120-1123.

(116) Ramasamy, P.; Kim, N.; Kang, Y.-S.; Ramirez, O.; Lee, J.-S. Tunable, Bright, and Narrow-Band Luminescence from Colloidal Indium Phosphide Quantum Dots. *Chem. Mater.* **2017**, 29 (16), 6893-6899.

(117) Zan, F.; Ren, J. Gas-Liquid Phase Synthesis of Highly Luminescent InP/ZnS Core/Shell Quantum Dots Using Zinc Phosphide as a New Phosphorus Source. *J. Mater. Chem.* **2012**, 22 (96), 1794-1799.

(118) Mundy, M. E.; Ung, D.; Lai, N. L.; Jahrman, E. P.; Seidler, G. T.; Cossairt, B. M.

Aminophosphines as Versatile Precursors for the Synthesis of Metal Phosphide Nanocrystals. *Chem. Mater*. **2018**, 30 (15), 5373-5379.

(119) Jun, K.-W.; Khanna, P. K.; Hong, K.-B.; Baeg, J.-O.; Suh, Y.-D. Synthesis of InP Nanocrystals from Indium Chloride and Sodium Phosphide by Solution Route. *Mater. Chem. Phys.* **2006**, 96 (2), 494-497.

(120) Ramasamy, P.; Kim, N.; Kang, Y. S.; Ramirez, O.; Lee, J. S. Tunable, Bright, and Narrow-Band Luminescence from Colloidal Indium Phosphide Quantum Dots. *Chem. Mater*. **2017**, 29, 6893-6899.

(121) Liu, J.; Meyns, M.; Zhang, T.; Arbiol, J.; Cabot, A.; Shavel, A. Triphenyl Phosphite as the Phosphorus Source for the Scalable and Cost-Effective Production of Transition Metal Phosphides. *Chem. Mater*. **2018**, 30 (5), 1799-1807.

(122) Lee, D.; Koh, S.; Yoon, D.-E.; Lee, S.; Kim, W. D.; Kim, D.; Bae, W. K.; Lim, J.; Lee, D. C. Synthesis of InP Nanocrystals Using Triphenyl Phosphite as Phosphorus Source. *Korean J. Chem. Eng.* **2019**, 36 (9), 1518-1526.

(123) Muthuswamy, E.; Brock, S. L. Oxidation Does Not (Always) Kill Reactivity of Transition Metals: Solution-Phase Conversion of Nanoscale Transition Metal Oxides to Phosphides and Sulfides. *J. Am. Chem. Soc.* **2010**, 132 (45), 15849-15851.

(124) Gerdes, F.; Volkmann, M.; Schliehe, C.; Bielewicz, T.; Klinke, C. Sculpting of Lead Sulfide Nanoparticles by Means of Acetic Acid and Dichloroethane. *Z. Phys. Chem.* **2015**, 229 (1-2), 139-151.

(125) Mendoza-Garcia, A.; Zhu, H.; Yu, Y.; Li, Q.; Zhou, L.; Su, D.; Kramer, M. J.; Sun, S. Controlled Anisotropic Growth of Co-Fe-P from Co-Fe-O Nanoparticles. *Angew. Chem., Int. Ed.* **2015**, 54 (33), 9642-9645.

(126) Himstedt, R.; Hinrichs, D.; Sann, J.; Weller, A.; Steinhauser, G.; Dorfs, D. Halide Ion Influence on the Formation of Nickel Nanoparticles and Their Conversion into Hollow Nickel Phosphide and Sulphide Nanocrystals. *Nanoscale* **2019**, 11 (32), 15104-15111.

(127) Wu, Y.; Wang, D.; Li, Y. Nanocrystals from Solutions: Catalysts. *Chem. Soc. Rev*. **2014**, 43 (7), 2112-2124.

(128) Duan, H.; Wang, D.; Li, Y. Green Chemistry for Nanoparticle Synthesis. *Chem. Soc. Rev.* **2015**, 44 (16), 5778-5792.

(129) Kovalenko, M. V.; Manna, L.; Cabot, A.; Hens, Z.; Talapin, D. V.; Kagan, C. R.; Klimov,

V. I.; Rogach, A. L.; Reiss, P.; Milliron, D. J.; et al. Prospects of Nanoscience with Nanocrystals. *ACS Nano* **2015**, 9 (2), 1012-1057.

(130) Cao, S.; Tao, F. F.; Tang, Y.; Li, Y.; Yu, J. Size- and Shape-Dependent Catalytic Performances of Oxidation and Reduction Reactions on Nanocatalysts. *Chem. Soc. Rev.* **2016**, 45 (17), 4747-4765.

(131) Luo, M.; Guo, S. Strain-Controlled Electrocatalysis on Multimetallic Nanomaterials. *Nat. Rev. Mater.* **2017**, 2 (11), 17059.

(132) Verwey, E. W.; Overbeek, J. T. G., Theory of Stability of Lyophobic Colloids. *Elsevier*, **1948**.

(133) Rabani, E. An Interatomic Pair Potential for Cadmium Selenide. *J. Chem. Phys.* **2002**, 116 (1), 258-262.

(134) Dubertret, S. I. a. B. Quasi 2D Colloidal CdSe Platelets with Thicknesses Controlled at the Atomic Level. *J. Am. Chem. Soc.* **2008**, 130, 49, 16504–16505.

(135) Christodoulou, S.; Climente, J. I.; Planelles, J.; Brescia, R.; Prato, M.; Martin-Garcia, B.; Khan, A. H.; Moreels, I. Chloride-Induced Thickness Control in CdSe Nanoplatelets. *Nano Lett.* **2018**, 18 (10), 6248-6254.

(136) Yang, G.; Kazes, M.; Oron, D. Chiral 2D Colloidal Semiconductor Quantum Wells. *Adv. Funct. Mater.* **2018**, 28, 1802012.

(137) Cho, W.; Kim, S.; Coropceanu, I.; Srivastava, V.; Diroll, B. T.; Hazarika, A.; Fedin, I.; Galli, G.; Schaller, R. D.; Talapin, D. V. CdSe NPLs Direct Synthesis of Six-Monolayer (1.9 nm) Thick Zinc-Blende CdSe Nanoplatelets Emitting at 585 nm. *Chem. Mater.* **2018**, 30 (20), 6957-6960.

(138) Ma, X.; Diroll, B. T.; Cho, W.; Fedin, I.; Schaller, R. D.; Talapin, D. V.; Gray, S. K.; Wiederrecht, G. P.; Gosztola, D. J. Size-Dependent Biexciton Quantum Yields and Carrier Dynamics of Quasi-Two-Dimensional Core/Shell Nanoplatelets. *ACS Nano* **2017**, 11 (9), 9119-9127.

(139) Derjaguin, B., Untersuchungen über die Reibung und Adhäsion, IV. *Kolloid-Zeitschrift* **1934**, 69 (2), 155-164.

(140) Lien, D.-H.; Uddin, S. Z.; Yeh, M.; Amani, M.; Kim, H.; Ager, J. W.; Yablonovitch, E.; Javey, A. Electrical Suppression of All Nonradiative Recombination Pathways in Monolayer Semiconductors. *Science* **2019**, 364 (6439), 468-471.

(141) He, T.; Zhang, Y.; Zhang, H.; Zhao, J.; Shi, H.; Yang, H.; Yang, P. Aggregation-Induced

Structural Symmetry Breaking Promotes Charge Separation for Efficient Photocatalytic Hydrogen Production. *ChemSusChem*, **2023**, e202300500.

(142) Liao, Q. Chapter Four-Enhanced Sampling and Free Energy Calculations for Protein Simulations. *Prog Mol Biol Transl Sci.* **2020**, 170, 177-213.

(143) Talapin, D. V.; Lee, J.-S.; Kovalenko, M. V.; Shevchenko, E. V. Prospects of Colloidal Nanocrystals for Electronic and Optoelectronic Applications. *Chem. Rev.* **2010**, 110 (1), 389-458.

(144) Nasilowski, M.; Mahler, B.; Lhuillier, E.; Ithurria, S.; Dubertret, B. Two-Dimensional Colloidal Nanocrystals. *Chem. Rev.* **2016**, 116 (18), 10934-10982.

(145) Zito, J.; Infante, I. The Future of Ligand Engineering in Colloidal Semiconductor Nanocrystals. *Acc. Chem. Res.* **2021**, 54 (7), 1555-1564.

(146) Choi, J.-H.; Wang, H.; Oh, S. J.; Paik, T.; Sung, P.; Sung, J.; Ye, X.; Zhao, T.; Diroll, B. T.; Murray, C. B.; et al. Exploiting the Colloidal Nanocrystal Library to Construct Electronic Devices. *Science* **2016**, 352 (6282), 205-208.

(147) Kim, Y.-H.; Park, J.; Kim, S.; Kim, J. S.; Xu, H.; Jeong, S.-H.; Hu, B.; Lee, T.-W. Exploiting the Full Advantages of Colloidal Perovskite Nanocrystals for Large-Area Efficient Light-Emitting Diodes. *Nat. Nanotechnol.* **2022**, 17 (6), 590-597.

(148) Wang, Y.; Kavanagh, S. R.; Burgués-Ceballos, I.; Walsh, A.; Scanlon, D. O.; Konstantatos, G. Cation Disorder Engineering Yields $AgBiS_2$ Nanocrystals with Enhanced Optical Absorption for Efficient Ultrathin Solar Cells. *Nat. Photonics.* **2022**, 16 (3), 235-241.

(149) Maier, A.; Strauß, F.; Kohlschreiber, P.; Schedel, C.; Braun, K.; Scheele, M. Sub-nanosecond Intrinsic Response Time of PbS Nanocrystal IR-Photodetectors. *Nano Lett.* **2022**, 22 (7), 2809-2816.

(150) Akkerman, Q. A.; Nguyen, T. P. T.; Boehme, S. C.; Montanarella, F.; Dirin, D. N.; Wechsler, P.; Beiglböck, F.; Rainò, G.; Erni, R.; Katan, C.; et al. Controlling the Nucleation and Growth Kinetics of Lead Halide Perovskite Quantum Dots. *Science* **2022**, 377 (6613), 1406-1412.

(151) Wang, F.; Dong, A.; Buhro, W. E. Solution–Liquid–Solid Synthesis, Properties, and Applications of One-Dimensional Colloidal Semiconductor Nanorods and Nanowires. *Chem. Rev.* **2016**, 116 (18), 10888-10933.

(152) Ithurria, S.; Dubertret, B. Quasi 2D Colloidal CdSe Platelets with Thicknesses Controlled at the Atomic Level. *J. Am. Chem. Soc.* **2008**, 130, 16504–16505.

(153) Riedinger, A.; Ott, F. D.; Mule, A.; Mazzotti, S.; Knusel, P. N.; Kress, S. J. P.; Prins, F.;

Erwin, S. C.; Norris, D. J. An Intrinsic Growth Instability in Isotropic Materials Leads to Quasi-Two-Dimensional Nanoplatelets. *Nat. Mater.* **2017**, 16 (7), 743-748.

(154) Butt, H.-J.; Graf, K.; Kappl, M., Physics and Chemistry of Interfaces. *Wiley-VCH: Weinheim*, **2006**.

(155) Christodoulou, S.; Climente, J. I.; Planelles, J.; Brescia, R.; Prato, M.; Martin-Garcia, B.; Khan, A. H.; Moreels, I. Chloride-Induced Thickness Control in CdSe Nanoplatelets. *Nano Lett.* **2018**, 18 (10), 6248-6254.

(156) Yang, G.; Kazes, M.; Oron, D. Chiral 2D Colloidal Semiconductor Quantum Wells. *Adv. Funct. Mater.* **2018**, 28, 1802012.

(157) Zelewski, S. J.; Nawrot, K. C.; Zak, A.; Gladysiewicz, M.; Nyk, M.; Kudrawiec, R. Exciton Binding Energy of Two-Dimensional Highly Luminescent Colloidal Nanostructures Determined from Combined Optical and Photoacoustic Spectroscopies. *J. Phys. Chem. Lett.* **2019**, 10 (12), 3459-3464.

(158) Shornikova, E. V.; Yakovlev, D. R.; Gippius, N. A.; Qiang, G.; Dubertret, B.; Khan, A. H.; Di Giacomo, A.; Moreels, I.; Bayer, M. Exciton Binding Energy in CdSe Nanoplatelets Measured by One- and Two-Photon Absorption. *Nano Lett.* **2021**, 21 (24), 10525-10531.

(159) Geiregat, P.; Rodá, C.; Tanghe, I.; Singh, S.; Di Giacomo, A.; Lebrun, D.; Grimaldi, G.; Maes, J.; Van Thourhout, D.; Moreels, I.; et al. Localization-Limited Exciton Oscillator Strength in Colloidal CdSe Nanoplatelets Revealed by the Optically Induced Stark Effect. *Light: Science & Applications* **2021**, 10 (1), 112.

(160) Yeltik, A.; Delikanli, S.; Olutas, M.; Kelestemur, Y.; Guzelturk, B.; Demir, H. V. Experimental Determination of the Absorption Cross-Section and Molar Extinction Coefficient of Colloidal CdSe Nanoplatelets. *J. Phys. Chem. C* **2015**, 119 (47), 26768-26775.

(161) Bai, P.; Hu, A.; Deng, Y.; Tang, Z.; Yu, W.; Hao, Y.; Yang, S.; Zhu, Y.; Xiao, L.; Jin, Y.; et al. CdSe/CdSeS Nanoplatelet Light-Emitting Diodes with Ultrapure Green Color and High External Quantum Efficiency. *J. Phys. Chem. Lett.* **2022**, 13 (39), 9051-9057.

(162) Liu, Y.; Gibbs, M.; Puthussery, J.; Gaik, S.; Ihly, R.; Hillhouse, H. W.; Law, M. Dependence of Carrier Mobility on Nanocrystal Size and Ligand Length in PbSe Nanocrystal Solids. *Nano Lett.* **2010**, 10 (5), 1960-1969.

(163) Gao, Y.; Aerts, M.; Sandeep, C. S. S.; Talgorn, E.; Savenije, T. J.; Kinge, S.; Siebbeles, L. D. A.; Houtepen, A. J. Photoconductivity of PbSe QuantumDot Solids: Dependence on Ligand

Anchor Group and Length. *ACS Nano* **2012**, 6, 9606-9614.

(164) Zhang, H.; Liu, W.; Talapin, D. V. Colloidal Nanocrystals with Inorganic Halide, Pseudohalide, and Halometallate Ligands. *ACS Nano* **2014**, 8, 7359-7369.

(165) Sandeep, C. S. S.; Azpiroz, J. M.; Evers, W. H.; Boehme, S. C.; Moreels, I.; Kinge, S.; Siebbeles, L. D. A.; Infante, I.; Houtepen, A. J. Epitaxially Connected PbSe QuantumDot Films: Controlled Neck Formation and Optoelectronic Properties. *ACS Nano* **2014**, 8, 11499-11511.

(166) Giansante, C.; Infante, I.; Fabiano, E.; Grisorio, R.; Suranna, G. P.; Gigli, G. "Darker-Than-Black" PbS Quantum Dots: Enhancing Optical Absorption of Colloidal Semiconductor Nanocrystals via Short Conjugated Ligands. *J. Am. Chem. Soc.* **2015**, 137 (5), 1875-1886.

(167) Lee, W. S.; Kang, Y. G.; Sharma, M.; Lee, Y. M.; Jeon, S.; Sharma, A.; Demir, H. V.; Han, M. J.; Koh, W. K.; Oh, S. J. Ligand Exchange and Impurity Doping in 2D CdSe Nanoplatelet Thin Films and Their Applications. *Adv. Electron. Mater.* **2022**, 8, 2100739.

(168) Graf, R. T.; Schlosser, A.; Zámbó, D.; Schlenkrich, J.; Rusch, P.; Chatterjee, A.; Pfnür, H.; Bigall, N. C. Interparticle Distance Variation in Semiconductor Nanoplatelet Stacks. *Adv. Funct. Mater.* **2022**, 2112621.

(169) Galle, T.; Spittel, D.; Weiss, N.; Shamraienko, V.; Decker, H.; Georgi, M.; Hubner, R.; Metzkow, N.; Steinbach, C.; Schwarz, D.; et al. Simultaneous Ligand and Cation Exchange of Colloidal CdSe Nanoplatelets toward PbSe Nanoplatelets for Application in Photodetectors. *J. Phys. Chem. Lett.* **2021**, 12, 5214-5220.

(170) Talapin, D. V. Colloidal Nanocrystals with Molecular Metal Chalcogenide Surface Ligands. *Science* **2009**, 324, 1417-1420.

(171) Talapin, D. V. Band-Like Transport, High Electron Mobility and High Photoconductivity in All-Inorganic Nanocrystal Arrays. *Nat. Nanotechnol.* **2011**, 6, 348-352.

(172) Zhang, S.; Cyr, P. W.; McDonald, S. A.; Konstantatos, G.; Sargent, E. H. EnhancedInfrared Photovoltaic Efficiency in PbS Nanocrystal/Semiconducting Polymer Composites: 600-Fold increase in Maximum Power Output via Control of the Ligand Barrier. *Appl. Phys. Lett.* **2005**, 87 (23), 233101.

(173) Sutton, R. J.; Eperon, G. E.; Miranda, L.; Parrott, E. S.; Kamino, B. A.; Patel, J. B.; Hörantner, M. T.; Johnston, M. B.; Haghighirad, A. A.; Moore, D. T.; et al. Bandgap-Tunable Cesium Lead Halide Perovskites with High Thermal Stability for Efficient Solar Cells. *Adv. Energy Mater.* **2016**, 6 (8), 1502458.

(174) Palazon, F.; Di Stasio, F.; Lauciello, S.; Krahne, R.; Prato, M.; Manna, L. Evolution of $CsPbBr_3$ Nanocrystals upon Post-Synthesis Annealing under an Inert Atmosphere. *J. Mater. Chem. C* **2016**, 4 (39), 9179-9182.

(175) Webber, D. H.; Brutchey, R. L. Ligand Exchange on Colloidal CdSe Nanocrystals Using Thermally Labile Tert-Butylthiol for Improved Photocurrent in Nanocrystal Films. *J. Am. Chem. Soc.* **2012**, 134 (2), 1085-1092.

(176) Graf, R. T.; Schlosser, A.; Zámbó, D.; Schlenkrich, J.; Rusch, P.; Chatterjee, A.; Pfnür, H.; Bigal, N. C. Interparticle Distance Variation in Semiconductor Nanoplatelet Stacks. *Adv. Funct. Mater.* **2022**, 2112621.

(177) Ithurria, S.; Dubertret, B. Quasi 2D Colloidal CdSe Platelets with Thicknesses Controlled at the Atomic Level. *J. Am. Chem. Soc.* **2008**, 130 (49), 16504-16505.

(178) Ithurria, S.; Tessier, M. D.; Mahler, B.; Lobo, R. P. S. M.; Dubertret, B.; Efros, A. L. Colloidal Nanoplatelets with Two-Dimensional Electronic Structure. *Nat. Mater.* **2011**, 10 (12), 936-941.

(179) Li, D.; Wang, C.; Tripkovic, D.; Sun, S.; Markovic, N. M.; Stamenkovic, V. R. Surfactant Removal for Colloidal Nanoparticles from Solution Synthesis: The Effect on Catalytic Performance. *ACS. Catal.* **2012**, 2 (7), 1358-1362.

(180) Cargnello, M.; Chen, C.; Diroll, B. T.; Doan-Nguyen, V. V. T.; Gorte, R. J.; Murray, C. B. Efficient Removal of Organic Ligands from Supported Nanocrystals by Fast Thermal Annealing Enables Catalytic Studies on Well-Defined Active Phases. *J. Am. Chem. Soc.* **2015**, 137 (21), 6906-6911.

(181) Iacono, F.; de la Cueva, L.; Gallego, J. M.; Juarez, B. H.; Otero, R. Thermal Ligand Desorption in CdSe Quantum Dots by Correlated XPS and STM. *Part. Part. Syst. Charact.* **2016**, 33 (7), 358-362.

(182) Moyen, E.; Jun, H.; Kim, H.-M.; Jang, J. Surface Engineering of Room Temperature-Grown Inorganic Perovskite Quantum Dots for Highly Efficient Inverted Light-Emitting Diodes. *ACS Appl. Mater. Interfaces* **2018**, 10 (49), 42647-42656.

(183) Trindade, T.; O'Brien, P.; Zhang, X.-m. Synthesis of CdS and CdSe Nanocrystallites Using a Novel Single-Molecule Precursors Approach. *Chem. Mater.* **1997**, 9 (2), 523-530.

(184) Wu, W.; He, F.; Wang, Y. Reversible Ultrafast Melting in Bulk CdSe. *J. Appl. Phys.* **2016**, 119 (5), 055701.

(185) Cherevkov, S. A.; Fedorov, A. V.; Artemyev, M. V.; Prudnikau, A. V.; Baranov, A. V. Anisotropy of Electron-Phonon Interaction in Nanoscale CdSe Platelets as Seen via Off-Resonant and Resonant Raman Spectroscopy. *Phys. Rev. B* **2013**, 88 (4), 041303.

(186) Kumar, S.; Ojha, A. K. Synthesis, Characterizations and Antimicrobial Activities of Well Dispersed Ultra-Long CdO Nanowires. *AIP Advances* **2013**, 3 (5), 052109.

(187) Tanford, C. Micelle Shape and Size. *J. Phys. Chem.* **1972**, 76, 3020−3024.

(188) Tries, A.; Osella, S.; Zhang, P.; Xu, F.; Ramanan, C.; Klaui, M.; Mai, Y.; Beljonne, D.; Wang, H. I. Experimental Observation of Strong Exciton Effects in Graphene Nanoribbons. *Nano Lett.* **2020**, 20 (5), 2993-3002.

(189) Zheng, W.; Zorn, N. F.; Bonn, M.; Zaumseil, J.; Wang, H. I. Probing Carrier Dynamics in sp3-Functionalized Single-Walled Carbon Nanotubes with Time-Resolved Terahertz Spectroscopy. *ACS Nano* **2022**, 16 (6), 9401-9409.

(190) Wang, X.; Ma, J.; Zheng, W.; Osella, S.; Arisnabarreta, N.; Droste, J.; Serra, G.; Ivasenko, O.; Lucotti, A.; Beljonne, D.; et al. Cove-Edged Graphene Nanoribbons with Incorporation of Periodic Zigzag-Edge Segments. *J. Am. Chem. Soc.* **2022**, 144 (1), 228-235.

## List of Publications

This thesis is based on the following publications and manuscripts:

(1) Anisotropic and Hyperbranched InP Nanocrystals via Chemical Transformation of in Situ Produced $In_2O_3$,
**Shuai Chen** and Andreas Riedinger. *Chem. Commun* **2022**, 58, 9246-9249; **(Chapter 3)**

(2) Ligand Decomposition Governs the Inter-Nanoplatelet Distance and Coupling Strength by Thermal Annealing,
**Shuai Chen**, Samir H. Al-Hilfi, Guangbo Chen, Heng Zhang, Wenhao Zheng, Lucia Di. Virgilio, Jaco J Geuchies, Junren Wang, Xinliang Feng, Andreas Riedinger, Mischa Bonn and Hai I. Wang. In preparation; **(Chapter 4)**

(3) Solvation Forces Affect the Colloidal Stability of CdSe Nanoplatelets,
**Shuai Chen**, Nanning Petersen, Martin Girard, Omar Valsson, Wenhao Zheng, Heng Zhang, Jaco J Geuchies, Andreas Riedinger, Mischa Bonn and Hai I. Wang. In preparation; **(Chapter 5)**

Other publications during the Ph.D. time:

(4) $Ag_{10}Ti_{28}$-Oxo Cluster Containing Single-Atom Silver Sites: Atomic Structure and Synergistic Electronic Properties,
**Shuai Chen**, Zhe-Ning Chen, Wei-Hui Fang, Wei Zhuang, Lei Zhang and Jian Zhang. *Angew. Chem. Int. Ed.* **2019**, 58, 10932–10935;

(5) Kinetic Control over Self-Assembly of Semiconductor Nanoplatelets,
Rebecca Momper, Heng Zhang, **Shuai Chen**, Henry Halim, Ewald Johannes, Stoyan Yordanov, Daniele Braga, Balthasar Blülle, David Doblas, Tobias Kraus, Mischa Bonn, Hai I. Wang, and Andreas Riedinger. *Nano Lett.* **2020**, 20, 6, 4102–4110;

(6) Threefold Collaborative Stabilization of $Ag_{14}$-Nanorods by Hydrophobic $Ti_{16}$-Oxo Clusters and Alkynes: Designable Assembly and Solid-State Optical-Limiting Application,
Xi Fan, Furong Yuan, Dejing Li, **Shuai Chen**, Zhibin Cheng, Zhangjing Zhang, Shengchang Xiang, Shuang-Quan Zang, Jian Zhang, and Lei Zhang. *Angew. Chem. Int. Ed.* **2021**, 60, 12949–12954;

(7) Protection of Ag Clusters by Metal-Oxo Modules,
Xi Fan, **Shuai Chen**, Lei Zhang, and Jian Zhang. *Chem. Eur. J.* **2021**, 27, 15563–15570;

(8) Solution-Processed Wafer-Scale $Ag_2S$ Thin Films: Synthesis and Excellent Charge Transport Properties,
Junren Wang, Shuai Fu, Heng Zhang, Robert Graf, Henry Halim, **Shuai Chen**, Wenhao Zheng, Mischa Bonn, Katharina Landfester, Andreas Riedinger and Hai I Wang. *Adv. Funct. Mater.* **2022**, 32, 2113147;

(9) Biomimetic $Cu_4$ Cluster Encapsulated within Hollow Titanium-Oxo Nanoring for Electrochemical $CO_2$ Reduction to Ethylene,
Xi Fan, Jian Cheng, Mei Qiu, Yongfan Zhang, **Shuai Chen**, Zhangjing Zhang, Yang Peng, Jian Zhang and Lei Zhang. *ACS Materials Lett.* **2023**, 5, 1527−1531;

(10) Nanomotors Driven by Single-Atom Catalysts,
**Shuai Chen**, Jianhong Wang, Shoupeng Cao, Samir H. Al-Hilfi, Juan Yang, Jingxin Shao, Jan C. M. van Hest, Mischa Bonn, Klaus Müllen and Yazhou Zhou. *Angew. Chem. Int. Ed.* **2023**, under review.

# Acknowledgments

Finally! Finally! Finally! Finally…… I nearly finish my Ph.D. time after 4.5 years since 15/01/2019. For me, the journey toward achieving the Ph.D. degree is twists and turns and challenging, but I believe that it must be incredibly rewarding for my whole life.

First and foremost, I would like to thank Prof. Dr. Mischa Bonn for having me work with so many open-minded, talented, happy, international colleagues in our department as a Doctoral researcher. Not only did you assist me in developing as an independent scientist, but you also offered me a smile and "Hi, Shuai!" whenever we met by chance. The smile and greeting are the greatest motivation when I drop off into pessimism and want to give up myself. You used "secret project" with a smile to describe the single-atom catalysts project, this "secret" help me to build the confidence and courage to me continue to engage in scientific research.

My project would undoubtedly be impossible without the help of my daily supervisor, Dr. Hai Wang. To you, I give my sincerest thanks because you never give up on me even though I am the last one. You always help me to become an independent scientist and person that I need to follow my own affairs. "Earned your Ph.D. degree by yourself" are your most inspiring words for me. There was a time when I thought I couldn't finish my Ph.D. degree. Many thanks to you again, Hai!

Dr. Andreas Riedinger, I am very grateful to you for introducing me to the field of nanocrystals. Without you, I couldn't start the Ph.D. project because material synthesis is the first step. InP NPLs is our final aim but I did not achieve the synthesis of it, you still encourage me and help me publish the first paper for my Ph.D. You give me valuable advice in time by WhatsApp even though on weekends when I send messages to you.

Laurie, many thaa------anks to you. You arranged many things for me very well with a nice smile whenever I need you.

For colleagues who have been directly involved in my projects: thank you all for your contributions to this thesis. Nanning, I have learned much simulation knowledge from you. Thanks to other collaborators: Prof. Dr. Xinliang Feng, Dr. Guangbo Chen, Dr. Martin Girard, and Dr. Omar Valsson.

Working with the people in AK Bonn has been a pleasant experience, so I thank the members of the department for providing such an atmosphere. For our "Rising Stars" (THz group) group, I

would certainly like to give a special mention to Wenhao and Heng, who helped me a lot with the THz part. I also thank the rest of the THz Team: Min, Shuai Fu, Xiaoqing, Lucia, Lei, Jiaming, Guanzhao, and Jaco for the useful discussion. Thanks to other members of the Bonn department: Jing, Xinfu, Kaifa, Kuo-Yang, Alessandro, Ali, Leon, Florian, Marc-Jan, and Chun-Chieh. For our synthesis group with Andreas, I would certainly like to give a special mention to Rebecca and Henry, who helped me off to a good start in the early days of Andreas' group. Thanks to other members of the Landfester department: Long, Julian, Junren, Yinzhou, Wenxin, Shoupeng, Christoph, and Seunghyeon. Last, I want to thank the small "CVD group", thank Yazhou to introduce me to a new field, and thank Samir to help a lot in the pyrolysis part.

In the end, I want to say to my goddess, my girlfriend, Dr. Xiaoxiao. For the last ten years, you always support me to achieve my dreams. From Kaifeng to Beijing, Fuzhou, and Mainz (Potsdam), you always encourage me even though you are in your hard Ph.D. time. Without you, I couldn't finish this thesis. Finally, I want to thank my parents and my sister to support me to finish my Ph.D.